UNIVERSITY OF OTTAWA

MASTER'S THESIS

Structural Studies of Boron Nitride Compounds Under Extreme Conditions

---

Author:

Spencer Sterling

Supervisor:

Professor Serge Desgreniers

A thesis submitted

in partial fulfillment of the requirements for the degree of

Master of Science in Physics

in the

Laboratoire de physique des solides denses

Department of Physics

Declaration of Authorship

I, **Spencer Sterling**, declare that this thesis titled, "Structural Studies of Boron Nitride Compounds Under Extreme Conditions" and the work presented in it are my own. I confirm that:

- This work was done wholly or mainly while in candidature for a research degree at this University.
- Where any part of this thesis has previously been submitted for a degree or any other qualification at this University or any other institution, this has been clearly stated.
- Where I have consulted the published work of others, this is always clearly attributed.
- Where I have quoted from the work of others, the source is always given. With the exception of such quotations, this thesis is entirely my own work.
- I have acknowledged all main sources of help.
- Where the thesis is based on work done by myself jointly with others, I have made clear exactly what was done by others and what I have contributed myself.

UNIVERSITY OF OTTAWA

Abstract

Faculty of Science

Department of Physics

Master of Science in Physics

Structural Studies of Boron Nitride Compounds Under Extreme Conditions

by **Spencer Sterling**

This document will present the work done on BN under high pressure conditions, both at room temperatures and at high temperatures under laser heating conditions. These experiments are performed to identify possible phase transitions within the BN system and characterize the materials present under the given conditions using a mixture of X-ray diffraction and Raman and infrared spectroscopies are employed. A review of the background and motivations for studies of BN under extreme conditions, as well as the techniques employed, is given as an introduction.

A phase transition from hexagonal boron nitride (hBN) to wurtzite boron nitride (wBN) is observed beginning at 9 GPa and room temperature, with coexistence of the two phases until 14 GPa for hydrostatic conditions and to above 20 GPa for non-hydrostatic conditions. This transition is partially reversible below 2 GPa. The formed wBN has a high concentration of defects. For recovered samples, defects couple with the 532.18 nm excitation laser producing a heating effect, observed as a Raman downshift with increasing laser power.

The bulk modulus B_0 and pressure derivative of the bulk modulus B_0' of hBN are estimated to be 30.6 $\pm$ 0.5 GPa and 8.7 $\pm$ 0.7, respectively. The bulk modulus of wBN is estimated to be 392 $\pm$ 5 GPa, leading to a Vickers hardness of 68 $\pm$ 1 GPa. Extra diffraction lines are observed for hBN samples loaded with N_2, indicating a potential new structure arising from a reaction of N_2 with hBN, but Raman spectroscopy fails to corroborate this finding. The crystallinity of the hBN samples and the choice of pressure transmitting medium are shown to have little to no effect on the estimated physical properties of hBN.

Laser heating is performed on hBN with various sample assemblies. The effectiveness of different assemblies is discussed. NaCl is used as a pressure and temperature gauge local to the X-ray probe to contrast the stationary ruby pressure gauge and the non-local black body temperature measurement. A large contrast between the two temperature measurements yields doubt that the intended temperatures of around 2000 K are produced in the sample. Observation of the proposed high-pressure high-temperature transition to body-centered tetragonal BN or intercalated BN cannot be confirmed, likely due to insufficient heating.

The prospects for studying Li-BN intercalation compounds under extreme conditions is discussed. An initial experiment on the system studied with X-ray diffraction is unable to confirm heating of the material nor the presence of intercalation compounds.

Acknowledgements

I would foremost like to express my gratitude to professor Serge Desgreniers for supporting me and granting me this opportunity. His guidance and patience over the years cannot be understated and I will be eternally grateful.

I would like to recognize the Canadian Light source beamline scientists Dr. Ning Chen, Dr. Chang-Yong Kim, and Dr. Weifeng Chen at the Hard X-ray MicroAnalysis beamline for their help in carrying out X-ray diffraction experiments, and Dr. Scott Rosendahl and Dr. Stuart Read at the Mid infrared Spectromicroscopy beamline for their help in carrying out infrared spectroscopy experiments. I will extend this recognition to Dr. Jesse Smith, beamline scientist with the high pressure collaborative access team at the Advanced Photon Source, for help in carrying out X-ray diffraction and laser heating experiments.

I would like to thank Laurent Gagné-Dumais, Erin Flannigan, and Benoit Vanus for their feedback on select chapters, and for several years of friendship. Louis Jacques, for many long conversations on adjacent subjects to this work, usually new statistical concepts I will continue trying to wrap my head around for years to come.

I thank my colleagues and friends at the Laboratoire physique des solides denses. I will miss the long days and conversations in the office and lab with Maël Chow-Cloutier and Michael Tokiyoshi Hamel, and look forward to our relationships in the future. Your company has been deeply valued and though our projects differed greatly, I appreciate the lengths to which we could bounce ideas off one another.

This wouldn't have been possible without any of you, so once again, thank you.

"Ladies and Gentlemen, I stand before you now because I never stopped dawdling like an eight-year-old on a spring morning on his way to school. Anything can make me stop and look and wonder, and sometimes learn"

Cat's Cradle Kurt Vonnegut, 1963

Contents

List of Figures

List of Tables

List of Abbreviations

DAC	Diamond anvil cell
XRD	X-ray diffraction
EoS	Equation of state
IR	Infrared
FTIR	Fourier transform infrared
HP	High-pressure
HPHT	High-pressure high-temperature
GPa	Gigapascal
PTM	Pressure transmitting medium (or media)
hBN	Hexagonal boron nitride
wBN	Wurtzite boron nitride
bct-BN	Body centered tetragonal boron nitride
GIC	Graphite intercalation compound
BNIC	Boron nitride intercalation compound
pN	Polymeric nitrogen
FBZ	First Brillouin zone
LO	Longitudinal optical
TO	Transverse optical
FWHM	Full width at half maximum
S/N	Signal to noise ratio
CLS	Canadian Light Source
APS	Advanced Photon Source
LPSD	Laboratoire de physique des solides denses

List of Symbols

Symbol	Meaning	Common Units
P	Pressure	GPa
T	Temperature	K
B_0	Bulk modulus	GPa
B_0'	Pressure derivative of the bulk modulus	
G	Shear modulus	GPa
H_V	Vickers hardness	GPa
Z	Atomic number	
2Θ	Diffraction angle	degrees (^{o})
d	Interplanar distance	Å
a, b, c	Lattice parameter	Å
V	Volume	Å^3
ω	Frequency (wavenumber)	cm^{-1}
λ	Wavelength	nm

Chapter 1

Introduction

Phase transitions in materials lead to radical differences in properties. Through the use of extreme conditions, meaning pressures on the scale of 1 GPa or greater and temperatures between few Kelvin to several thousands of Kelvin, a wide range of range of material phases become accessible. One familiar example is with carbon. The low pressure, solid phase of carbon is graphite, commonly used as pencil lead. Graphite is composed of flat sheets of carbon atoms bonded to one another in a hexagonal order. These sheets are laid on top of one another with a fairly weak attractive force. This weak inter-sheet bonding is the reason why the material comes off so easily when pressed to paper. Above 5.5 GPa and 1800 K[1], graphite transforms into diamond. The two materials are identical in chemical composition, but quite different in terms of physical properties. These differences are owed to the crystallographic arrangement of the two solids. In graphite the atoms are only strongly bonded in 2-dimensional sheets, whereas in diamond the atoms are linked in a way that forms a 3-dimensional lattice. A very similar system is investigated in this thesis.

Extreme conditions on condensed matter has led to exciting developments in materials science worth mentioning here. It is under greatly elevated pressures that superconductors with the highest critical temperatures reported are formed, notably LaH_{10} at 250K and 170 GPa[2] and a recent report of superconductivity at room temperature in carbonaceous sulfur hydride at 155 GPa[3]. According to prevailing theory, even hydrogen should become a metal and superconductor at sufficient pressure[4]. In theory, this would be a room temperature superconductor, and would confirm that Jupiter's massive magnetic fields (which reach past across the orbits of nearby planets) is due a core of dense, metallic

hydrogen. The ongoing race for metallic hydrogen synthesis has seen many controversial reports[5,6], all being rightfully handed a wealth of skepticism[5,7]. Recent studies of the change of the band gap and infrared spectrum of pressurized hydrogen have been very promising regarding the realization of the metallization of hydrogen at 80K and 425 GPa[8], meaning if it hasn't yet been synthesized, it is quite close. Indeed, it is an exciting time to be researching materials under extreme conditions.

1.1 Motivations

Research at extreme conditions is heavily concerned with the generation of materials with novel properties, the study of why these properties exist, how they evolve, and how to take advantage of them in our less extreme living conditions. In such a way, pressure also presents itself as a useful tool that can be used for tuning material properties and extracting information about them. The materials we seek to create in the studies presented here have a wealth of properties of interest. These materials may be more effective abrasives than any on the market or higher energetically dense and more stable than any other non-nuclear explosives. We may be interested in their novel, directionally dependent electronic properties, or even just simply to test the effectiveness of models and their simulations.

1.1.1 Ultrahard Materials

Hardness is classified by different scales depending on the experimental method, such as the Mohs scale, which is measured by the ability to scratch another material, or the Vickers scale, which measures the amount of plastic deformation caused by an indentation. Anything with a Vickers hardness H_V above 40 GPa is considered superhard[9]. Hard and superhard materials are incredibly important for industrial applications, being used

as abrasives, cutting tips, and polishing agents to cut away material from otherwise very strong surfaces. An abrasive that is too soft (not hard enough) will be machined down by the material that is intended to be machined, so the harder the material to be machined machine, the harder the abrasive is needed to be. Due to chemical inertness being a common property among superhard materials, they are also used as chemical and physical wear-resistance coatings. It has been noted that the creation of the industry of synthetic superhard materials is one of the greatest stages of the technological revolution in the 20th century[10], and with the accelerating manufacturing activities and environmental demand for hard materials without need for coolants, the global demand for new and improved hard materials continues to expand[11–13].

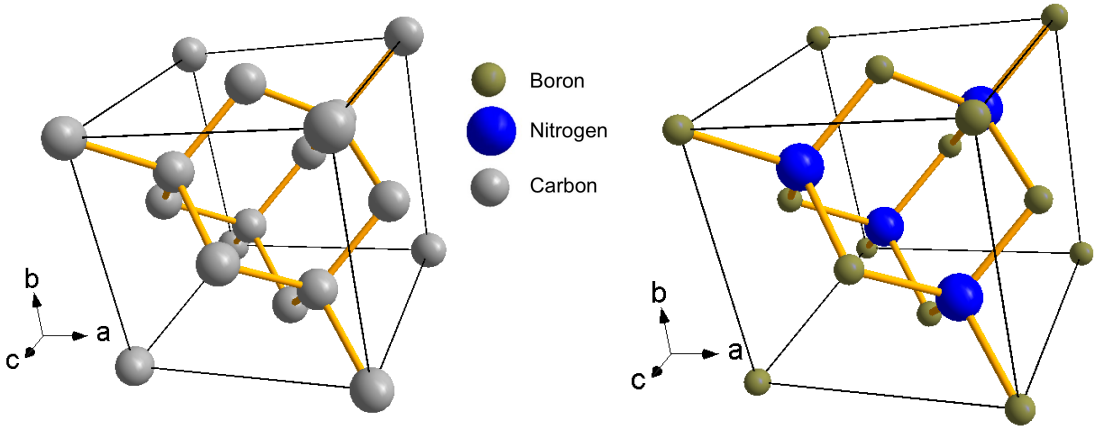

(A) Diamond.

(B) cBN.

FIGURE 1.1: Unit cells for the crystal structures of diamond and cubic boron nitride (cBN), viewed along the (1 1 2) direction. Both consist of a face-centered cubic Bravais lattice with 4 additional atoms within the unit cell, creating the diamond structure for monotonic species, or zinc blende structure for diatomic species like BN. Leaving each atom with 4 nearest neighboring atoms, there is naturally sp^3 bonding between the atoms.

Among hard materials, diamond is the champion. Possessing a hardness of 60-120 GPa, it surpasses any other material found in nature or yet developed; it is unlikely that it is possible to ever beat it by much[10]. As a result, diamond is very useful as an abrasive and is heavily used across many industries. Unfortunately, diamond suffers some

issues as an abrasive material. Notably, diamond has poor thermal stability, as it readily converts to graphite around 700°C in air, slightly higher than what is possible in a conventional oven. Furthermore, diamond is unsuitable for working in iron-rich environments as it reacts and degrades, forming carbides with the iron. This is an issue for using it as a machining abrasive, considering how pervasive steel, a hard, high iron metal, is as a building material, and in need of lots of machining.

The second most prominent ultrahard material would be cubic boron nitride (cBN), discovered in the early sixties[14]. With both composing elements lying directly on either side of carbon on the periodic table, it is isoelectronic to diamond. It has the zinc blende structure, which makes it isostructural to diamond as well, as shown in Figure 1.1. Like diamond, cBN is obtained at high pressure, starting from the low pressure form of hBN. While cBN is indeed an ultrahard material, its intrinsic hardness is lower than that of diamond, only 30-45 GPa[15], due to the partial ionicity of the B-N bonds. cBN is still the second hardest commercial superhard material[11]. Furthermore, single crystal cBN has a fracture toughness about half that of diamond, though polycrystalline cBN with binders shows higher fracture toughness at no expense to the hardness[16,17].

As shown in Figure 1.2, recent material designs based on cBN or diamond has increased the upper limit for hardness, though not without similar drawbacks to the original materials. New materials with similar hardness to cBN and diamond would hopefully provide a way around the issues associated with the current ultrahard material options, as well as more selection for the global demand. These materials would therefore need to maintain a hardness comparable to those in use, while being more thermally stable than diamond.

By inspecting the compression of a solid, it is possible to uncover elastic parameters for the material such as the bulk modulus, the property characterizing the compressibility and part of the picture necessary for determining how hard a material is. Though there are many different models for defining hardness, most of them can be expressed as a

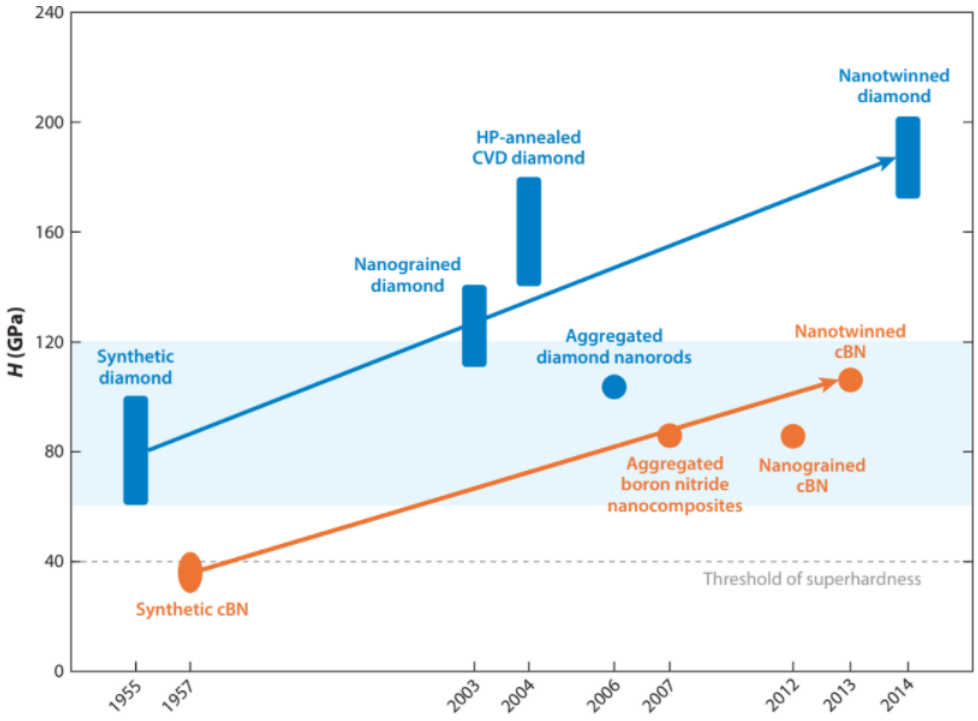

FIGURE 1.2: A timeline of the synthesis of diamond and cBN based ultra-hard materials and their corresponding hardness (reproduced from *Zhao et al.*, 2016[11]). The cyan region shows the hardness range of natural diamond.

relation between the aforementioned bulk modulus and the shear modulus defined as how much the material deforms under sheer strain rather than pressure. Chen's model for hardness[18], defined as

$$H_V = 2(\frac{G^3}{B^2})^{0.585} - 3 \tag{1.1}$$

where H_V is the calculated Vickers hardness, G is the shear modulus, and B is the bulk modulus. Using this equation, it is possible to estimate the hardness based on observed elastic parameters.

1.1.2 Boron Nitrides of Interest

Hexagonal Boron Nitride (hBN)

The low pressure phase of hexagonal boron nitride (hBN), termed "white graphite", lives up to it's name. Layered hexagonal sheets of sp^2 bonded B-N makes up the ambient stable structure of BN. The point group of the hBN lattice is D_{6h}[19], due to the alternating stacking of layers such that the position of each B atom in one layer is the same as a N atom in the following, and vice versa, as shown in Figure 1.3. This does make it structurally different from graphite lattice, whose point group is D_{3h}. the hBN lattice would have this point group if the stacked sheets instead were aligned by elemental type species along the c-axis[19].

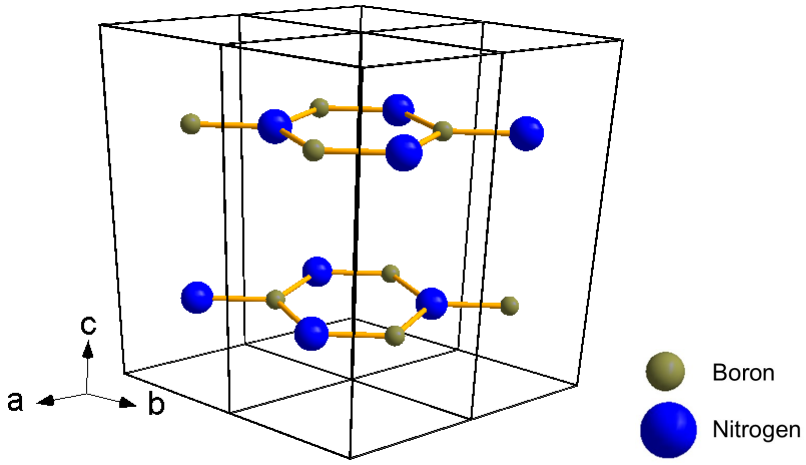

FIGURE 1.3: The structure of hBN. Note the elemental alternation in the c-axis, which leads to a slight change in structure compared to graphite.

The fast growing field of atomically thin 2D materials was first nucleated by the experimental discovery of graphene[20]. By exfoliating the 2D crystal down to one or only a few sheets, the remaining material exhibits unusual and wonderful new properties. hBN, being structurally and electronically similar to graphite, was a natural addition to 2D and layered devices, either as a substrate[21] or the material in focus. Indeed, it possesses incredible strength and toughness, for instance[22]. Furthermore, hBN is an indirect

bandgap semiconductor with a range of phonon-assisted optical transitions[23], and its distinctive electronic structure provides a rich phonon-assisted emission spectrum[24]. hBN is of great interest for use in infrared nanophotonics, as well as a single-photon and ultraviolet emitter[25]. hBN has even been used to make quantum dots[26]. Needless to say that the study of the physical properties of hBN at extreme conditions are of interest as it could lead to other significant discoveries, such as how to effectively tune these properties. The experiments presented in this thesis begin with subjecting hBN to extreme conditions in order to study it's properties and to characterize the transition from hBN to other phases.

Wurtzite Boron Nitride (wBN)

Just like for graphite, when several gigapascals of pressure are applied to hBN, a transition from sp^2 to sp^3 bonded B-N occurs[27]. Although with graphite the application of extreme conditions would produce diamond outright, under high pressure at ambient temperature hBN converts instead to a wurtzite structure. The transformed wurtzite boron nitride (wBN) is structurally similar to the phase of "hexagonal diamond" for the carbon system, a mineral phase known as lonsdaleite.

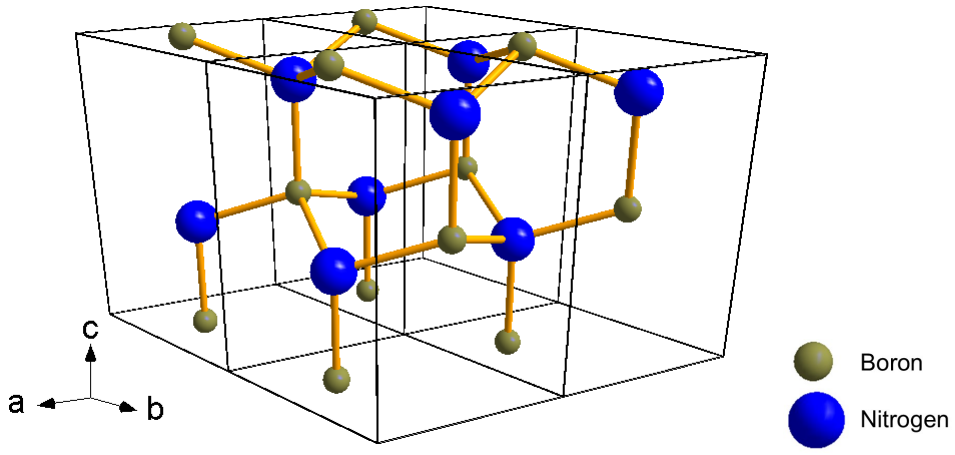

FIGURE 1.4: The structure of wBN. Note the angle between a and b axes of the unit cell being 30^o off of 90^o due to the hexagonal structure, separating the phase from the one seen in Figure 1.1b.

Simulations have shown potential for both wBN and lonsdaleite to be harder than diamond[28]. With wBN having a greater thermal stability than that of diamond, it is a promising candidate as a novel ultrahard material.

Other semiconducting group-III nitrides, such as GaN, AlN, and InN, have been instrumental in the development of optoelectronics; they all are stable in the wurtzite structure. It is thus essential to understand and determine the characteristics of wBN. Unfortunately, due to the difficulty in synthesizing wBN in more than small amounts (such as a large, high-quality crystal), there have been few studies into the physical properties of wBN[29]. Composites of cBN and wBN have already shown the sign of hardness closer to that of single crystal and polycrystalline diamond than for any other forms of cBN[30]. The hardness of wBN is yet to be determined and understanding how it contributes to the elevation of hardness in a nanocomposite is unclear.

Body-Centered Tetragonal Boron Nitride (bct-BN)

Although hBN, cBN, and wBN form the "holy trinity" of BN phases, there exists a number of other observed and conjectured phases. BN has been reported in rhombohedral[31] and orthorhombic[32] configurations, while other designations such as the disordered turbostratic BN exist. However, one proposed phase is of specific interest in this thesis, which will be referred to henceforward as the body-centered tetragonal BN (bct-BN). Initially proposed in 2011 under different monikers by two separate groups[33,34], the bct phase of BN is predicted to be a metastable, high pressure and high temperature (HPHT) phase of BN. Computer simulations have shown that the type of deformation leading to a high pressure phase transition is what leads to the different phase structure[33]. Whereas chair-like deformation (as defined in the article[33]) is what usually causes the transition to a wurtzite crystalline structure, with sufficient applied temperature, the deformation would instead be boat-type, leading to the tetragonal structure. Simulations proposed that bct-BN is actually a mechanically stable intermediate phase in the transition between hBN

and wBN[34]. Where the wurtzite structure can be recognized by six-membered rings of B and N atoms, the newly formed structure features distinctive 4- and 8- membered rings along a shared axis, making a $P4_2/mnm$ symmetry isostructural to the β phase of BeO (and as such, was labeled as "β-BeO BN" in Hromadová's discussions).

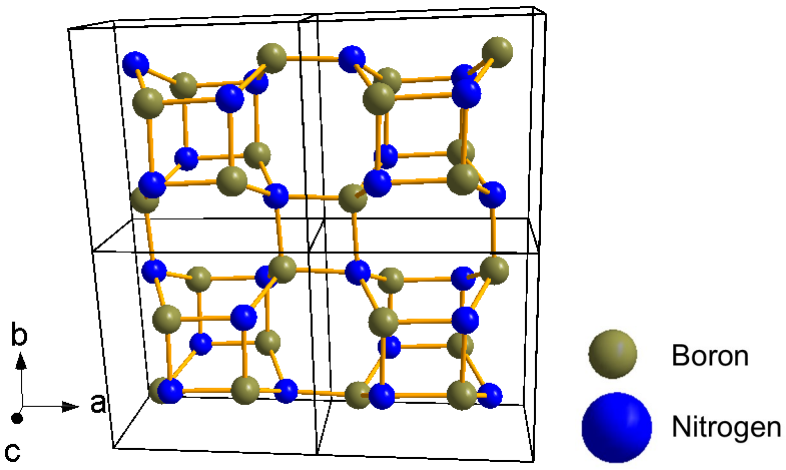

FIGURE 1.5: bctBN as viewed from the (1 2 4) direction.

Hromadová's simulations[33] show that the high pressure deformations change from chair-type to boat-type around 900 K, and around 1000 K it is boat-type dominant. They calculate that bct-BN should actually be more thermally stable than wBN, but only once the kinetic barriers are overcome through heating. However, it seems as if the transition has to be nucleated from hBN, rather than just setting the conditions right, making the challenge of the bct-BN synthesis non-trivial. When increasing the temperature too high at lower pressures, and the hBN converts to cBN[35] - no bct-BN; increasing the pressure too high below 1000 K, converts the hBN to wBN - no bct-BN here either. This bct-BN is suspected to be ultrahard, although not as hard as the wurtzite or zinc-blende counterparts, with bulk modulus lower by about 7%[33]. The calculated Vickers hardness of bct-BN is calculated to be 65.2 GPa, very comparable to that of cBN, while having a much higher shear strength than cBN: 68.6 GPa for bct-BN, as compared to 21.6 GPa for cBN[34], making it a much more optimal abrasive material.

The experiments in this thesis are designed for the study of these three phases in mind (hBN, wBN, and bct-BN). The goal is to uncover their properties and to characterize the phase transitions between them, as well as uncovering the potential for forming new, high energy density materials starting from hBN.

1.1.3 Polymeric Nitrogen and Energetic Materials

High energy density materials is one of the areas of highest interest within the field of extreme conditions condensed matter. Such materials are used as higher-efficiency chemical fuels, for instance. Pressure provides a route not only to the synthesis of novel dense, higher energy materials, but also to tuning their properties. Furthermore, high pressure and temperature modification allows for the effective simulation of the atmosphere upon detonation, enabling the study of the physics under those conditions. Insofar, most modern advances in obtaining such materials has been through use of compounds with high nitrogen content[36]. This nitrogen backbone provides stored energy from the conversion of nitrogen double bonds to molecular nitrogen triple bonds.

As predicted by McMahan *et al.*[37], sufficiently high density (such found under incredible pressures) of molecular nitrogen causes the intra-molecular forces to be comparable to inter-molecular forces, referred to as electronic frustration. Sufficient frustration causes the molecular nitrogen to dissociate to form a monatomic nitrogen lattice of single bonded nitrogen. This monatomic lattice network would be like a polymer of nitrogen (pN), with many stable forms predicted, including those with the A7 (arsenic), BP (black phosphorous), cg (cubic-gauche), and ch (trans-cis chain) structures[38]. A material containing such nitrogen single bonds would present an energy density many times that of standard explosives, nearly 7 times that of TNT per unit mass[39].

Many forms of polymeric nitrogen have since been discovered, with many of them stable to relatively low pressure conditions, but none yet that are stable under ambient

atmosphere. Above 150 GPa at room temperature, nitrogen takes on an opaque, electrically conductive form[40], coined the η phase. The η phase was proven to be non-molecular, amorphous and consisting of polymeric single-bonded nitrogen[41]. The η was shown to be metastable to room pressure but only under 100 K, while at room temperature it converts to a non-polymeric phase below 50 GPa[42].

A few years after the discovery of the η phase of nitrogen, the cubic-gauche (cg) form was first created above 110 GPa and 2000 K[43]. Under room temperature, the phase was metastable down to 42 GPa, however the illumination of even a weak laser was enough to convert it back to molecular nitrogen. At 140 K it was shown that this was stable down to possibly less than 25 GPa.

It was a decade before another phase of pN was created; in 2014, the layered polymeric (LP) structure of nitrogen was created by laser heating nitrogen at 120-180 GPa to temperatures as high as 3000 K[44]. This phase was shown to be about 7.8% denser and about 22.5% stiffer than cBN, hopefully meaning it's more stable. Very recently, a modification to this phase was created in the form of the hexagonal layered polymeric nitrogen (HLP-N). Above 240 GPa, laser heating samples of pure nitrogen produced a new polymeric phase in a tetragonal arrangement, metastable down to at least 66 GPa under room temperature[45].

Most recently, and perhaps most excitingly, one more of Mailhiot's[38] predicted polymeric structures was created. Structurally analogical to the 2D phase of black phosphorous, the black phosphorous phase of nitrogen (bp-N) was only recently synthesize during laser heating above 140 GPa[46,47]. The phase was shown to be stable to pressures as low as 46 GPa. It would be interesting to use a layered system as hBN to further confine and perhaps facilitate the dissociation of triply bonded nitrogen molecules in the solid-state.

The pressures and temperatures necessary to create polymeric nitrogen that is yet to be stabilized at ambient conditions makes it a serious challenge for real-life applications. As such, there is great interest in exploring other nitrogen dense materials to produce single

bonded nitrogen compounds that could be formed at and be metastable to much lower respective pressures.

1.1.4 Nitrogen Intercalation in hBN

Following the insight of McMahan *et al.*[37], nitrogen needs to be in high density in order to produce the electronic frustration on the molecular nitrogen bonds that would lead to dissociation into nitrogen single bonds. Starting with a high nitrogen density solid could potentially lead to a higher density of nitrogen upon sample loading than otherwise starting with pressurized nitrogen. This was the inspiration in using, for instance, cyanuric triazide, a compound consisting of a C_3N_3 with three azide (N_3^-) arms attached to it, resulting in a C_3N_{12} stoichiometry. Under pressure, in the solid state, the azide arms close in on the ring, forming tri-tetrazole, composed of 3 linked CN_4 tetrazole rings. The nitrogens in the new external rings sharing electrons keeping them not double bonded, but not single bonded either. This high pressure phase has been shown to revert back to cyanuric triazide as low as 5 GPa[48], much lower than any pN polytypes.

Recently, lithium nitrides in a nitrogen atmosphere under pressure provided a really close look at metastable single bonded nitrogen compounds. Under increasing pressure, the stable stoichiometries of these lithium nitrides become more and more dominantly composed of nitrogen. Up to 75 GPa, the initial stoichiometry Li_3N converted to LiN, LiN_2, and eventually to LiN_5, at which point the molecular bonds were overwhelmingly nitrogen single bonds[49]. Even more surprisingly, LiN_5 remained stable down to room pressure while under a controlled argon atmosphere[50]. Unfortunately, upon exposure to air, the LiN_5 sample decomposed. This nonetheless shows the great promise of nitrogen dense materials under pressure for the formation and stabilization of single bonded nitrogen compounds. Another proposed but in-so far unstudied nitrogen dense materials class is that of nitrogen intercalant materials.

In a trio of papers published over the past 5 years[51–53], researchers proposed an alternative form hBN as a potential single bonded nitrogen host under pressure, specifically specifically referring to nitrogen-intercalated hBN. Intercalation refers to the introduction of external elements and molecules into the network of a material. In this case, between the bound hBN sheets. In the mentioned papers, it was shown that the intercalation of nitrogen to the hBN network leads to different phases at high pressure conditions.

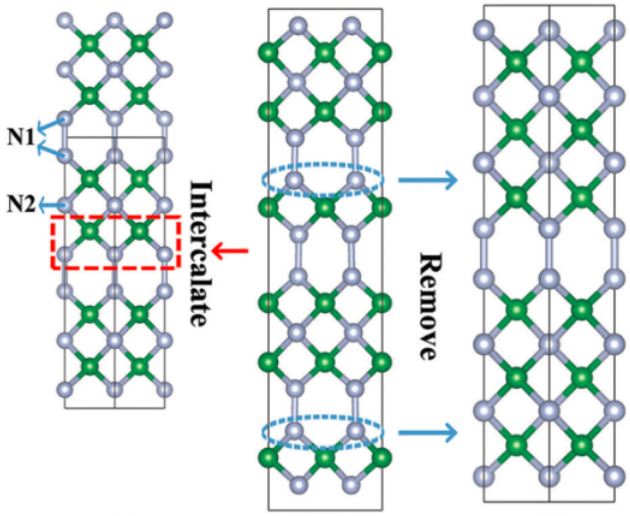

FIGURE 1.6: Structures of B_2N_3, B_3N_5, and B_3N_4, in the respective order. The difference between the 3 structures is demonstrated fairly easily by considering them as sections of cBN joined by single bonded nitrogen joints. By adding an extra cBN-type layer to the B_3N_5, the B_2N_3 structure is created. If instead one portion of the nitrogen bonds was removed, the resulting structure would be the B_3N_4 structure. Reproduced from Lin *et al.*, 2019[52].

Other materials have already been intercalated into hBN, such as a specific type of acids[54], as well as lithium though none[55], though no species nitrogen. Molecular nitrogen, however, stands to still be introduced within the hBN network.

The specific structures that are most energetically favorable depend on the distribution of nitrogen between the hBN sheets, but 3D networks with B_3N_5, B_3N_4, and B_2N_3 stoichiometries are predicted to be metastable to room conditions. This new class of materials would exhibit single bonded nitrogen linking sections of cBN-like BN sections, as

shown in Figure 1.6. While the material itself would be ultrahard, with a predicted hardness between 42-78.5 GPa (higher than that of cBN!). Due to the single bonded nitrogen, these materials would be incredibly energy dense, with an energy density of 2.95-3.44 kJ/g, meanwhile the electronic properties are very interesting. These materials would exhibit 2D metallicity, insulated by a small band gap insulation in the other direction. The possibilities for these materials is quite expansive and their creation could herald a slew of new technologies. As such, one major goal of this thesis is to investigate the potential routes to creating nitrogen-intercalated BN structures and, likewise, the predicted high pressure phases.

1.2 Thesis Contributions

This thesis serves to communicate the research done in examining the physical properties of BN compounds under extreme conditions. These studies have been performed using X-ray diffraction and spectroscopic methods on a wealth of different samples. Foremost, X-ray diffraction and Raman and infrared spectroscopy have been used to investigate the structural and vibrational properties of hBN. Samples of hBN of various crystalline states in various media have been subjected to high pressures, some under ambient temperature and others at high temperatures as a result of laser heating, in search of wurtzite and body-centered tetragonal phases of BN, and also to explore the conditions to promote N_2 intercalation. Intercalation has been attempted with nitrogen and lithium species in the hopes of creating novel compounds.

Chapter 2 will discuss the methods used in this thesis to study the solids under extreme conditions. In Chapter 3, the X-ray diffraction experiments and result for samples at ambient temperature will be discussed, as well as the physical properties examined from the following analysis. In Chapter 4, the results of high pressure Raman and IR

spectroscopy experiments will be shown and discussed, including the optical characteristics of the phase transitions observed. In Chapter 5, the X-ray diffraction and laser heating experiments will be discussed and the results will be presented. In Chapter 6, the results of compressing a mixture of lithium and hBN will be discussed. Finally, a summary of the previously discussed results, outstanding questions, and suggestions for future research are presented in Chapter 7.

Bibliography

1. Bundy, F. P. Pressure-Temperature Phase Diagram of Elemental Carbon. *Physica A: Statistical Mechanics and its Applications* **156,** 169–178. ISSN: 0378-4371 (Mar. 1989).

2. Drozdov, A. P. *et al.* Superconductivity at 250 K in Lanthanum Hydride under High Pressures. *Nature* **569,** 528–531. ISSN: 1476-4687 (May 2019).

3. Snider, E. *et al.* Room-Temperature Superconductivity in a Carbonaceous Sulfur Hydride. *Nature* **586,** 373–377. ISSN: 1476-4687 (Oct. 2020).

4. Ashcroft, N. W. Metallic Hydrogen: A High-Temperature Superconductor? *Phys. Rev. Lett.* **21,** 1748–1749 (Dec. 1968).

5. Dias, R. P. & Silvera, I. F. Observation of the Wigner-Huntington Transition to Metallic Hydrogen. *Science* **355,** 715–718. ISSN: 0036-8075, 1095-9203 (Feb. 2017).

6. Eremets, M. I. & Troyan, I. A. Conductive Dense Hydrogen. *Nat Mater* **10,** 927–931. ISSN: 1476-1122 (Nov. 2011).

7. Castelvecchi, D. Physicists Doubt Bold Report of Metallic Hydrogen. *Nat. News* **542,** 17 (Feb. 2017).

8. Loubeyre, P., Occelli, F. & Dumas, P. Synchrotron Infrared Spectroscopic Evidence of the Probable Transition to Metal Hydrogen. *Nature* **577,** 631–635. ISSN: 1476-4687 (Jan. 2020).

9. Xu, B. & Tian, Y. Superhard Materials: Recent Research Progress and Prospects. *Sci. China Mater.* **58,** 132–142. ISSN: 2199-4501 (Feb. 2015).

10. Brazhkin, V. V. & Solozhenko, V. L. Myths about New Ultrahard Phases: Why Materials That Are Significantly Superior to Diamond in Elastic Moduli and Hardness Are Impossible. *Journal of Applied Physics* **125,** 130901. ISSN: 0021-8979 (Apr. 2019).

11. Zhao, Z., Xu, B. & Tian, Y. Recent Advances in Superhard Materials. *Annu. Rev. Mater. Res.* **46,** 383–406. ISSN: 1531-7331 (July 2016).

12. Solozhenko, V. L. & Gregoryanz, E. Synthesis of Superhard Materials. *Materials Today* **8,** 44–51. ISSN: 1369-7021 (Nov. 2005).

13. Haines, J., Léger, J.-M. & Bocquillon, G. Synthesis and Design of Superhard Materials. *Annu. Rev. Mater. Res.* **31,** 1–23. ISSN: 1531-7331 (Aug. 2001).

14. Wentorf, R. H. Synthesis of the Cubic Form of Boron Nitride. *J. Chem. Phys.* **34,** 809–812. ISSN: 0021-9606 (Mar. 1961).

15. Harris, T. K., Brookes, E. J. & Taylor, C. J. The Effect of Temperature on the Hardness of Polycrystalline Cubic Boron Nitride Cutting Tool Materials. *International Journal of Refractory Metals and Hard Materials* **22,** 105–110. ISSN: 0263-4368 (Jan. 2004).

16. Liew, W. Y. H., Yuan, S. & Ngoi, B. K. A. Evaluation of Machining Performance of STAVAX with PCBN Tools. *Int J Adv Manuf Technol* **23,** 11–19. ISSN: 1433-3015 (Jan. 2004).

17. Wentorf, R. H., Devries, R. C. & Bundy, F. P. Sintered Superhard Materials. *Science* **208,** 873–880. ISSN: 0036-8075 (May 1980).

18. Chen, X.-Q., Niu, H., Li, D. & Li, Y. Modeling Hardness of Polycrystalline Materials and Bulk Metallic Glasses. *Intermetallics* **19,** 1275–1281. ISSN: 0966-9795 (Sept. 2011).

19. Geick, R., Perry, C. H. & Rupprecht, G. Normal Modes in Hexagonal Boron Nitride. *Phys. Rev.* **146,** 543–547. ISSN: 0031-899X (June 1966).

20. Novoselov, K. S. *et al.* Electric Field Effect in Atomically Thin Carbon Films. *Science* **306,** 666–669. ISSN: 0036-8075, 1095-9203 (Oct. 2004).

21. Dean, C. R. *et al.* Boron Nitride Substrates for High-Quality Graphene Electronics. *Nat. Nanotechnol.* **5,** 722–726. ISSN: 1748-3395 (Oct. 2010).

22. Huang, Y. *et al.* Thin Boron Nitride Nanotubes with Exceptionally High Strength and Toughness. *Nanoscale* **5,** 4840. ISSN: 2040-3364, 2040-3372 (2013).

23. Cassabois, G., Valvin, P. & Gil, B. Hexagonal Boron Nitride Is an Indirect Bandgap Semiconductor. *Nature Photonics* **10.** Comment: To appear in Nature Photonics, 262–266. ISSN: 1749-4885, 1749-4893. arXiv: 1512.02962 (Apr. 2016).

24. Vuong, T. Q. P. *et al.* Overtones of Interlayer Shear Modes in the Phonon-Assisted Emission Spectrum of Hexagonal Boron Nitride. *Phys. Rev. B* **95,** 045207. ISSN: 2469-9950, 2469-9969 (Jan. 2017).

25. Caldwell, J. D. *et al.* Photonics with Hexagonal Boron Nitride. *Nat. Rev. Mater.* **4,** 552–567. ISSN: 2058-8437 (Aug. 2019).

26. Lei, Z., Xu, S., Wan, J. & Wu, P. Facile Preparation and Multifunctional Applications of Boron Nitride Quantum Dots. *Nanoscale* **7,** 18902–18907. ISSN: 2040-3372 (Nov. 2015).

27. Meng, Y. *et al.* The Formation of Sp 3 Bonding in Compressed BN. *Nat. Mater.* **3,** 111–114. ISSN: 1476-4660 (Feb. 2004).

28. Pan, Z., Sun, H., Zhang, Y. & Chen, C. Harder than Diamond: Superior Indentation Strength of Wurtzite BN and Lonsdaleite. *Phys. Rev. Lett.* **102,** 055503 (Feb. 2009).

29. Nagakubo, A., Ogi, H., Sumiya, H., Kusakabe, K. & Hirao, M. Elastic Constants of Cubic and Wurtzite Boron Nitrides. *Appl. Phys. Lett.* **102,** 241909. ISSN: 0003-6951 (June 2013).

30. Dubrovinskaia, N. *et al.* Superhard Nanocomposite of Dense Polymorphs of Boron Nitride: Noncarbon Material Has Reached Diamond Hardness. *Appl. Phys. Lett.* **90,** 101912. ISSN: 0003-6951 (Mar. 2007).

31. Kurakevych, O. O. & Solozhenko, V. L. Rhombohedral Boron Subnitride, B13N2, by X-Ray Powder Diffraction. *Acta Cryst C* **63,** i80–i82. ISSN: 0108-2701 (Sept. 2007).

32. Zhang, Z. *et al.* Orthorhombic BN: A Novel Superhard Sp3 Boron Nitride Allotrope. *Physics Letters A* **378,** 741–744. ISSN: 0375-9601 (Feb. 2014).

33. Hromadová, L. & Martoňák, R. Pressure-Induced Structural Transitions in BN from *Ab Initio* Metadynamics. *Phys. Rev. B* **84,** 224108. ISSN: 1098-0121, 1550-235X (Dec. 2011).

34. Wen, B., Zhao, J., Melnik, R. & Tian, Y. Body-Centered Tetragonal B_2N_2: A Novel Sp3 Bonding Boron Nitride Polymorph. *Phys. Chem. Chem. Phys.* **13,** 14565. ISSN: 1463-9076, 1463-9084 (2011).

35. He, L.-L., Akaishi, M. & Horiuchi, S. Structural Evolution in Boron Nitrides during the Hexagonal-Cubic Phase Transition under High Pressure at High Temperature. *Microsc. Res. Tech.* **40,** 243–250. ISSN: 1097-0029 (1998).

36. Badgujar, D., Talawar, M., Asthana, S. & Mahulikar, P. Advances in Science and Technology of Modern Energetic Materials: An Overview. *Journal of Hazardous Materials* **151,** 289–305. ISSN: 03043894 (Mar. 2008).

37. McMahan, A. K. & LeSar, R. Pressure Dissociation of Solid Nitrogen under 1 Mbar. *Phys. Rev. Lett.* **54,** 1929–1932 (Apr. 1985).

38. Mailhiot, C., Yang, L. H. & McMahan, A. K. Polymeric Nitrogen. *Phys. Rev. B* **46,** 14419–14435. ISSN: 0163-1829, 1095-3795 (Dec. 1992).

39. Mao, H.-K., Ji, C., Li, B., Liu, G. & Gregoryanz, E. Extreme Energetic Materials at Ultrahigh Pressures. *Engineering*, S2095809920301880. ISSN: 20958099 (July 2020).

40. Goncharov, A. F., Gregoryanz, E., Mao, H.-k., Liu, Z. & Hemley, R. J. Optical Evidence for a Nonmolecular Phase of Nitrogen above 150 GPa. *Phys. Rev. Lett.* **85,** 1262–1265. ISSN: 0031-9007, 1079-7114 (Aug. 2000).

41. Gregoryanz, E. *et al.* High P-T Transformations of Nitrogen to 170GPa. *The Journal of Chemical Physics* **126,** 184505. ISSN: 0021-9606, 1089-7690 (May 2007).

42. Eremets, M. I., Hemley, R. J., Mao, H.-k. & Gregoryanz, E. Semiconducting Non-Molecular Nitrogen up to 240 GPa and Its Low-Pressure Stability. *Nature* **411,** 170–174. ISSN: 0028-0836, 1476-4687 (May 2001).

43. Eremets, M. I., Gavriliuk, A. G., Trojan, I. A., Dzivenko, D. A. & Boehler, R. Single-Bonded Cubic Form of Nitrogen. *Nature Mater* **3,** 558–563. ISSN: 1476-1122, 1476-4660 (Aug. 2004).

44. Tomasino, D., Kim, M., Smith, J. & Yoo, C.-S. Pressure-Induced Symmetry-Lowering Transition in Dense Nitrogen to Layered Polymeric Nitrogen (LP-N) with Colossal Raman Intensity. *Phys. Rev. Lett.* **113,** 205502. ISSN: 0031-9007, 1079-7114 (Nov. 2014).

45. Laniel, D., Geneste, G., Weck, G., Mezouar, M. & Loubeyre, P. Hexagonal Layered Polymeric Nitrogen Phase Synthesized near 250 GPa. *Phys. Rev. Lett.* **122,** 066001. ISSN: 0031-9007, 1079-7114 (Feb. 2019).

46. Ji, C. *et al.* Nitrogen in Black Phosphorus Structure. *Sci Adv* **6,** eaba9206 (June 2020).

47. Laniel, D. *et al.* High-Pressure Polymeric Nitrogen Allotrope with the Black Phosphorus Structure. *Phys. Rev. Lett.* **124,** 216001. ISSN: 0031-9007, 1079-7114 (May 2020).

48. Laniel, D. *et al.* High Pressure Study of a Highly Energetic Nitrogen-Rich Carbon Nitride, Cyanuric Triazide. *J. Chem. Phys.* **141,** 234506. ISSN: 0021-9606 (Dec. 2014).

49. Laniel, D., Weck, G. & Loubeyre, P. Direct Reaction of Nitrogen and Lithium up to 75 GPa: Synthesis of the Li_3N, LiN, LiN_2, and LiN_5 Compounds. *Inorg. Chem.* **57,** 10685–10693. ISSN: 0020-1669, 1520-510X (Sept. 2018).

50. Laniel, D., Weck, G., Gaiffe, G., Garbarino, G. & Loubeyre, P. High-Pressure Synthesized Lithium Pentazolate Compound Metastable under Ambient Conditions. *J. Phys. Chem. Lett.* **9,** 1600–1604. ISSN: 1948-7185 (Apr. 2018).

51. Li, Y., Hao, J., Liu, H., Lu, S. & Tse, J. S. High-Energy Density and Superhard Nitrogen-Rich B-N Compounds. *Phys. Rev. Lett.* **115,** 105502. ISSN: 0031-9007, 1079-7114 (Sept. 2015).

52. Lin, S. *et al.* Prediction of Superhard B_2N_3 with Two-Dimensional Metallicity. *J. Mater. Chem. C* **7,** 4527–4532. ISSN: 2050-7526, 2050-7534 (2019).

53. Xie, C. *et al.* Superhard Three-Dimensional B_3N_4 with Two-Dimensional Metallicity. *J. Mater. Chem. C* **5,** 5897–5901. ISSN: 2050-7526, 2050-7534 (2017).

54. Kovtyukhova, N. I. *et al.* Reversible Intercalation of Hexagonal Boron Nitride with Brønsted Acids. *J. Am. Chem. Soc.* **135,** 8372–8381. ISSN: 0002-7863, 1520-5126 (June 2013).

55. Sumiyoshi, A., Hyodo, H. & Kimura, K. Li-Intercalation into Hexagonal Boron Nitride. *Journal of Physics and Chemistry of Solids* **71,** 569–571. ISSN: 00223697 (Apr. 2010).

Chapter 2

Theory and Experimental Techniques

The word "crystal" appears many times within this text and as such it would be irresponsible not to clearly define the term. Simply stated, a crystal is any solid with a regular, periodic arrangement. In spite of the second law of thermodynamics, the natural state of most pure solids is an ordered, crystalline one. This underlying order not only allows us to study the properties of materials to a profound level, but is also the reason for a great portion of a material's properties. The first section of this chapter will detail how atoms are arranged in a crystalline structure and the impact it has on material properties in general. The latter half of the chapter will then give the details of the experimental methods used to study these materials.

2.1 A Brief Introduction to the Solid State

2.1.1 Crystal Structure

The arrangement of a crystal structure is usually explained in terms of a unit cell. The unit cell is a small volume containing atoms which can be translated along given axes to describe the entire system. The unit cell is characterized by six parameters, three which are length of the orthogonal vertexes, defined as a, b, and c, and three which are the angles between vertexes, α, β, and γ, which are the respective angles between b and c, a and c, and a and b, as demonstrated in Figure 2.1. Based on these 6 parameters, crystal structures are organized into 7 crystal systems. The structures are then further divided into a total

of 14 lattice types based on the arrangement of lattice points within the cell refereed to as the Bravais lattices, listed in Table 2.1.

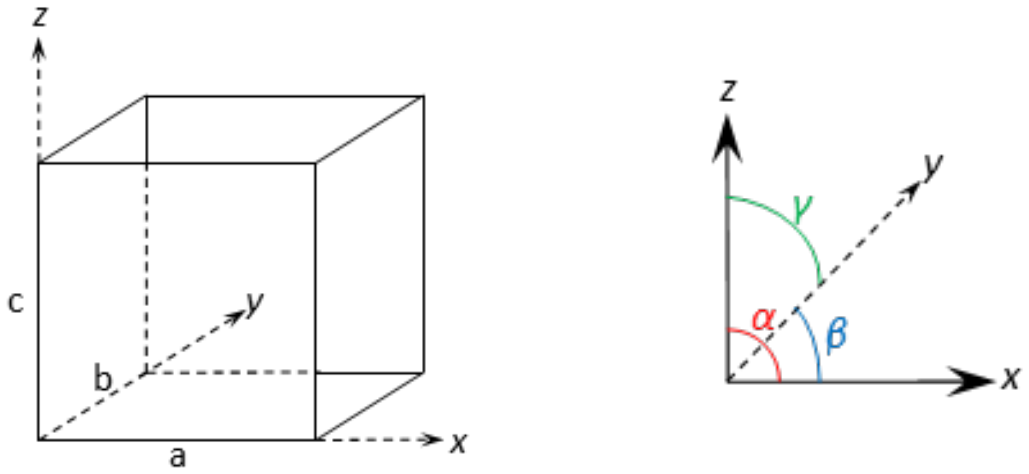

FIGURE 2.1: Schematic of a basic unit cell, presenting the relation between each of the six structural parameters.

The simplest of the crystal systems is the cubic system, where $a = b = c$ and $\alpha = \beta = \gamma = 90^o$, and the most complicated is the triclinic system, where none of the six parameters are equal. The cubic lattice itself is not a Bravais lattice as there is 3 potential modifications of it depending on the arrangement of points within, be they atoms or molecules. Placing an additional lattice point within the center (0.5a, 0.5b, 0.5c) leads to the Body-Centered (BC) Cubic, whereas having an additional lattice point in the center of each face, that is to say at (0.5a, 0.5b, 0c), (0a, 0.5b, 0.5c), and (0.5a, 0b, 0.5c), leads to the Face-Centered (FC) Cubic Bravais lattice. No additional lattice points in a cubic unit cell creates the Simple (S) Cubic Bravais Lattice.

With a crystal structure in place, any (x,y,z) position within the unit cell should be described instead as $(\frac{x}{a},\frac{y}{b},\frac{z}{c})$ such that an atom within the center for a BCC unit cell, for example, would be at the position (0.5,0.5,0.5). There need not be an atom or molecule at every lattice point of a given Bravais lattice for it to be an appropriate description, nor must atoms and molecules be placed strictly at those points.A given basis, defined with

Lattice type	Parameters	Angles	Bravais Lattice types
Cubic	$a = b = c$	$\alpha = \beta = \gamma = 90^0$	S, BC, FC
Rhombohedral (trigonal)	$a = b = c$	$(\alpha = \beta = \gamma) \neq 90^0$	S
Tetragonal	$a = b \neq c$	$\alpha = \beta = \gamma = 90^0$	S, BC
Hexagonal	$a = b \neq c$	$\alpha = \beta = 90^0; \gamma = 120^0$	S
Orthorhombic	$a \neq b \neq c$	$\alpha = \beta = \gamma = 90^0$	S, BC, FC, 1FC
Monoclinic	$a \neq b \neq c$	$\alpha = \gamma = 90^0; \beta \neq 90^0$	S, BC
Triclinic	$a \neq b \neq c$	$\alpha \neq \beta \neq \gamma$	S

TABLE 2.1: Bravais lattices of crystalline solids. S is for simple, BC for body-centered, F for face-centered, and 1FC for singular face-centered.

respect to the point (0,0,0), that repeats at every lattice point can create the entire system. As an example, NaCl, which looks like the BCC structure, is actually SC with a basis consisting of one Na at (0,0,0) and a Cl at (0.5,0.5,0.5).

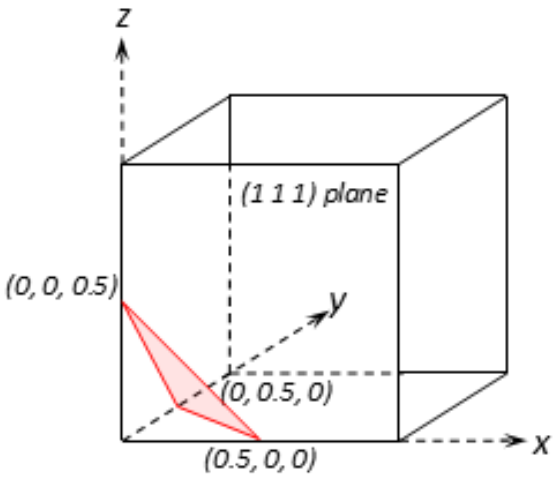

FIGURE 2.2: Schematic of an hkl plane on a generic lattice. a (1 1 1) plane is demonstrated with intercepts halfway along each of the vertexes.

These fractional conventions are used to describe positions within the unit cell or distances from the origin in a basis, but planes follow a different convention, using Miller indices. For a given plane, the a, b, and c intercepts are taken as (x,y,z), then the reciprocal is taken to produce $(\frac{1}{x}, \frac{1}{y}, \frac{1}{z})$. The lowest set of whole numbers that maintain the same ratio between them becomes the Miller indices for this plane. For example, a plane with intercepts at (0.5,0,0), (0,0.5,0), and (0,0,0.5) would have the reciprocal taken to produce

Lattice System	d_{hkl}	V
Cubic	$(\frac{h^2+k^2+l^2}{a^2})^{-1/2}$	a^3
Hexagonal	$(\frac{4}{3}\frac{h^2+hk+k^2}{a^2}+\frac{l^2}{c^2})^{-1/2}$	$\frac{\sqrt{3}}{2}a^2c$

TABLE 2.2: d_{hkl} and volume for relevant structures in terms of lattice parameters.

$(\frac{1}{0.5},\frac{1}{0.5},\frac{1}{0.5})$=(2,2,2)=(1,1,1), as shown in Figure 2.2. These Miller indices are referred to as (*hkl*), and the orientation of crystal structures are usually given in terms of the facing *hkl* plane. In the previous example given *h*,*k*,*l*=1.

The distance between equivalent, parallel planes is an important quantity in diffraction studies such as ours. The generally interplanar distance, d_{hkl}, can be calculated from the structural parameters and for given (*hkl*) is equal to

$$d_{hkl} = V(h^2b^2c^2\sin^2\alpha + k^2a^2c^2\sin\beta + l^2a^2b^2\sin^2\gamma + 2hkabc^2(\cos\alpha\cos\beta - \cos\gamma) + 2hlab^2c(\cos\alpha\cos\gamma - \cos\beta) + 2kla^2bc(\cos\beta\cos\gamma - \cos\alpha))^{-1/2} \quad (2.1)$$

Where d_{hkl} is the distance between a given *hkl* plane and V is the volume of the unit cell, which is equal to

$$V = abc\sqrt{1 - \cos^2\alpha - \cos^2\beta - \cos^2\gamma + 2\cos\alpha\cos\beta\cos\gamma} \quad (2.2)$$

Both of these equations are quite long in their general form, though for any case except triclinic they may both be greatly simplified, as shown in Table 2.2.

2.1.2 Phonons

By taking the Fourier transform of the crystal lattice, we get the reciprocal lattice, which also happens to be a Bravais lattice. One popular primitive cell in a Bravais lattice is the Wigner-Seitz cell. To construct a Wigner-Seitz cell, lines are drawn from a primitive lattice site to neighboring lattice sites. At half the length of each line, a flat, orthogonal surface is

drawn, becoming the faces or vertexes of the primitive cell. The smallest space enclosed by these surfaces becomes the Wigner-Seitz cell.

Within reciprocal space, the Wigner-Seitz primitive cell of the reciprocal lattice is referred to as the First Brillouin Zone (FBZ), with edges at $\frac{\pi}{a}\hat{i}$. For periodic boundary conditions, any combination of reciprocal lattices vectors b_i satisfying

$$k = \Sigma_i \frac{m_i}{\sqrt[3]{N}} b_i \tag{2.3}$$

gives an allowed wavevector k, where N is the number of primitive cells in the lattice. The FBZ and the allowed wavevectors therein determine a vast amount of important electronic, optical, and vibrational properties of the material. A full derivation of how and why can be found in classic solid state theory textbooks (such as the one from Kittel[1] or from Ashcroft and Mermin's[2]), as that is unfortunately beyond the boundaries for this text.

The normal modes of vibrations within a crystal structure can be described in a concise manner through the use of vibrational pseudoparticles called phonons. The vibrational frequency dependence of the normal modes on the wavevector is known as a dispersion relation $w(k)$, with periodic boundaries at the FBZ. Distinct normal modes will occupy different branches within the dispersion relation. If the energy of the mode stays finite at the Brillouin zone center, where k=0, then the mode is optical, whereas if $w(k = 0) = 0$ then the mode is acoustic. These labels refer to how adjacent ions move in real space, where adjacent ions responding to an optical phonon move in an alternating fashion, whereas ions move together in response to an acoustic phonon.

Because the wavevectors of photons (light particles) are very small (orders of magnitude smaller than the values at the FBZ edges) optical probes only access, at the first-order,

Degeneracy	Symbol	Rotational Symmetry	Subscript	Center of Symmetry	Subscript
1	A	S	1	S	g
2	E	A	2	A	u
3	F				
>0	B				

TABLE 2.3: The phonon labeling system. A given phonon is labeled with the appropriate symbol and subscripts. S is for symmetric, A for antisymmetric.

the phonon modes around the k=0 zone center. For acoustic phonons, the frequency approaches 0 for small values of k, making optical measurement of acoustic photons (referred to as Brillouin scattering) much more difficult. Meanwhile, for optical modes, the frequency is finite at k=0. In our experiments, only optical phonons are investigated. A lattice with n ions in its basis will have $3n$ normal modes. Three of these normal modes will be acoustic, leaving 3(n-1) optical modes.

Phonon modes are labeled based on their symmetries within the crystal structure and the amount to which they are degenerate. Non-degenerate phonon modes are given the label A, while doubly degenerate are labeled E, and triply are F. Phonons belonging to antisymmetric mode representations are given the label B. The symmetries are noted in the subscript. Rotational symmetry is taken into account by numbers, where the subscript 1 denotes a symmetry about a 180^o rotation about the axis perpendicular to the principal axis of symmetry, whereas 2 denotes antisymmetry about the same transformation. For center of symmetry, the mode is given the subscript "g" (gerade, German for even) if it has a center of symmetry, or the subscript "u" (ungerade, German for uneven) for a center of antisymmetry. These are listed clearly in Table 2.3. For example, a doubly degenerate phonon mode, with a center of symmetry and anti-symmetric about a 180^o rotation will be labeled as an E_{2g} mode. Generally, modes with the subscript "g" are Raman active, and those with the subscript "u" are IR-active.

2.2 Diamond Anvil Cell

The incredible pressures of interest in the present studies have been referred to, but we have as of yet to describe exactly how it is done. How awfully taunting! It will be first useful to define pressure more generally.

While pressure can often be thought of an intrinsic thermodynamic property, as the intensive conjugate force paired to the extensive displacement volume, it is much easier defined as the force exerted on an area, that is to say $P = \frac{F}{A}$. This already hints at how one might generate a massive pressure - either exert an incredible amount of force, such as the gravitational pull of the entire upper planetary material on the deep Earth, or reduce size to be microscopic. Due to more than just logistical limitations, experimentalists opt for the latter.

In the first half of the 20th century, high pressure studies were limited to 4-5 GPa, an intrinsic limitation of the piston cylinder apparatus used at the time. However, the biggest interest at that time was the synthesis of synthetic diamonds, and diamonds required more pressure than that could be generated. The pressure barrier was surpassed by Tracy Hall's "Belt" apparatus, where a liner and gasket were placed between the pistons, which acted to radially support the pistons and contain the interior chamber, applying and allowing application of higher pressure. The standard maximum pressure of this apparatus moved up to 5-10 GPa, which has more than doubled since. This type of "belt" apparatus is still in use for large scale diamond production owing to the large sample volumes that can be brought to considerably high pressures[3].

The most major leap in the design of high pressure devices was achieved thanks to Nobel physicist Percy Bridgman: his opposed anvil design busted previous barriers. This apparatus featured small, tungsten carbide anvils, aligned such that two small, flat faces (known as culets) oppose each other to compress a sample[4]. The microscopic sample volumes contained by these anvils was able to reach incredible pressures by application

of only a modest force. A superhard material such as tungsten carbide was essential to the success of the design. Hardness is simply the ability to resist deformation under pressures, as other materials casually thought of as hard such as steel deform like plastic under gigapascals of pressure. Anvils allowed to deform to a similar degree would be destined for failure. Bridgman's device was so simple in theory that it could have been designed much earlier.

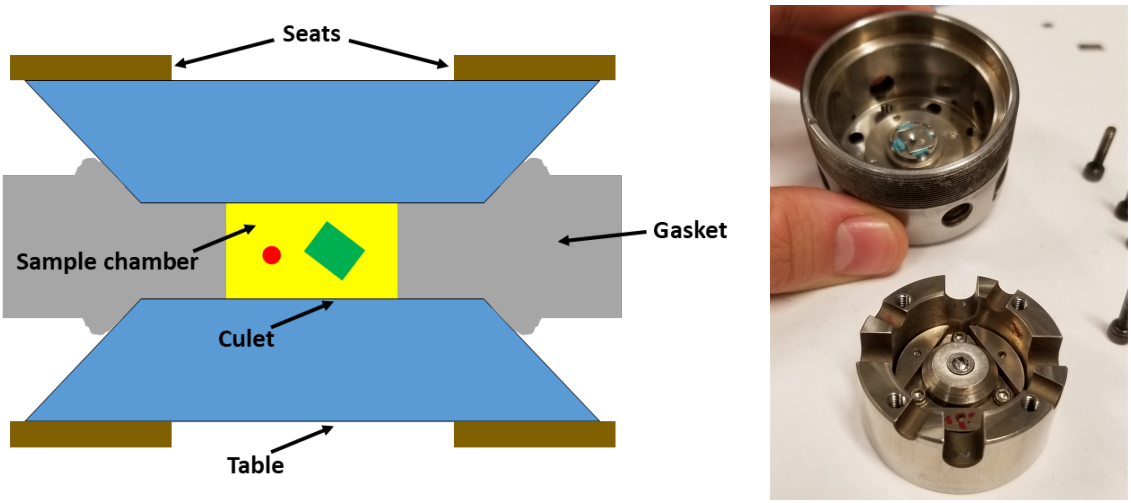

FIGURE 2.3: Schematic and picture of a diamond anvil cell. In the picture, the DAC is separated, with the piston in the foreground and body in the background. A steel gasket is secured on the anvil within the body. Thumb is for scale.

However, tungsten carbide is an opaque material making it difficult to probe material properties *in-situ*. It is not the hardest material available either. As such, diamonds were eventually chosen as the new anvil material as a destined pairing for high pressure experiments[5], being both the hardest material available, and optically transparent to an extensive spectral range, thus allowing for a wide range of studies. Consequently, in 1959 the diamond anvil cell (DAC) was born[6], allowing experimentalists to presently obtain pressures well over 400 GPa. This wasn't the end of tungsten carbide's residence in high pressure devices.

Soon after the DAC took the main stage, the major issue faced by users was the alignment stability of the opposed diamond anvils. This was resolved though implementation of tungsten carbide seats, backing the wide end, or table, of the anvils. The seats stabilized the alignment, as well as allowed for a wider diamond aperture, leading to a higher and enhanced throughput of probing radiation. The backing seats allowed for smaller diameter diamond anvils to be used as well, reducing the overall cost of the DAC[7].

Many different DAC designs have since been introduced, working off the previously stated developments[8]. For the most part, they are all arrangements of piston design, pressure application, anvil support types. A schematic of a typical DAC assembly can be seen in Figure 2.3, along with a picture of a separated DAC. The most prominent configurations are: the Merrill-Bassett cell[9], developed initially for single crystal diffraction studies, the Paris-Edinburgh-type cell[10], developed for neutron diffraction studies, the Mao-Bell cell[11], designed for high and low temperature studies, and the membrane DAC[12], designed for more continuous, controllable pressure ramps.

Much of the studies in this thesis are with a with a 3- or 4-pin piston-cylinder cells, driven by the actions of screws or a membrane. Type IIa gem quality diamond anvils were used because their low nitrogen impurity content allows a fairly unobstructed access to mid-IR spectral regions. The nitrogen impurities otherwise cause strong absorption between 1100-1500 cm^{-1}. Some X-ray diffraction experiments also using a membrane DAC with type Ia diamond anvils.

2.2.1 Gasket Preparation and Materials

It was mentioned earlier that hard steel deforms like plastic under such incredible pressures. This is actually quite fortunate, as it makes for a suitable solid gasket material. The gasket serves as both sample isolation and diamond anvil support, like the belt device that came before it.

A thin slip of metal, usually of around 250 μm thickness, is secured against the anvil on the body of the DAC, initially held in place by sticky tack. The piston anvil is pressed against this gasket from the other side, indenting the shape of both anvils into the metal. This action causes two things.

First, the region beneath the anvil culets is reduced in thickness, to anywhere of 50-150 μm, hardening the gasket and increasing the yield strength of the material. The radial support from this deformation (extrusion) is important for higher pressure experiments, while lower pressure (sub 10 GPa) experiments can make do with a larger volume/thickness. Thinner, harder gaskets mean gasket failure is less likely during the upstroke in pressure, though equally the lack of plasticity of harder materials makes the gasket more prone to rupturing for the pressure down-stroke. There's always a balancing act!

Second, material from the slip is extruded up the sides of the anvil, indented with the shape of the anvil the entire way up. This indentation forms a seal that will help to contain any material stored by the gasket, while the extent of the extrusion gives a rough estimate of the gasket thickness between the culets. This thickness is measured more accurately with a micrometer following the indentation, however. This extrusion further acts as a belt, reinforcing the diamond anvils upon load.

Once an appropriate thickness of gasket has been obtained by indentation, the piston is removed and the gasket is prepared for drilling. The gasket is aligned with a pulse-laser machining setup, featuring a frequency-doubled Nd:YAG Q-switched microchip 300 ps laser, with a repetition rate at 500 Hz and a central wavelength of 532 nm . The motorized system then maneuvers the gasket in a circular pattern of user selected radius. Along this path, the pulsed laser carves out a hole that will be used for the sample chamber. The wider this hole, the more sample that can fit within, while the less radial support from the compressed edges. Less of this support can lead to translation or expansion of the sample chamber, potentially leading to a gasket failure if the chamber reaches too close to an edge of the culet. As such, the diameter is usually kept to typically one third to one half that of

the culet. Once machining is completed, the gasket is removed from the laser machining platform, cleaned in an ultrasonic bath with soap and acetone, separately, to remove any oxides, free expulsed materials, or other exotic contaminants. The gasket is then ready for action!

The gasket materials are almost always metals. ANSI 301 full hard stainless steel or spring-steel are cheap and effective materials for use for lower pressure studies, while harder, more costly refractory metals such as rhenium or tungsten are used for higher pressure studies (above 140 GPa) and for high temperatures (above 2000 K). Apart from metals, mixtures of ultrahard cBN and epoxy have been shown to be effective as gasket materials[13]; this wasn't used in our experiments, however, due to concerns of complications imposed from a BN polytype.

2.2.2 Pressure Gauges

Following the development of the gasket for DACs, the limiting factor for high pressure research was the difficulty of sample pressure detection within a DAC. Initially, the pressure-volume equations of state of studied metals were used to gauge pressures. This method would be quite cumbersome, however, for studies involving anything that wasn't a metal with a reliably established equation of state. A more robust solution was needed.

This solution would come in the 70s through use of ruby fluorescence. The technique involved the placement of a tiny ruby (α-Al_2O_3:Cr^{3+}) sphere, the size of 10 μm or less, within the sample chamber along with the sample. By excitation of a laser (532 nm), the Cr^{3+} impurities in the ruby will emit a strong, red R_1-R_2 doublet (as described in Figure 2.4) with respective wavelengths of 694.25 and 692.86 nm at room conditions[14], the spectrum of which can be captured by a spectrograph equipped with a charge-couple device (CCD). This fluorescence can be seen quite effectively through a microscope with a

red-pass filter, where all will be dark except for a red, glowing microsphere, aiding greatly in visual optimization of the laser alignment.

The fluorescent signal of ruby showed reliable pressure dependence up to 20 GPa[15] and was soon after calibrated to 100 GPa[16]. Ruby spheres on the order of less than a micron across can be placed within the sample chamber of a DAC, taking up an tiny portion of the sample chamber while still being visible under magnification. The rubies are also chemically stable, making them suitable to be included alongside most studied materials, and is structurally stable, meaning it won't undergo a phase transition to a different, uncalibrated substance at different pressure conditions. The only potential reaction that ruby undergoes is melting when exposed to sufficient heating, which still only generally occurs when it couples with a heating laser. Furthermore, the shape of the fluorescence doublet provides information regarding the hydrostaticity of the sample chamber. Under non-hydrostatic conditions (were there is a large pressure gradient), the R_1 and R_2 lines become increasingly convoluted as both their line widths increase. The ruby fluorescence method proved to become a staple of high pressure studies.

The pressure can be calculated by the R_1 shift by use of the empirical relation

$$P(GPa) = \frac{A}{B}[(\frac{\lambda}{\lambda_0})^B - 1] \tag{2.4}$$

where P is the pressure in gigapascals, λ_0 is the wavelength of the R_1 line at ambient pressure, λ is the recorded wavelength of the R_1 at the given conditions, and A and B are constants dependent on the model assumed. For non-hydrostatic conditions, the Mao model uses A and B equal to 1904 GPa and 5, respectively[17]. For hydrostatic conditions, the Dewaele model uses A and B equal to 1920 GPa and 9.61, respectively, and is calibrated up to 180 GPa[18]. These are the two models used in the present study.

The pressure dependence of both models remain fairly similar under most pressure, remaining less than 2% in difference between the two models for pressures under and

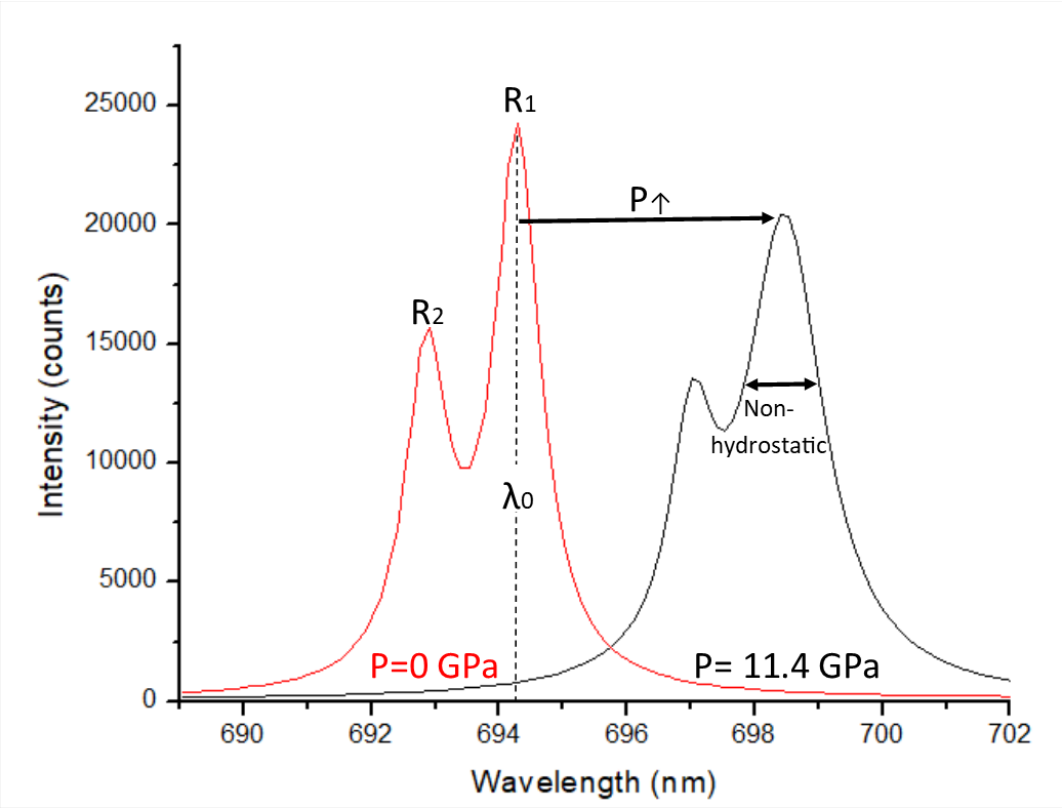

FIGURE 2.4: R_1 and R_2 fluorescence lines of ruby at different pressures in a KBr medium. The shift to a higher wavelength can be seen upon increasing pressure. Furthermore, due to the nonhydrostatic stress caused by the imperfect pressure transmission of the KBr medium, we observe broadening of the two fluorescence lines at a higher pressure.

around 10 GPa, as the pressure dependence is linear to about 20 GPa[19]. The maximal difference between them is only about 16% by the end of the calibrated range, around 180 GPa. This can all be seen in Figure 2.5.

Though the Mao/Dewaele models for non-hydrostatic/hydrostatic pressure calibration, respectively, have proven quite accurate, reliable, and effective, not to mention easy to transition between, many other similar models for the pressure dependence of the ruby R_1 line have been published[21–27]. A new model was proposed to bridge the gap between them and serve as the standard model to be used in reports[20]. This model, named Ruby2020, consists of a second order polynomial of form

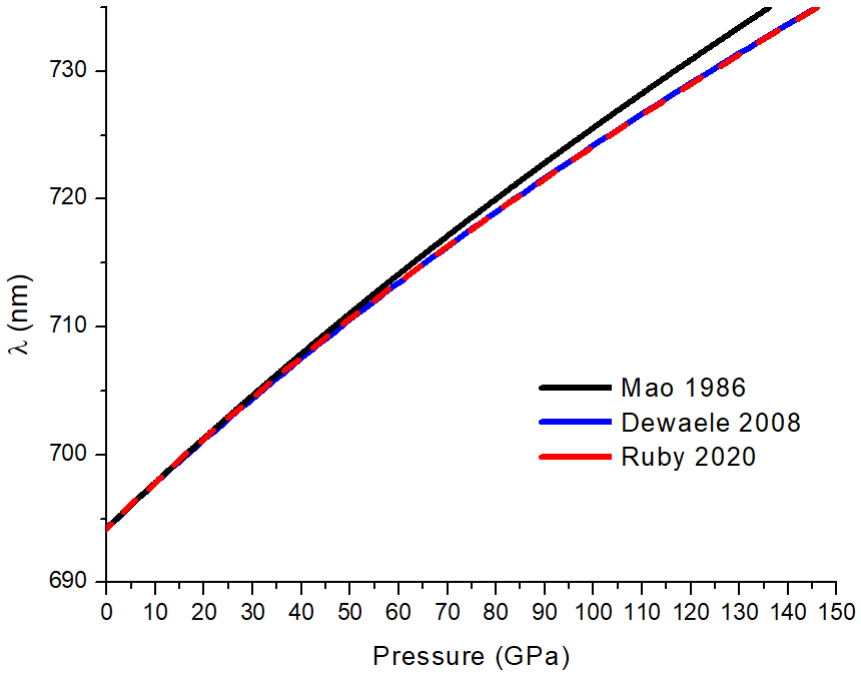

FIGURE 2.5: A comparison of thesis-relevant and recent proposed ruby calibration models. The black line represents the non-hydrostatic model by Mao *et al.*[17], whereas the others are for hydrostatic conditions. By design, the newly proposed Ruby2020 model[20] lies very close to the Dewaele *et al* model[18]. As mentioned, below 20 GPa, the relation is linear, so all three models align.

$$P = A(\frac{\Delta\lambda}{\lambda_0})[1 + B(\frac{\Delta\lambda}{\lambda_0})] \tag{2.5}$$

where $\Delta\lambda = \lambda - \lambda_0$, the pressure induced spectral shift, and A and B are fitted constants as before, 1870 ($\pm$10) GPa and 5.63 ($\pm$0.03), respectively. The model is calibrated up to 150 GPa with a pressure uncertainty of 2.5%. Within this 2.5% error lies all the other published gauge models; within 1% is Dewaele's (as well as the models of Dorogokupets and Oganov[22], and Chijioke *et al.*[21]).

The present study uses the Mao/Dewaele equations for pressure calibration.

2.2.3 Pressure Transmitting Media

In the majority of high-pressure experiments, a minimal pressure gradient is desired; conditions should be as hydrostatic as possible. Non-hydrostatic conditions lead to increased unaccounted strain on the materials in study, a large pressure gradient, and unpredictable and unreliable high pressure behavior, such as stress dependence of vibrational modes and transition boundaries and types due to stress induced deformation[28,29]. Hydrostatic pressure conditions are achieved by the use of a pressure transmitting medium (PTM). PTMs take the form of preferably non-reactive gases (commonly noble gases, though N_2 is popular when it's an unlikely reactant), fluids (such as mineral oil or methanol-ethanol-water mixtures, referred to as 'mew'), and soft solids, usually salts (such as NaCl or KBr). Fluid PTMs were not used in any of the experiments herein, so there's no need to describe how such processes are usually undertaken.

Among the most used gases are nitrogen, argon, neon, and helium, all of which provide the most hydrostatic conditions up to respective pressure limits. These gases all present low pressure deviations until above 10 GPa (helium doesn't even solidify at 300K until 12.5 GPa). Of all the gases, the pressure gradients for nitrogen increase most rapidly, where small pressure gradients are observed by 10 GPa, increasing to around 0.7 GPa of deviation by 25 GPa[30]. Meanwhile, helium provides the best hydrostatic environment, providing a 4% pressure gradient at 40 GPa.

However, gases aren't suitable for all high pressure studies. All the gases mentioned exhibit a range of fluorescence or vibrational spectra which absorb or saturate in certain ranges of interest, or scatter X-rays. Other studies, such as high temperature studies, necessitate that there be a separation between anvils and sample, as the world's best thermal conductor would wick any heat away rather than allowing the sample's temperature to rise. As such, optically transparent, solid PTMs are a good investment. The two solid PTMs used in this dissertation are the alkali halides KBr and NaCl, whose high-pressure

hydrostatic performance is described by Celeste *et al.*[31].

KBr is an essential PTM for IR studies, being transparent between 400-4,000 cm^{-1} (25,000-2,500 nm). It is only hydrostatic prior to a structural phase transition around 2.5 GPa. Despite this, KBr used as a PTM maintains quasi-hydrostatic conditions, with a consistent gradient increase of 0.25 GPa pressure deviation up to 11 GPa, at which point the deviation begins to steadily increase, still remaining less than 1 GPa deviation until close to 20 GPa[31]. NaCl was used primarily for heating experiments; with a transmission window of 625-40,000 cm^{-1} (16,000-250 nm) it is definitely suitable for IR studies as well. NaCl remains hydrostatic, however, only to 1 GPa. NaCl has no observed stuctural phase transition under pressure, and above that 1 GPa hydrostatic drop, it remains impressively quasi-hydrostatic, with deviations of 0.1-0.2 GPa consistent up to 14 GPa, after which deviation increases slowly[31].

2.2.4 Sample Details

Powered hBN was outsourced from Sigma-Aldrich. The sample presenting an average particle size of 1 um with a nominal 98% purity was used as is for our experiments. Small single crystals of hBN of suitable dimensions for high pressure experiments in the diamond anvil cell were detached and cut from larger domain single crystals (SPI Supplies). In both cases, the quality and phase purity were assessed by Raman spectroscopy and X-ray diffraction.

2.2.5 Sample Loading Process

The machined and cleaned gasket is replaced on the diamond of the DAC's body, secured once again by the sticky tack, located and oriented in the exact way it was for the initial impression so that the match with the diamond anvil is still perfect. For solid PTMs, grains are now added until just barely poking out of the sample chamber, then compressed into

a dense pellet. A polycrystalline grain or monocrystalline sliver of the sample is then added, and a ruby sphere is placed on the opposite anvil such that it won't be resting on the gasket or sample (and as such being induced to undue strain). If using a gaseous PTM, the sample and ruby are placed together within the sample chamber before being loaded into the gas loading system[32]. Another option for loading with gases is cryogenic loading. By obtaining the gases (in practice with N_2 and Ar) in a cryogenic liquid state, the fluid is essentially a condensed state of the gas. The fluid can be dropped into the sample chamber before applying the piston. This risks the sample being lost in case of an overflow, but it is a much quicker, cheaper option when it works.

With a sample now loaded in the DAC, characterization methods are required to monitor the change of physical properties under extreme conditions.

2.3 X-ray Diffraction (XRD)

X-rays are a powerful and versatile probe, which have found experimental and practical applications across all fields since their discovery in 1895 by Wilhelm Röntgen (the first Nobel laureate for the physics prize!). In fact, the many of the first Nobel prizes in physics were related to pioneering work using X-rays.

Crystalline solids act as a diffraction grating for radiation with a wavelength shorter than that of the interplanar distance. The condition for constructive interference of the diffracted rays must then satisfy Bragg's law.

As described in Figure 2.6, an incoming beam is scattered by electrons located around the atomic centers in an ordered plane at an angle θ, such that another parallel X-ray scattered of the neighboring plane travels an additional distance of $2d sin\theta$, where d is the distance between the two planes. For the two X-rays to interfere constructively with one another, as well as with other X-rays scattered off the same plane, this path difference

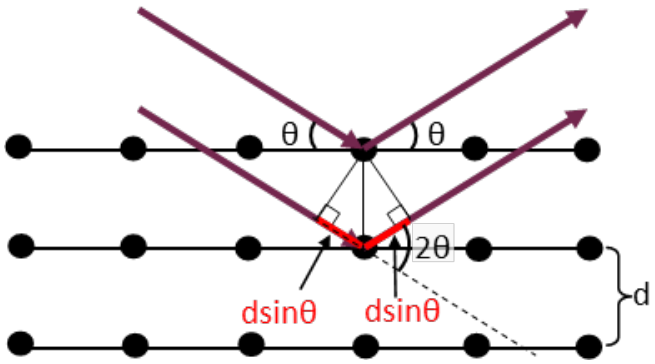

FIGURE 2.6: A representation of the Bragg scattering process, where the arrows depict the path of the X-ray beam on a crystalline solid. The red section of the beam path describes the additional distance traveled by that ray, the sum of which is obviously $2d \sin\theta$.

must be equal to an integer multiple of the X-ray wavelength, $n\lambda$. This condition for constructive interference is Bragg's law,

$$n\lambda = 2d_{hkl} \sin\theta \tag{2.6}$$

For the purposes of our experiments, $n = 1$ for all relevant cases. For each crystal grain satisfying the diffraction condition, a point of constructive interference appears at an angle θ to the scattering plane, which is 2θ to the incident X-ray beam, as shown in Figure 2.7. Where there are more grains oriented differently within the path of the X-rays, there will be more spots distributed around rings of 2θ in radius for each satisfied plane. For powder systems, where there are likely 10^{26} different orientations, these distributions of spots become a series of uniform Debye rings, each ring the result of a different hkl plane reflections, shown in Figure 2.8. For systems of lower orientational distribution, such as single crystals or semi-polycrystalline collections, a steady incident X-ray beam may satisfy the Bragg condition for few or even none of the acceptable *hkl* planes. This issue can be bypassed by modifying what parameters are available in the Bragg equation: λ and θ.

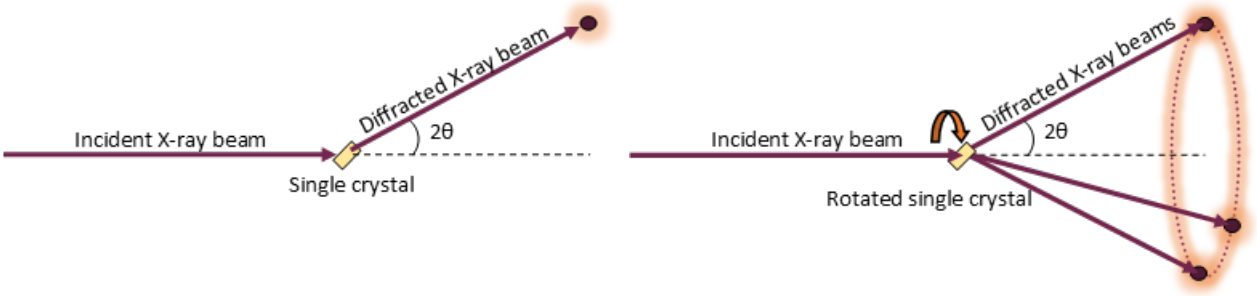

(A) Scattering resulting in a Bragg spot.

(B) Debye ring created from the rotating of a crystal.

FIGURE 2.7: An X-ray beam is aligned with a single crystal, oriented at an angle θ with a given plane such that the Bragg condition is satisfied, such as in Figure 2.7a. For a single satisfied diffraction plane on a single crystal, this leads to one intense Bragg spot, as described in Figure 2.7b. If this crystal is rotated around an axis parallel to the incident X-ray, a Debye ring is traced out instead.

Scattering by an electron is described by the Thompson equation

$$I = I_0(\frac{\mu_0}{4\pi})^2(\frac{e^4}{m_e^2 r^2})\sin^2\alpha \tag{2.7}$$

where I_0 is the intensity of the incident beam, μ_0 the permeability of free space, e the charge of the electron, m_e the mass of the electron, r the distance between electron and position of measured intensity, and α the angle between direction of scattering and the direction of the electron acceleration that gives rise to the scattering.

While the actual scattering intensity depends on many factors, the scattering amplitude of a given plane is reliant on two terms: the structure factor, and the atomic form factor.

Atomic form factor is the ratio of wave scattering amplitude by one atom by that of one electron. As the scattering power of an electron is about 7 orders of magnitude higher than that of a proton, this factor entirely depends on the number and distribution of electrons in space for one atom.

$$f_j(\mathbf{K}) = -\frac{1}{e}\int d\mathbf{r}\, e^{i\mathbf{K}\cdot\mathbf{r}}\,\rho_j(\mathbf{r}) \tag{2.8}$$

where **K** is the reciprocal lattice vector. The scattering then depends upon the atomic form factor for the atomic species, as well as their arrangement about a lattice. The scattering caused by the distribution of these factors within the lattice defines the structure factor

$$F_{hkl} = \Sigma_{j=1}^{n} f_j \, e^{2\pi i(hx_{1j}+kx_{2j}+lx_{3j})} \tag{2.9}$$

the square of which happens to be proportional to the diffraction intensity for a given *hkl* plane. With the atomic positions of each atom *j* in the unit cell known, the relative intensities of scattering can be calculated for a given *hkl* plane, as scattering is proportional to the square of F_{hkl}.

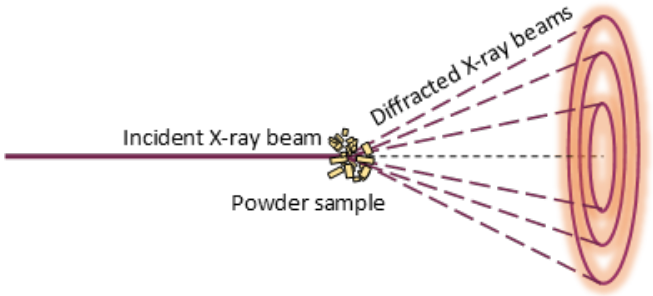

FIGURE 2.8: When a powder sample is introduced to the X-ray beam path, there is on the order of 10^{26} crystal domains, all randomly oriented. The many different orientations satisfy the rotational to produce Debye rings as described by 2.7b. Meanwhile, the Bragg condition is also being satisfied for different diffraction planes, leading to a series of Debye rings.

2.3.1 Synchrotron XRD

Despite great advances in X-ray technologies, there are still several limiting factors for in-house X-ray diffractometers for high pressure studies. For this reason, most *in-situ* high pressure XRD studies are usually done using X-rays from a synchrotron source.

Synchrotron sources are a type of electron storage ring that is optimized for access to the radiation emitted by the accelerated particles. When a charged particle is accelerated

near the speed of light around a circular path, intense, broadband light is emitted tangential to the direction of propagation. The radiation from relativistic electrons also tends to be highly confined in the forward direction, meaning that the divergence of a beam will be quite low, allowing for a small beam width. The broadband radiation from synchrotron sources is thus highly tunable with the use of monochromators.

The tunability is especially important because for the lower energy limit imposed on leads to a higher absorption in diamonds (1.5 mm of diamond will absorb about 99% of <0.8 keV X-ray photons[33], while our anvils have a thickness of about 2mm on average), and because the scattering angles that can be collected are limited by the detector size and by the body and gasket of the DAC. Access to higher energy photons at a synchrotron source leads to a near complete transparency of the diamonds and lower scattering angles. Typically photons of energies higher than 25 keV (<0.5Å) are desired. The width of the incident X-ray beam should also be less than the sample cavity, which is often less than $100\mu m$ in diameter. An X-ray beam width much smaller than that diameter is needed to probe specific locations within the DAC, and especially to rock the DAC at that position. Even for an infinitessimal beam width placed in the dead center of the cell, the average DAC body limits rocking to about 30^o. The need for higher incident photon flux is reinforced by the nature of our samples, which tend to be on the order of nanolitres in volume, meaning there's less for the X-rays to interact with. Furthermore, because the diffraction intensity is proportional to the square of Z, our case of low Z materials is going to be scattering that much less, especially in comparison to the high Z gasket material that will be caught in the tails of a wide beam.

Synchrotron XRD experiments in this report were undertaken at the Canadian Light Source (CLS) in Saskatoon, Canada, the Advanced Photon Source (APS), in Chicago, USA, and the Super Photon Ring 8 (SPring-8) in Sayo, Japan. Professor Serge Desgreniers was responsible for the data collection from the SPring-8 facility. The setup of the experimental hutches for the two beamlines the author visited are detailed below. Details about the BL

10XU beamline at SPring-8 are given by Hirao *et al.*[34].

Canadian Light Source (CLS)

The Hard X-ray MicroAnalysis (HXMA, 06ID-1) X-ray radiation comes from a 63 pole superconducting wiggler. The radiation is produced on an energy range from 5-40 keV with a flux of 10^{12} photons per second for 0.1% of the beamwidth when the energy is at 12keV and the storage ring is operating with 100mA electrons. The energy is selected using a double crystal monochromator housing two crystal pairs of Si(111) and Si(220). The beam then passes through a collimator and a rhenium clean-up aperture before reaching the DAC and sample. This produces a close to circular beam with a radius of about 30 μm. The diffracted X-rays are collected with a MAR345 imaging plate detector (MarXperts, GmbH), located several tens of centimeters away, producing an X-ray diffraction image, circular with a diameter of 345 nm and with a pixel resolution of $100\mu m$ x $100\mu m$. The alignment of the collimator, aperture, and DAC, and the rocking procedures are done in accordance with the protocols described by Smith and Desgreniers[35].

Some XRD data were also collected at the newly opened CLS Brockhouse X-ray Diffraction and Scattering (BXDS) facility, but no pressure ramps were performed and were merely meant to corroborate other measurements.

Advanced Photon Source (APS)

X-ray diffraction studies at the APS were done at the High Pressure Collaborative Access Team (HPCAT) beamline 16ID-B. The undulator-based X-ray beam ranges in energy from 18-50 keV, as selected by the double crystal (Si(111) and Si(220)) monochromator. The beam is focused by a pair of Kirkpatrick-Baez (KB) mirrors to produce a focused beamsize of 3x6μm^2 with a flux of 10^{12} photons per second at 30keV . The beam is passed through a clean-up aperture prior to reaching the sample. Diffracted X-rays are collected on a fast

readout Pilatus 1M detector[36,37]. The setup for sample heating using focused laser beams is described in Chapter 5.

2.4 Vibrational Spectroscopy

Vibrational excitations can be treated similarly, though independently, to electronic excitation in many circumstances. Just like for an electronic state, probing a vibrational state can cause an excitation or decay between ground and excited vibrational states. This can be used to study the phonon modes of a material. Raman and IR are the most common techniques used for studying optical modes near the center of the FBZ, providing similar but complimentary information. Though the physical processes are quite different, the vibrational information reveals similar information about a material depending on their selection rules, so they are often times considered as complimentary.

A vibration is essentially a series of deformations transmitted through a solid. The effect this deformation has on the material determines whether the related phonon can be detected by either spectroscopic method. If these deformations lead to a change in the polarizability, as in Figure 2.9a, the mode is Raman-active, whereas if the dipole moment is altered, as in Figure 2.9c, the phonon will be IR-active. Depending on the symmetries of the unit, be it molecular or crystalline, a given phonon mode can be active to either technique, to both, or to neither. Because of this, Raman and IR spectroscopies can be used together to reveal information neglected by the other's selection rules, and corroborate those that are shared.

Vibrational spectroscopy has become a hallmark within high pressure research for many reasons. Primarily, because diamond is transparent to a large optical range, these spectroscopic methods have direct access to microscopic samples in the DAC. Diamonds with a naturally occurring high nitrogen content do absorb a broad portion of the mid-IR spectrum, but low nitrogen content diamonds are available and just as effective of anvils,

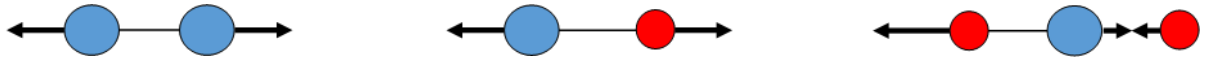

(A) Raman-active, IR-inactive. (B) Raman- and IR-active. (C) IR-active, Raman-inactive.

FIGURE 2.9: Schematic of molecular vibrations satisfying different selection rules. Differently colours circles represent different atomic species.

although being more expensive. These spectroscopic methods are very useful at material identification and characterization, giving an effective report of what is and isn't in the DAC and confidently signaling phase transitions. Unlike XRD, the signals for such spectroscopic techniques do not have the type of Z-dependence that makes studying low-Z materials a challenge.

2.4.1 Raman Spectroscopy

Raman Spectroscopy is a commonly used technique for high pressure experiments for several reasons. As it is very sensitive to minor changes in atomic bonding and crystal structure, it proves a powerful technique for studying solid-solid transitions and metastability phenomena. Raman Spectroscopy has been used to map out the pressure-temperature phase diagrams of materials, probe bonding behaviour under unusual thermodynamic conditions, and study both intra- and inter-molecular bonding characteristics of materials in a diamond anvil cell. Diamond, as well as cBN, have also been employed as Raman pressure gauges due to their structural and chemical stability under HPHT conditions[38]. Furthermore, many Raman setups double as a ruby fluorescence system, reducing the need for multiple realignments within a single experiment.

Raman Scattering

Raman spectroscopy employs a monochromatic source of light with whose the change of frequency due to Raman scattering of a sample is inspected. When a sample is subjected to electromagnetic radiation, scattering of the radiation can occur. Generally, the scattering

type observed is Rayleigh scattering, an elastic process leading to no change in frequency of the scattered photon. However, less frequently (about 10^{-6} times as often), Raman scattering can occur when a phonon is scattered in the process. To explain this process, Stokes scattering must first be discussed.

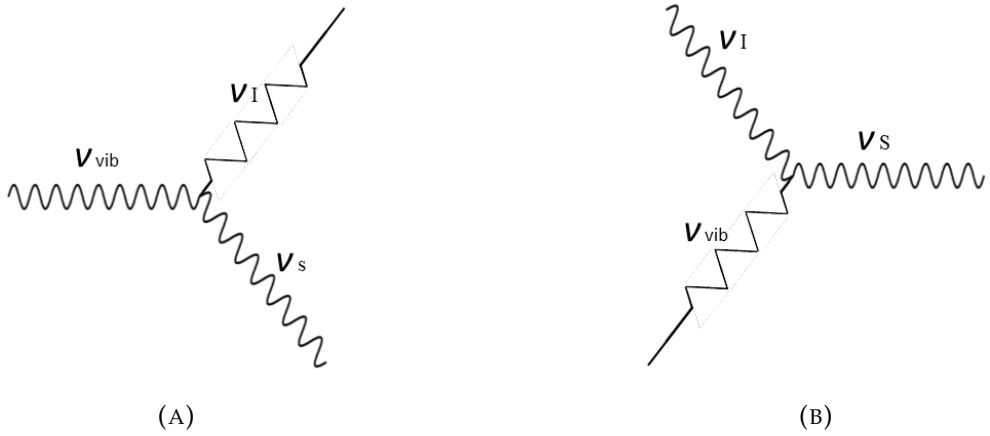

FIGURE 2.10: Raman scattering diagrams of an incident photon of frequency ν_I interacting with a vibration of frequency ν_{vib} through the emission of a phonon (Stokes scattering, **a**) and absorption of a phonon (Anti-Stokes scattering, **b**).

When a system such as a molecule in a vibrational ground state absorbs an incident photon of energy $h\nu_I$, it is excited to a virtual state. The system immediately emits a scattered photon of energy $h\nu_s < h\nu_I$ and transitions down to a vibrational excited state in what is referred to as Stokes scattering. This process can be equally described by the emission of a phonon, as shown in Figure 2.10a. To preserve the conservation of energy, the energy of this scattered photon must be

$$h\nu_s = h\nu_I \pm h\nu_{vib} \tag{2.10}$$

where ν_{vib} is the frequency of the vibration, referred to as the Raman shift within the frame of Raman spectroscopy, often measured in cm^{-1}, and the $\pm$ is negative for the Stokes scattering process. This difference in energy goes into exciting the system into a vibrational excited state.

However, the opposite process can also occur, as in Figure 2.10b. If the initial state is a vibrational excited state, then the system may go back to a lower state after absorbing and emitting a photon. In this case, $h\nu_s > h\nu_I$, meaning that the vibrational energy has been converted to radiant energy. This process is known as Anti-Stokes scattering, and can also be described by equation 2.10, with the $\pm$ sign becoming positive.

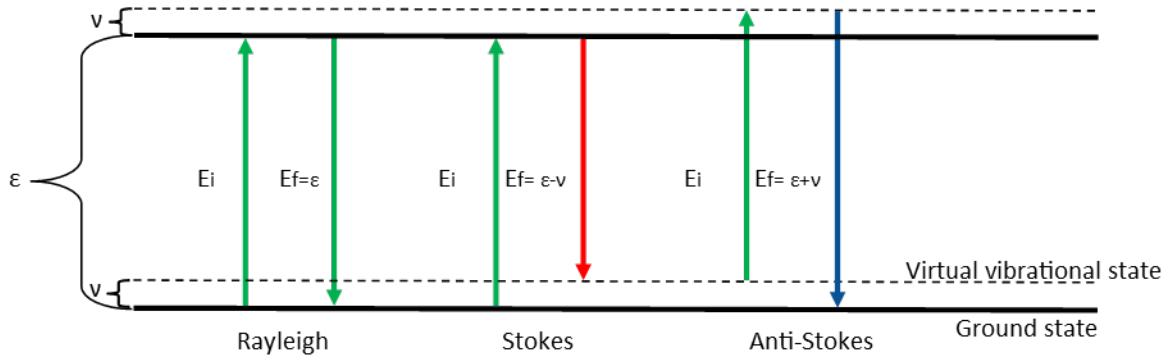

FIGURE 2.11: Elastic (Rayleigh) and quasi-elastic (Raman) scattering processes.

Rayleigh and Raman scattering describes all three scattering processes discussed above and presented in Figure 2.11. The difference in frequency is independent of the incident wavelength, and as such any wavelength of laser light could theoretically produce Raman scattering.

In a typical Raman spectrum, the Rayleigh line is centered at a Raman shift of 0 cm^{-1}, measured relative to the wavenumber (inverse of wavelength expressed in units of cm^{-1}) of the corresponding excitation light, with Stokes and Anti-Stokes lines separated in a symmetric fashion around the Rayleigh line. At thermal equilibrium, the population of the ground state is higher than that of the excited state, in line with Maxwell-Boltzmann distribution law. Because this leads to a much higher probability for Stokes scattering, it is customary only to take the Stokes side of the spectrum[39]. This custom is followed in these experiments, as will be described in section 2.4.1.

The Raman shift of peaks on a Raman spectrum then give a measurement of the frequency of Raman-active phonons in the studied system. In molecular solids, vibrations

due to intramolecular interactions appear in the 400-4000 cm^{-1} range (the same energy range as mid-infrared radiation), while vibrations arising from intermolecular interactions such as lattice vibrations appear in the 0-400 cm^{-1} range (far-IR energy). Furthermore, as the integrated intensity of a Raman line is proportional to concentration and degree of polarizability, Raman spectroscopy can be used for quantitative analysis. Because of the quantitative, chemical information that Raman spectroscopy is capable of providing, it is also widely used for chemical standards analysis.

The vibrational frequency of a diatomic molecule is given by

$$\nu = \frac{1}{2\pi c}\sqrt{\frac{K}{\mu}} \tag{2.11}$$

Where K is the force constant and μ is the reduced mass, which shows that ν is proportional to $\sqrt{K}$. As materials become more dense in response to elevated pressures, the bonds typically become stiffer, leading to an increase in the Raman shift. This makes Raman spectroscopy quite effective at detecting the response of a material to pressure, and any related deformations caused. Any drastic changes in the spectrum, such as the appearance or disappearance of Raman lines, indicates a change in molecular symmetry or the creation or destruction of bonds in the molecule, respectively. Such indicated phase transitions can be corroborated with results from other techniques, like XRD, for a full picture of the induced changes.

Experimental Setup

Raman spectroscopy experiments were performed at the Laboratoire de Physique de Solides Denses (LPSD) at the University of Ottawa. The setup included a solid state frequency doubled Nd:YAG laser (532.18 nm) run at 200 mW at the source, though neutral optical density filters were often employed to keep the power incident on the sample down. The laser was focused with a custom-built Raman microscope using a 50X Mitutoyo objective

with a long working distance. The 180^o backscattering geometry meant that the scattered light was collected and refocused by the same objective. The focused light was passed in the microscope through a laser line rejection filter, steered using highly reflective mirrors, and focused into a multimode optical fiber. The fiber carried the light to an Andor Shamrock SR-303i spectrometer. The aperture and grating could be changed based on desired needs, but these studies consistently used a 1800 line/mm grating with a 100 μm slit opening. This combination yielded a spectral resolution of 0.05 nm (1.5 cm^{-1}) at 575 nm (17400 cm^{-1}). The dispersed light was detected by a thermoelectrically cooled (-70^{o}C) Andor Newton charged-coupled device (CCD). The resulting Raman spectrum was acquired using Andor Solis software. A neon lamp was used for spectral calibration, with a third-order polynomial fit of the known Ne emission lines to those collected, within 1 cm^{-1}.

The DAC was mounted in a holder attached to xyz translation stages with the piston facing the microscope. Manual adjustments were made on a micrometer scale using the stage for alignment with the laser. Positioning was done using the CCD video camera, the speckle pattern of throughput light, and optical microscope that could be flipped in with the use of a beamsplitter. Raman line profiles were analyzed with XRDA[40] using either a Gaussian or Lorentzian fitting function to extract peak positions, line widths, and integrated intensities.

2.4.2 Infrared Spectroscopy

Unlike Raman Spectroscopy, IR spectroscopy relies on absorption or reflection rather than scattering. Infrared absorption occurs when the energy of an incident photon is equal to that of a phonon in a molecule or crystal. If the vibration causes changes in the electric dipole moment, then the incident light is able to couple with the vibration and be absorbed.

For IR studies, it is vital to take into account the thickness of the sample. Too thin, and the sample won't absorb effectively. Too thick, and the IR light is completely absorbed such that peak profiles are no longer discernible. Certain samples can be compressed to an appropriate thickness, but not always. This issue is even more essential for powdered samples, which also scatter the probing beam, meaning that it is possible to have a powdered sample that is too thin to absorb effectively, while too plentiful, scattering the probe into saturation. For reflectivity measurements, the sample surface being probed should be flat and parallel to the culet. For these reasons, thin single crystals were preferred for our experiments.

Further complications can arise from defects within the diamond anvils themselves. IR absorbing nitrogen impurities occur naturally within diamond, which vastly obscures the mid- to far-IR regions of the spectra. As such, type II low nitrogen content diamonds, preferably synthetic, are used as the anvils for IR studies to maintain access to these regions of the spectrum, as noted before.

Fourier Transform Infrared (FTIR) Spectroscopy

Previous generations of IR spectrometers have employed prisms for optical splitting or gratings as monochromators. These first generations of IR spectrometers possessed low scan speed, sensitivity, and poor resolution. The introduction of the interferometer, however, brought about the third generation of IR spectrometers, the FTIR, which improved upon the faults of the previous methods in one powerful instrument.

In most cases, a Michelson interferometer is employed, a beamsplitter separates the light, with half going towards a fixed mirror and the other half towards a moveable mirror, before recombining and being directed to the detector by the same beamsplitter, as shown in Figure 2.12. As the moving mirror scans, the resulting signal is an interferogram. This signal will be an interference pattern in the time domain, with maxima wherever the optical path difference, imposed by the mirror's displacement, is an integer multiple of

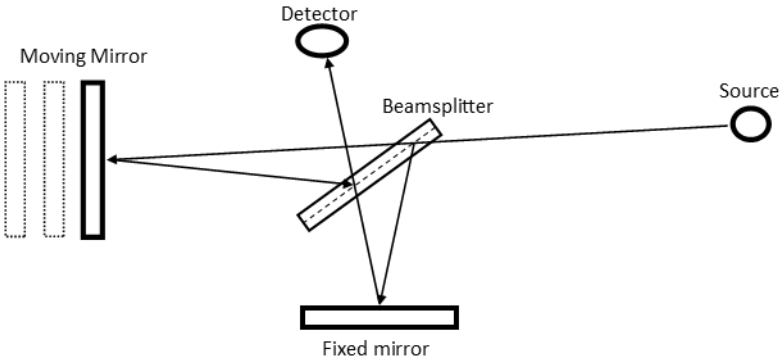

FIGURE 2.12: Basic schematic of a Michelson interferometer.

the wavelength of the probe, and minimas wherever that path difference is half multiples of the wavelength. The mirror speed, which should be constant, is monitored by a HeNe (632.8nm) passed through the interferometer to generate a reference interferogram. This reference interferogram will be a cosine wave with a frequency that is set for the desired mirror speed. In our experiments, a scan speed of 25 KHz (0.7 cm/sec) was preferred.

While traditional spectroscopic techniques allow direct measurement of a transmission or reflectance spectrum, there are a few more steps in FTIR (which is fine considering the collection rate, and resolution, are improved by a factor of 10,000 faster). As the interferogram is a measurement of the signal in the time domain, a fast Fourier transform (FFT) is applied to get the spectrum in the frequency domain.

To produce a normalized absorption or reflection signal, a reference signal must be taken. In most experiments, the absorption reference would be a signal taken through the air or through a blank substrate. In HP experiments, this reference signal is through an empty DAC. For a reflectance measurements, a reflective surface positioned perpendicular to the probe can generate a proper reference signal, while in a DAC a signal taken on the gasket may suffice.

An absorbance signal is measured such that

$$A(\nu) = \log(\frac{1}{T(\nu)}) = \log(\frac{I_0(\nu)}{I(\nu)}) \tag{2.12}$$

Where $A(\nu)$ is the absorbance, $T(\nu)$ is the transmittance, $I_0(\nu)$ is the reference signal and $I(\nu)$ is the sample signal.

With the speed of scanning in an FTIR spectrometer, multiple scans can be averaged to improve the signal-to-noise ratio (S/N) of the averaged spectrum, which is proportional to the square-root of the number of scans averaged. Our experiments took anywhere from 128-512 scans to ensure an optimal S/N.

The detector used in these experiments was a liquid N_2-cooled mercury cadmium telluride (MCT) detector using a thermal Globar IR source. A similar system was used at the CLS Mid-IR 01B1-1 beamline using synchrotron radiation as the IR source for an improved signal.

This combination allowed for a resolution of 4 cm^{-1} at 4000 cm^{-1}. The Agilent Resolutions Pro software was used to monitor, collect, and process the spectra.

Interference Filtering Methods

To achieve high pressures in a DAC, the culets of the diamond anvils are aligned such that they are parallel to each other and perpendicular to the probe, light can be reflected back and forth between the two culets several times, producing a Fabry-Perot effect. This results in a periodic pattern superimposed to the IR spectrum. Because this effect is an artifact, causing a reduction in the S/N in many cases, and generally being non-aesthetic, it would preferably be removed from any spectra. A substantial part of the project went into resolving this issue

Attempts to remove this in post-processing proved not only time consuming - requiring more than an hour to post-process an average spectrum - but also less than optimal. Simulating the curve with a simple periodic function proved to be an unsatisfactory fit for the entire spectrum because the frequency of the Fabry-Perot interference depends on the frequency of the signal, the spacing of the diamonds, and the ratio of sample to PTM that the signal passes through; all these parameters change over the course of a compression

cycle or even across the spectrum. Performing a FFT to eliminate the artifact in the time domain, followed by an inverse FFT back to the frequency domain works in theory, but proves equally inefficient as time and information is lost from the system considering this poses 3 transforms from the original signal. After spending much time trying to come up with the best way to eliminate this interference, the answer ended up being the most obvious: cut it out at the source.

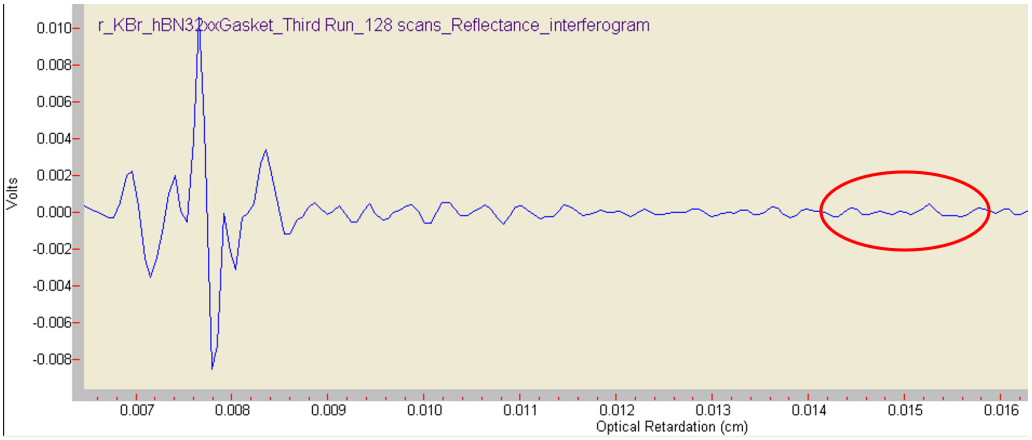

(A) Interferogram of an KBr filled DAC. The interference causing artifact is circled in red.

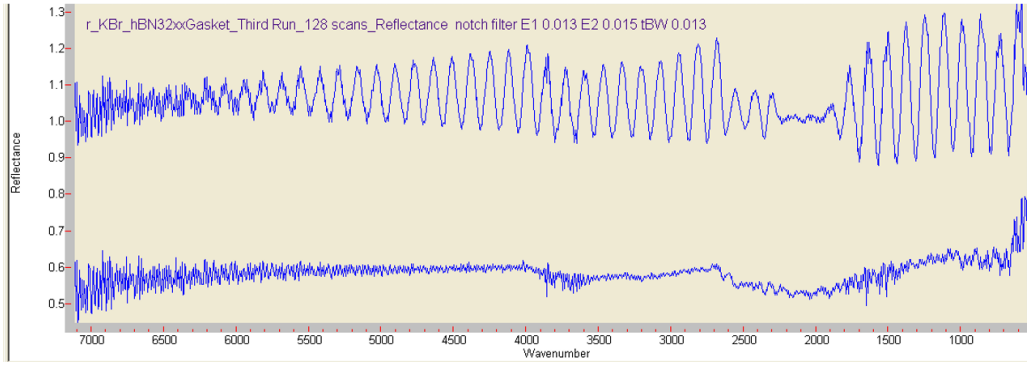

(B) The transformed spectra from the interferogram, with the unfiltered spectra given a y-offset for clarity.

FIGURE 2.13: Comparison of the filtering on a transparent medium in a DAC. The filtering of the artifact circled on the interferogram shown in Figure 2.13a effectively removes the interference seen in the transformed spectrum shown in Figure 2.13b. The filtered spectrum in Figure 2.13b is essentially flat, save for noise and some signal around 2000 cm^{-1} from diamond, and 1500 cm^{-1} and 3700 cm^{-1} from water and overtones of water, respectively, that didn't perfectly match that observed in the reference.

The Agilent Resolutions Pro software possesses time-domain filtering capabilities, and

because that is where the initial data is stored, this filtering can be done directly on the time-domain signal rather than having to perform 2 additional transforms to get the final filtered result. A notch filter can then be applied to the region where the artifact lies on the interferogram. As shown in Figure 2.13a, the artifact is not obvious at all at first glance, so the frequency of the artifact in the frequency or the parameters for a preceding fit must be taken note to know where to look for it. The parameters of the notch filter can be adjusted to produce the smoothest result. At times, a secondary notch filter needs to be applied to produce the best filtering result, likely due to the presence of an additional reflective surface, such as that from the sample. The resulting spectrum should end up without the presence of fringes, as shown in Figure 2.13b.

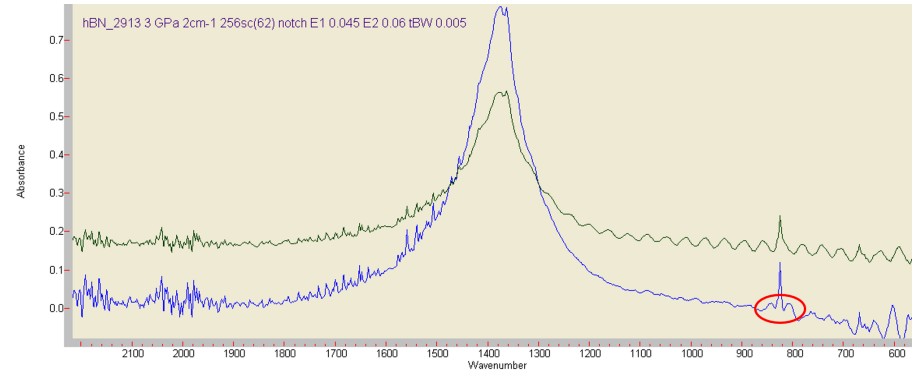

(A) hBN.

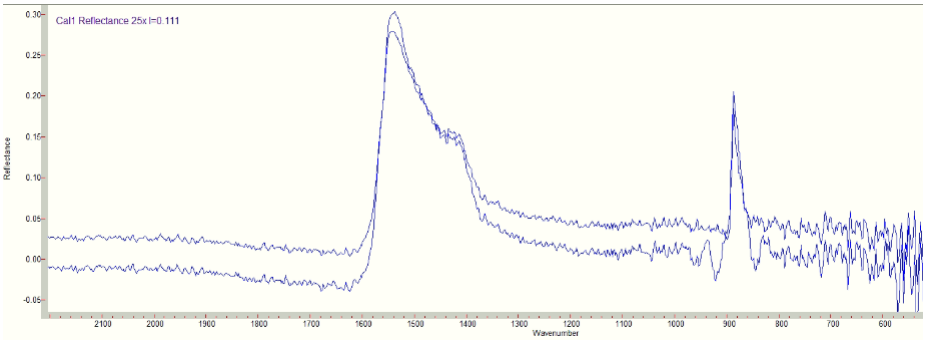

(B) Calcite.

FIGURE 2.14: Comparison of filtered and unfiltered IR spectra. Figure 2.14a shows the spectra of a sample of hBN in a DAC with a KBr PTM. The overlaid unfiltered spectra is shown in green with a y-offset for clarity. The Fabry-Perot effect appears as a quasi-periodic modulation. The notch filtering is clearly observed to remove the periodic artifacts, producing the blue spectrum. Figure 2.14b shows the spectra of a calcite crystal in air with the same notch filter applied, and the unfiltered spectra with a y-offset for clarity.

The notch filter isn't without its faults however. Following the filtering process, new, localized artifacts were observed around sharp features of the spectrum, resulting from a "ringing" affect sometimes seen when Fourier transforms are used to create sharp features. This can be seen in Figure 2.14a, where the filtering of this interference creates shoulder-like sidelobes of a sharp feature around 825 cm^{-1}. To ensure the filtering process wasn't causing any other non-genuine disruptions to the structure, the same process should be applied to a material with a well studied and similar IR spectrum. Calcite proved to be such a material with immediate access.

The filtered and unfiltered IR spectra of a single crystal of calcite is shown in Figure 2.14b. Like hBN, it also has a large, intense, broad feature above 1200 cm^{-1} and a sharp feature below 900 cm^{-1}. Applying the same filter as for hBN can be seen to produce very little difference in the spectrum apart from two side-lobes that appear around the sharp feature, much like for the case of hBN. The area of these features can be reduced by either increasing the width of the transition bandwidth of the filter, similar to the FWHM of a curve, or by increasing the width of the supergaussian stopped edges. Either of these "fixes" for the aptly named "shrugs" often leads to more interference, at half the frequency of the originally filtered interference, and may even cause distortions to the genuine spectral features. So the process of filtering can sometimes be a tug-of-war, between minimizing the "shrugs", and eliminating all interference and spectral distortions. In these experiments, the shrugs were tolerated because they are easy to identify as artifacts and remove. At times if these shrugs lead to any issues with the related peaks, a filter producing less shrug and more secondary interference can be chosen, with subsequent filters applied at half the central position of the previous until a satisfactory spectrum is achieved.

With the methods and techniques laid out here, samples of hBN were studied with a range of experimental conditions to elucidate how and why its properties change in response to pressure. The coming chapters are separated based on the techniques employed to study hBN under pressure, starting with a discussion on XRD experiments at

room pressure, then vibrational spectroscopic studies, followed by XRD experiments performed with laser heating. The final chapter discusses a side-project and employs the use of a combination of techniques.

Bibliography

1. Kittel, C. & McEuen, P. *Introduction to Solid State Physics* ISBN: 978-81-265-3518-7 (John Wiley & Sons, 2015).

2. Ashcroft, N. & Mermin, N. *Solid State Physics* ISBN: 978-0-03-083993-1 (Thomson Learning, Inc, New York, 1976).

3. Klotz, S. in *High-Pressure Physics* 1–22 (CRC Press, 2012).

4. Bridgman, P. W. The Resistance of 72 Elements, Alloys and Compounds to 100,000 Kg/Cm^2. *Proc. Am. Acad. Arts Sci.* **81,** 165–251. ISSN: 0199-9818 (1952).

5. Weir, C., E.P. Lippincott, E., VanValkenburg, A. & Bunting, E. Infrared Studies in the 1 - 15 Micron Region to 30,000 Atmospheres. *Publ. Natl. Bur. Stand. July 1 1957 June 30 1960* **63A,** 55 (1960).

6. Jamieson, J. C., Lawson, A. W. & Nachtrieb, N. D. New Device for Obtaining X-Ray Diffraction Patterns from Substances Exposed to High Pressure. *Review of Scientific Instruments* **30,** 1016–1019. ISSN: 0034-6748 (Nov. 1959).

7. Boehler, R. & Hantsetters, K. D. New Anvil Designs in Diamond-Cells. *High Press. Res.* **24,** 391–396. ISSN: 0895-7959 (Sept. 2004).

8. Jayaraman, A. Diamond Anvil Cell and High-Pressure Physical Investigations. *Rev. Mod. Phys.* **55,** 65–108 (Jan. 1983).

9. Merrill, L. & Bassett, W. A. Miniature Diamond Anvil Pressure Cell for Single Crystal X-ray Diffraction Studies. *Review of Scientific Instruments* **45.** First use of the Merill-Bassett type cell, 290–294. ISSN: 0034-6748 (Feb. 1974).

10. Besson, J. M. *et al.* Neutron Powder Diffraction above 10 GPa. *Physica B: Condensed Matter* **180–181,** 907–910. ISSN: 0921-4526 (June 1992).

11. Mao, H. K. & Bell, P. M. Design of a Diamond-Windowed, High- Pressure Cell for Hydrostatic Pressure in the Range 1 Bar to 0.5 Mbar. *Carnegie Inst Wash. Yearb.* **74. 402-405** (1975).

12. Letoullec, R., Pinceaux, J. P. & Loubeyre, P. The Membrane Diamond Anvil Cell: A New Device for Generating Continuous Pressure and Temperature Variations. *High Press. Res.* **1,** 77–90. ISSN: 0895-7959 (Oct. 1988).

13. Funamori, N. & Sato, T. A Cubic Boron Nitride Gasket for Diamond-Anvil Experiments. *Review of Scientific Instruments* **79,** 053903. ISSN: 0034-6748 (May 2008).

14. Syassen, K. Ruby under Pressure. *High Press. Res.* **28,** 75–126. ISSN: 0895-7959 (June 2008).

15. Piermarini, G. J., Block, S., Barnett, J. D. & Forman, R. A. Calibration of the Pressure Dependence of the R1 Ruby Fluorescence Line to 195 Kbar. *Journal of Applied Physics* **46,** 2774–2780. ISSN: 0021-8979 (June 1975).

16. Mao, H. K., Bell, P. M., Shaner, J. W. & Steinberg, D. J. Specific Volume Measurements of Cu, Mo, Pd, and Ag and Calibration of the Ruby R1 Fluorescence Pressure Gauge from 0.06 to 1 Mbar. *Journal of Applied Physics* **49.** Hydrostatic pressures, up to 100 GPa, 3276–3283. ISSN: 0021-8979 (June 1978).

17. Mao, H. K., Xu, J. & Bell, P. M. Calibration of the Ruby Pressure Gauge to 800 Kbar under Quasi-Hydrostatic Conditions. *J. Geophys. Res. Solid Earth* **91.** quasi-hydrostatic pressures, up to 80 GPa, 4673–4676. ISSN: 2156-2202 (1986).

18. Dewaele, A., Torrent, M., Loubeyre, P. & Mezouar, M. Compression Curves of Transition Metals in the Mbar Range: Experiments and Projector Augmented-Wave Calculations. *Phys. Rev. B* **78,** 104102 (Sept. 2008).

19. Katrusiak, A. High-Pressure Crystallography. *Acta Cryst A* **64,** 135–148. ISSN: 0108-7673 (Jan. 2008).

20. Shen, G. *et al.* Toward an International Practical Pressure Scale: A Proposal for an IPPS Ruby Gauge (IPPS-Ruby2020). *High Press. Res.* **40,** 299–314. ISSN: 0895-7959 (July 2020).

21. Chijioke, A. D., Nellis, W. J. & Silvera, I. F. High-Pressure Equations of State of Al, Cu, Ta, and W. *Journal of Applied Physics* **98,** 073526. ISSN: 0021-8979 (Oct. 2005).

22. Dorogokupets, P. I. & Oganov, A. R. Ruby, Metals, and MgO as Alternative Pressure Scales: A Semiempirical Description of Shock-Wave, Ultrasonic, X-Ray, and Thermochemical Data at High Temperatures and Pressures. *Phys. Rev. B* **75,** 024115 (Jan. 2007).

23. Holzapfel, W. B. Progress in the Realization of a Practical Pressure Scale for the Range 1–300 GPa. *null* **25,** 87–99. ISSN: 0895-7959 (June 2005).

24. Jacobsen, S. D. *et al.* Compression of Single-Crystal Magnesium Oxide to 118 GPa and a Ruby Pressure Gauge for Helium Pressure Media. *American Mineralogist* **93,** 1823–1828. ISSN: 0003-004X (Nov. 2008).

25. Kunc, K., Loa, I. & Syassen, K. Diamond under Pressure: Ab-Initio Calculations of the Equation of State and Optical Phonon Frequency Revisited. *null* **24,** 101–110. ISSN: 0895-7959 (Jan. 2004).

26. Sokolova, T. S., Dorogokupets, P. I. & Litasov, K. D. Self-Consistent Pressure Scales Based on the Equations of State for Ruby, Diamond, MgO, B2–NaCl, as Well as Au, Pt, and Other Metals to 4 Mbar and 3000 K. *Russian Geology and Geophysics* **54,** 181–199. ISSN: 1068-7971 (Feb. 2013).

27. Syassen, K. Ruby under Pressure. *null* **28,** 75–126. ISSN: 0895-7959 (June 2008).

28. Abouelsayed, A., Thirunavukkuarasu, K., Hennrich, F. & Kuntscher, C. A. Role of the Pressure Transmitting Medium for the Pressure Effects in Single-Walled Carbon Nanotubes. *J. Phys. Chem. C* **114,** 4424–4428. ISSN: 1932-7447 (Mar. 2010).

29. Duwal, S. & Yoo, C.-S. Shear-Induced Isostructural Phase Transition and Metallization of Layered Tungsten Disulfide under Nonhydrostatic Compression. *J. Phys. Chem. C* **120,** 5101–5107. ISSN: 1932-7447 (Mar. 2016).

30. Klotz, S., Chervin, J.-C., Munsch, P. & Le Marchand, G. Hydrostatic Limits of 11 Pressure Transmitting Media. *J. Phys. D: Appl. Phys.* **42,** 075413. ISSN: 0022-3727, 1361-6463 (Apr. 2009).

31. Celeste, A., Borondics, F. & Capitani, F. Hydrostaticity of Pressure-Transmitting Media for High Pressure Infrared Spectroscopy. *High Press. Res.* **39,** 608–618. ISSN: 0895-7959 (Oct. 2019).

32. Rivers, M. *et al.* The COMPRES/GSECARS Gas-Loading System for Diamond Anvil Cells at the Advanced Photon Source. *High Press. Res.* **28,** 273–292. ISSN: 0895-7959 (Sept. 2008).

33. Henke, B. L., Gullikson, E. M. & Davis, J. C. X-Ray Interactions: Photoabsorption, Scattering, Transmission, and Reflection at E = 50-30,000 eV, Z = 1-92. *Atomic Data and Nuclear Data Tables* **54,** 181–342. ISSN: 0092-640X (July 1993).

34. Hirao, N. *et al.* New Developments in High-Pressure X-Ray Diffraction Beamline for Diamond Anvil Cell at SPring-8. *Matter and Radiation at Extremes* **5,** 018403. ISSN: 2468-2047 (Jan. 2020).

35. Smith, J. S. & Desgreniers, S. Selected Techniques in Diamond Anvil Cell Crystallography: Centring Samples Using X-Ray Transmission and Rocking Powder Samples to Improve X-Ray Diffraction Image Quality. *J Synchrotron Rad* **16,** 83–96. ISSN: 0909-0495 (Jan. 2009).

36. *Beamlines Information | Advanced Photon Source* https://hpcat.aps.anl.gov/technical-notes (2021).

37. Meng, Y., Hrubiak, R., Rod, E., Boehler, R. & Shen, G. New Developments in Laser-Heated Diamond Anvil Cell with in Situ Synchrotron x-Ray Diffraction at High Pressure Collaborative Access Team. *Review of Scientific Instruments* **86.** APS HPCAT methodology, 072201. ISSN: 0034-6748 (July 2015).

38. Goncharov, A. F. Raman Spectroscopy at High Pressures. *International Journal of Spectroscopy* **2012,** 1–16. ISSN: 1687-9449, 1687-9457 (Jan. 2012).

39. Ferraro, J. R., Nakamoto, K. & Brown, C. W. in *Introductory Raman Spectroscopy (Second Edition)* (eds Ferraro, J. R., Nakamoto, K. & Brown, C. W.) 1–94 (Academic Press, San Diego, Jan. 2003). ISBN: 978-0-12-254105-6.

40. Desgreniers, S. & Lagarec, K. XRDA: A Program for Energy-Dispersive X-Ray Diffraction Analysis on a PC. *J. Appl. Crystallogr.* **27,** 432–434. ISSN: 1600-5767 (1994).

Chapter 3

Room Temperature X-Ray Diffraction

X-ray diffraction (XRD) is a powerful and effective tool for non-destructive studies of the structure of materials *in-situ*. Though XRD has been used for structural investigations of boron nitride for a long time[1], determining a structure comparable to that of graphite[2], there is much fewer investigations under high pressure conditions and a wealth of conflicting reports on the measured elastic parameters in literature[3–6]. No study published so far has used N_2 as a pressure-transmitting medium (PTM), often opting for ones that introduce more non-hydrostatic strain such as NaCl. This also means that the use of high pressure conditions for nitrogen intercalation has yet to investigated in hBN.

In this chapter, structural responses to pressure and the high pressure phase transition from hBN to wBN as characterized by XRD are investigated. The elastic parameters of the materials in focus will be determined and the conditions for the formation of high-density phases will be discussed.

Relevant information regarding the structures of materials of interest are noted in Table 3.1. The information for hBN is placed next to that of graphite, which hBN is an electronic and structural analogue of, so that they may be easily compared. While at ambient conditions, hBN has slightly larger *a*-parameter and slightly smaller *c*-parameter compared to those corresponding to graphite, this change accounts for only about 2.1% difference in the c/a ratio. Upon compression above 9 GPa, a first-order phase transition occurs in BN, from the graphite-like structure of hBN to the wurtzite structure of wBN, characterized by a slight increase in *a*-parameter and a large drop in both the *c*-parameter and the resulting unit cell volume. As another structure, bct-BN, is predicted to form under simultaneous high pressures and high temperatures, it will be discussed in Chapter 5 (Heating under

Species	Space Group	a (Å, at P=0 GPa)	c (Å, at P=0 GPa)	Cell Volume (Å^3, at P=0 GPa)	Formation Conditions	Source
$C_{Graphite}$	$P\,63/m\,m\,c$	2.46	6.71	35.29	P=0	[7]
hBN	P -6 m 2	2.498	6.668	36.03	P=0	[8]
wBN	$P\,63\,m\,c$	2.536	4.199	23.39	P=9-12 GPa	[9]
bct-BN	$P\,4_2/mnm$	4.37	2.52	48.12	P=6-40 GPa, HT	[10,11]

TABLE 3.1: Structural and phase information of relevant solids, at room temperature. HT refers to high temperatures needed.

pressure).

Many separate samples were analyzed in this study, prepared using different PTMs and initial crystallinity. Unless otherwise noted, the studies presented in this chapter were carried out at room temperature, with the XRD done at the CLS HXMA beamline (06-ID1), using N_2 as a PTM. Nitrogen is a common high pressure PTM due to its relatively low cost, straightforward loading, and ability to maintain hydrostatic conditions up to 13 GPa, with pressure gradients less than 5% up to 25 GPa[12]. Other research teams have avoided using it in favor of NaCl, which shows small but notable pressure inhomogeneities to very low pressures as compared to nitrogen (a standard deviation around 0.25 GPa between pressures of 1-15 GPa[13]).

3.1 Analysis of the dense hBN structure

A sample of hBN was compressed past the transition point to wBN, then decompressed to near ambient, and finally compressed again to high pressures. The XRD plots for this series are shown in Figure 3.1. As expected, with increasing pressure the X-ray diffraction lines shift to higher scattering angles; the size of the interplanar spacings, which have decreased in response to pressure, are inversely proportional to the sin of twice the angle of diffraction, in accordance with Bragg's law.

$$2d \sin\theta = n\lambda \tag{3.1}$$

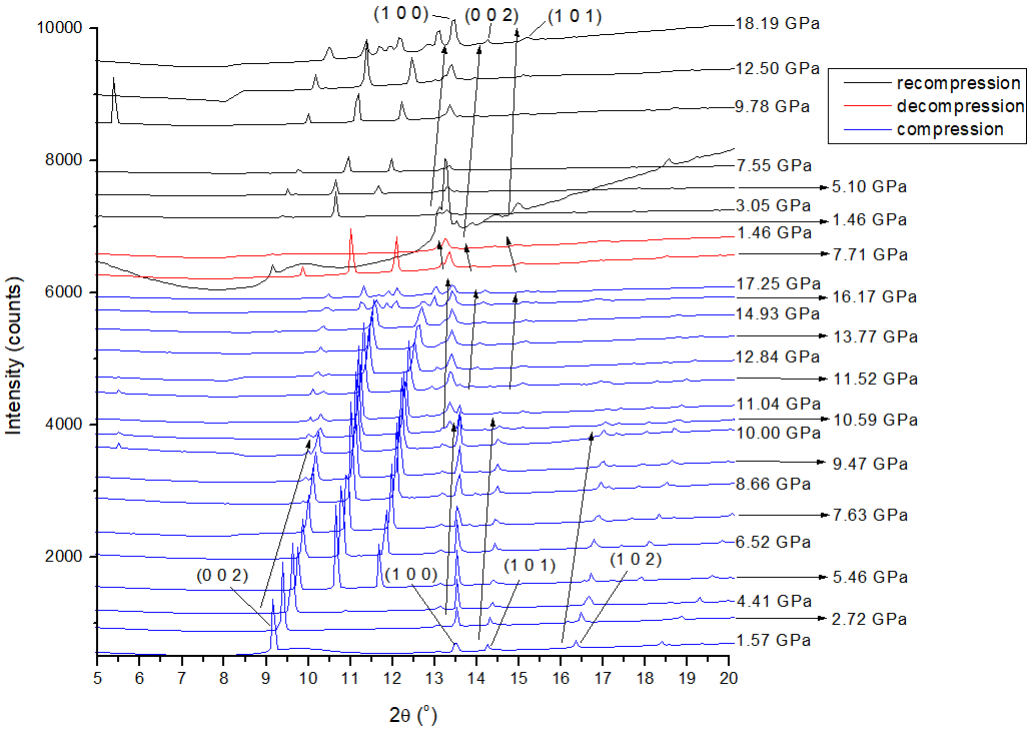

FIGURE 3.1: Progression of XRD patterns with pressure for a compression-decompression-recompression series of hBN with N_2 used as the PTM. A vertical offset is introduced for clarity. The relevant X-ray diffraction lines are labeled with their hkl indices and their progression is marked with arrows. The arrows starting at low pressure relate to phase I hBN, while those starting at high pressures relate to phase II wBN. Any unlabeled peaks are due to solid phases of the N_2 PTM. Note that the first X-ray diffraction pattern of the recompression portion has an unusual background and a broad hump centered around 9.7^o arising from liquid nitrogen scattering.

The most notable feature of the hBN X-ray diffraction pattern is the intense (0 0 2) line, corresponding to the spacings of basal planes. This line shifts more rapidly with pressure than the other lines, owed to the weak interaction between planes in the c-direction compared to the strong covalent bonds between B and N atoms in the basal plane. From 1.57 GPa to the final observation of hBN at 13.77 GPa, the c-parameter decreases by 13$\pm$0.9%, whereas the a-parameter only changes by 0.9$\pm$0.1%, as shown in Figure 3.2. This makes the (0 0 2) line a much better initial gauge of the expansion or compression of hBN for further studies.

The pressure evolution of the unit cell volume was fitted to an equation of state which

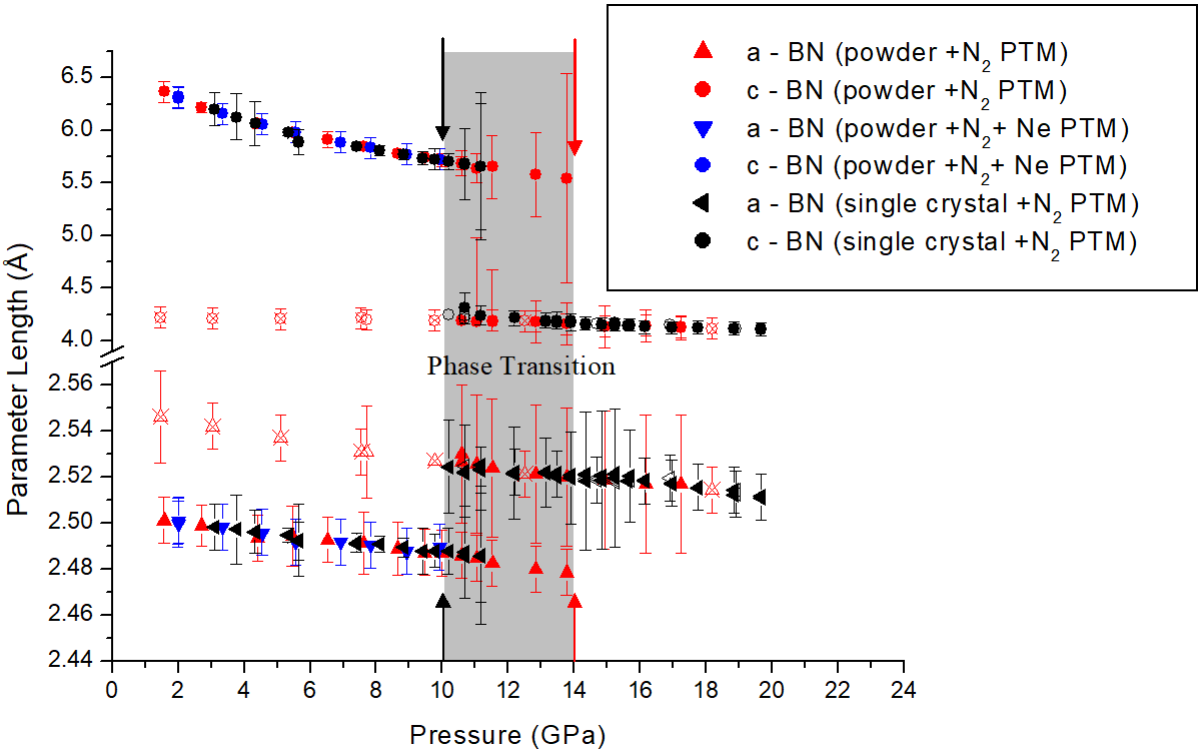

FIGURE 3.2: Lattice parameters as a function of pressure, as measured by X-ray diffraction from several hBN samples. Hollow data points represent values for which the samples have been decompressed following the phase transition to the high-density wBN phase. The grey region drawn from 9-11 GPa shows the partial transition, where there is a coexistence of both phases. Note the split scale in the vertical axis.

relates volume to pressure. Typically, an equation of state depends upon the initial cell volume, the bulk modulus, and the linear pressure derivative of the bulk modulus, B_0', defined such that

$$B(P) = B_0 + B_0' P \tag{3.2}$$

and is unitless. This allows for the determination of the bulk modulus and its pressure derivative by a proper fit of the experimental volume data. The first-order Murnaghan (M EoS), third-order Birch-Murnaghan (B-M EoS), and Vinet-Rose (V-R EoS) equations of state were chosen. The M EoS

$$P(V) = \frac{B_0}{B_0'}[(\frac{V}{V_0})^{-B_0'} - 1] \tag{3.3}$$

assumes a linear change with pressure of the bulk modulus B_0, whereas the third order B-M EoS

$$P(V) = \frac{3B_0}{2}[(\frac{V_0}{V})^{7/3} - (\frac{V_0}{V})^{5/3}]\{1 + \frac{3}{4}(B_0' - 4)[(\frac{V_0}{V})^{2/3} - 1]\} \tag{3.4}$$

assumes a non-linear variation with pressure. The V-R EoS has an exponential dependence on pressure for B_0, defined such that

$$P = [3B_0(1-x)/x^2]\exp[\eta(1-x)] \tag{3.5}$$

where $x = (\frac{V_0}{V})^{1/3}$ and $\eta = \frac{3}{2}(B_0' - 1)$.

A χ-squared minimization of the data was performed for the three equations of state, using parameters B_0 and B_0'. The χ-squared function is defined such that

$$\chi^2 = \Sigma_i(O_i - E_i)^2 \tag{3.6}$$

where the sum is over all elements in our data set, O_i a given observed value, and E_i the value expected from the EoS. This minimization was done numerically through the use of the "Solver" extension in Microsoft Excel[14]. Interestingly, despite differences in crystallinity, pressure medium, and hydrostatic quality, the results were similar enough between each of the sample series for each respective equation of state that the fitting could safely be performed on a compilation of all the data. The relation between the cumulative χ^2 and the fitting parameters is shown in Figure 3.3, which shows that the minimal region of the χ^2 tends to be ellipses with a negative linear or slightly nonlinear relation between the two parameters. These ellipses are likely related to the covariance between the two parameters as they relate to the EoS. No other local minima in the chi squared relations were found for any of the equations of state, even near previously reported values[3,5].

The fitting returned different values for B_0 and B_0' for each equation of state shown in Table 3.2, as expected according to Ooi *et al.*[15]. Plotted in Figure 3.4, each of these

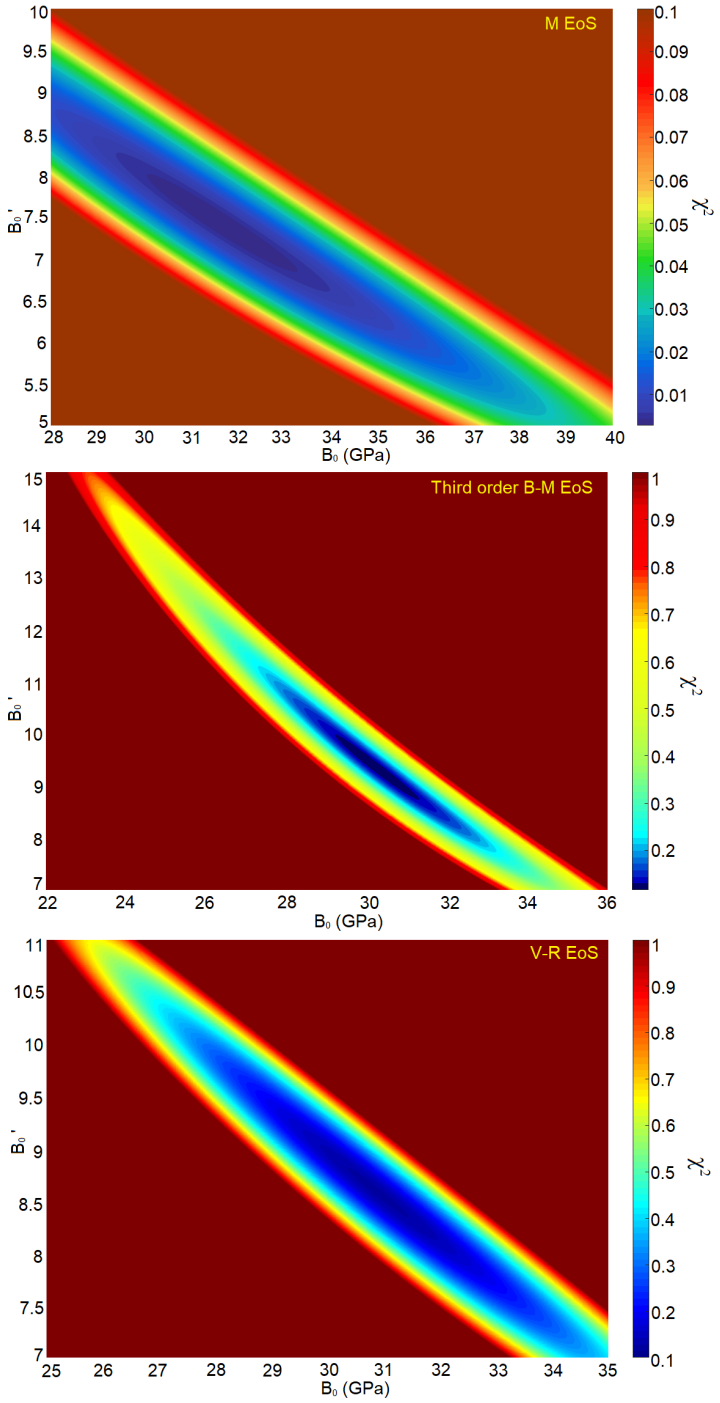

FIGURE 3.3: Chi-squared minimization relations for pressure with changing bulk modulus and pressure derivative of bulk modulus. The relations are plotted for three selected high pressure equations of state as applied to the measured volume of hBN with pressure. The global minimum, which drops off exponentially, is taken as the fitted values of B_0 and B_0'. The colour denotes the Chi-squared total, with higher values presented as more red (worse fit). Note that the colour scale for the M-EoS is different than the other two plots for clarity.

B_0 (GPa)	B_0'	EoS used	Source
36.7 ±0.5	5.6 ±0.2	1st order M EoS	*Solozhenko, Will, Elf - 1995*[5]
27.6 ±0.5	10.5 ±0.5	3rd order B-M EoS	*Le Godec et al. - 2000*[4]
20 ±2	17 ±2	3rd order B-M and P-M EoS	*Fuchizaki et al. - 2008*[3]
29.1 ±0.4	9.1 ±0.3	Anderson EoS	*Urakawa et al. - 1995*[6]
31.5 ±0.6	7.4 ±0.1	1st order M EoS	this study
29.8 ±1	9.7 ±0.1	3rd order B-M EoS	this study
30.4 ±0.4	8.9 ±0.1	Vinet-Rose EoS	this study

TABLE 3.2: Previously and currently reported bulk modulus and its pressure derivative. The equation of state fitted for determination of the parameters is noted, where M is in place of Murnaghan, B-M for Birch-Murnaghan, and P-M for Parsafar-Mason[17].

resulting equations are paralleled in their relation to the data, such that we can confirm that the results of the three are simultaneously valid. While elastic theory shows that stiffer materials have a B_0' of close to 4, higher values have been shown for other layered materials such as graphite (with a B_0 and B_0' of 33.8 GPa and 8.9, respectively[16]).

The average between the three equations gives $B_0 = 30.6 \pm 0.5$ GPa and $B_0' = 8.7 \pm 0.7$. The result of using these values for each EoS is shown in Figure 3.4: the quality of fit is maintained for the V-R EoS, while it is worse for the B-M EoS, and inadmissible for the Murnaghan EoS. It must then be stated that, while the V-R EoS does seem to show forgiveness to small differences in the values used for elastic parameters, that care should be taken when comparing elastic parameters derived from different models.

As evidenced by the results of Table 3.2, there has been a wealth of conflicting reports with regard to these parameters. It is noted that these differences occur regardless of equation of state employed. Calculated by Fuchizaki[3], the temperature dependence of the bulk modulus, $(dB_{0T}/dT)_V = 1 \times 10^{-2}$ GPa/K, is somewhat too small to account for these differences in room temperature; this could only contribute to the uncertainty in a small proportion. Moreover, first-principles calculations have shown that many layered structures are possible in the hBN system due to differences in stacking sequence[18]. According to published reports, true structural nature of hBN may then be that of a mixed

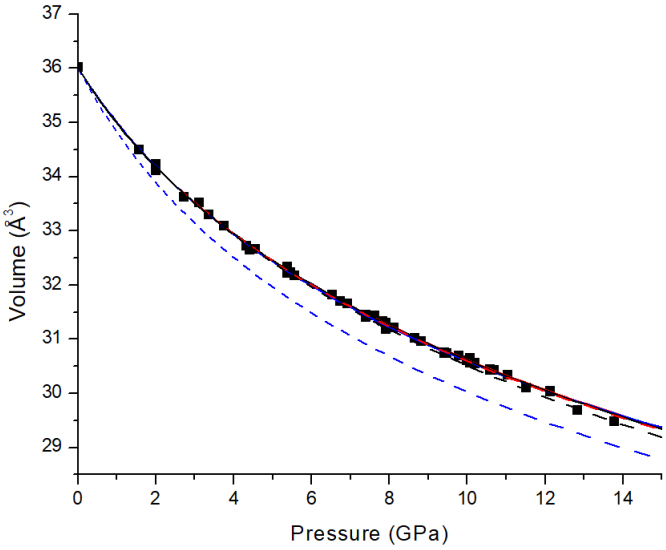

FIGURE 3.4: Fitted EoSs for hBN. The solid lines depict the equations of state using the fitted parameters (Table 3.2) for the BM-EoS (black), the M-EoS (blue), and the VR-EoS (red). The dashed lines depict those equations using the parameters taken from the average of the three fits. The solid lines being hard to differentiate from each other shows that they are in good agreement, and they are indeed well fit to the given data. However, the exchange of parameters for the average values $B_0 = 30.6 \pm 0.5$ GPa and $B_0' = 8.7 \pm 0.7$ leads to a measurable change in the B-M EoS and a drastic change to the Murnaghan EoS, such that the equations no longer are in a good fit.

structure of three energetically degenerate layered structures, two belonging to $P6_3/mmc$ while another to $P3m1$. True to the diffraction conditions of these symmetry groups, a (0 0 4) peak is observed in most patterns which, as Fuchizaki[3] points out, is curiously missing from the classic hBN structural investigations such as Solozhenko's[5].

Another possible explanation for these differences is nonhydrostatic conditions leading to a rise of unisotropic pressure response[3]. Considering all of the cited reports are for experiments with an NaCl PTM (or a combination of that and MgO[4]), the differences in hydrostaticity should be at least comparable between all the studies, and wouldn't reasonably lead to the great variation observed. N_2 PTM has been shown to maintain minimal pressure gradients and maintain essential hydrostaticity until above 10 GPa[12], which is considerably higher than for NaCl, which maintains a fairly stable but small gradient up to 14 GPa[13]. The lack of a resolution by the use of a better PTM points to a need for further

explication for these differences.

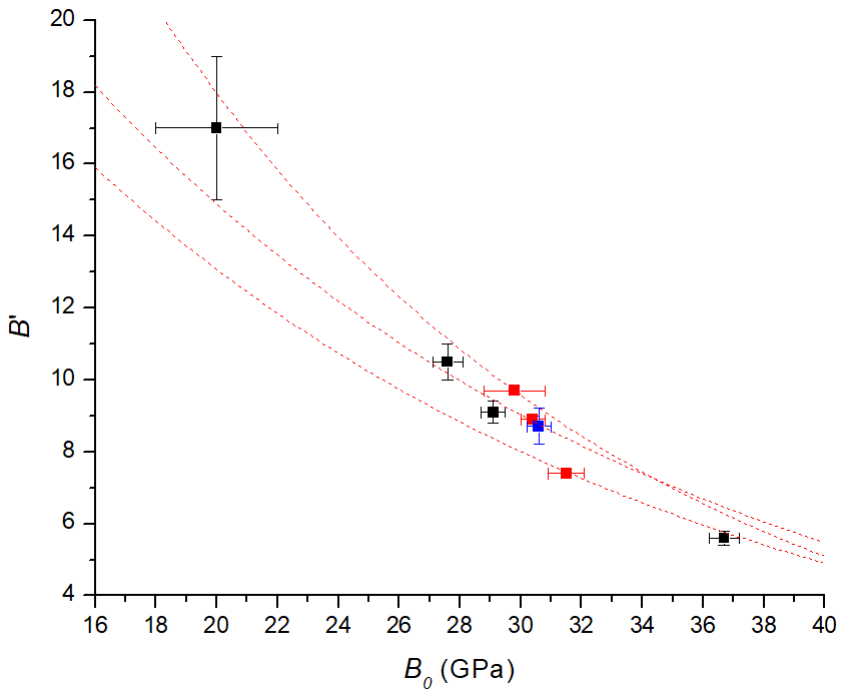

FIGURE 3.5: Graphical representation of reported elastic parameters B_0 and B_0' for hBN. In black are values from previous reports by Fuchizaki[3], Le Godec[4], Urakawa[6], and Solozhenko[5] respectively left to right. Our findings for different EoSs are shown (red), and their average (blue). The red dotted lines represent the covariance curves.

The elastic parameters presented in Table 3.2 are plotted out in Figure 3.5. Here it is clearly demonstrated that the chosen EoS does indeed have a considerable impact on the fitted result, but not enough to bridge the gap between various reports. This also communicates the consistency of a relation between B_0 and B_0' that was illustrated by the confidence ellipses in Figure 3.3: A smaller B_0 implies a larger B_0' and vice versa.

All of the reports lay near the extrapolation of the major axes of the χ^2 ellipses of one of the fittings, but there is not convergence near any singular point; the major axis of the χ^2 from the 3rd order B-M EoS extrapolates towards the reports of both Fuchizaki and Le Godec[3,4], while that from the 1st order Murnaghan EoS points towards the report of Solozhenko[5]. Only the parameters reported by Le Godec[4] lie anywhere near the parameters we now report. While the parameters reported separately by Le Godec and

Urakawa[4,6] align with the curve for our V-R EoS, it should be noted that these two studies did not employ this EoS and therefore these parameters cannot be readily compared.

While there have been proposals for hBN to be used as a PTM and pressure calibrant due to the great variation of volume with pressure[3,19], the necessary step of standardization of the structural pressure response is yet to be obtained despite internal consistency, and thus the use of hBN as a potential pressure calibrant is still not globally viable.

3.2 Analysis of the wBN structure

Starting above 9 GPa, a transition is observed for BN, marked by the decrease in intensity of the phase I hBN lines and the appearance of phase II wBN lines. Because of the overshadowing intensity of the solid N_2 lines, as illustrated in Figure 3.1, the specific changes across this transition are better represented differently as in Figure 3.6, which gives a detailed presentation of the X-ray diffraction pattern before and after the transition. The characteristic (0 0 2), (1 0 0), and (1 0 1) lines of hBN weaken in intensity as pressure increases across the coexistence range, while the wBN lines of the same hkl indices appear with growing intensity the same pressure range.

There are a few notable differences of the wBN diffraction pattern compared to that of hBN. Particularly, the (0 0 2) line of wBN appears between the (1 0 0) and (1 0 1) lines, illustrated in Figure 3.6, representing a difference of around 25% in the *c*-direction between the two structures. This is the evidence of a denser material; the (0 0 2) line being scattered at a wider angle than the (1 0 0) line indicated that the value of the *c*-parameter is now less than twice that of the *a*-parameter. Interestingly, the value of the *a*-parameter does increase across the transition, marked by the shift to lower diffraction angle, although only by about 1.5%. The (0 0 2) line of the high pressure phase is also quite weak, making it measurable only once there is more wBN, that is to say toward the higher pressure end of the coexistence region (and beyond, for that matter).

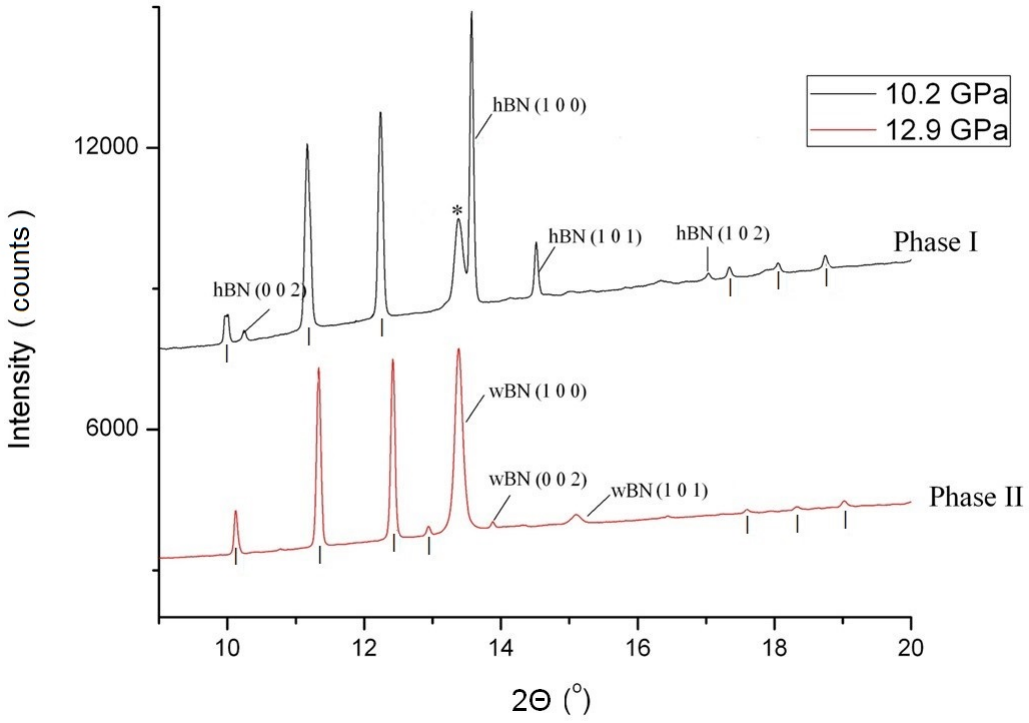

FIGURE 3.6: XRD patterns from before and after the phase transition from hBN to wBN in a nitrogen medium. The most notable diffraction feature differentiating hBN from wBN is the displacement of the (0 0 2) diffraction line due to the contraction in the *c*-axis upon the transition. Diffraction lines from the solidified nitrogen are observed and noted with "|". A peak potentially related to the (1 0 0) line of wBN is marked with "∗".

The changes observed for the (1 0 0) and (1 0 1) lines are less immediately evident. The wBN (1 0 0) line lies at a 2θ value about 1.5% lower than the (1 0 0) of hBN, making it hard to discern in the coexistence region. As shown in Figure 3.7, the FWHM of those lines can be used to differentiate them in place of their relative angles. While the FWHM of the hBN (1 0 0) line is a consistent value of $FWHM_{hBN(100)} = 0.052 \pm 0.001^o$, that of wBN is around twice that value, $FWHM_{wBN(100)} = 0.111 \pm 0.002^o$. There is also a demonstrable increase with pressure, likely owed to the non-hydrostatic stresses expected by the nitrogen PTM above 10 GPa, according to literature[12]. Interestingly, there is a large jump in the (1 0 0) FWHM around 14 GPa, but observed only for single crystal. This is likely caused by the transition of nitrogen to the δ^* phase[20]. The single crystal of hBN is likely confined between forming crystal grains of the nitrogen solid, causing stress upon the structure,

whereas the crystallites of the powder are small enough not to be affected by these grain boundaries. This is supported by the fact that we observe the FWHM fall back to average, unstressed values upon decompression and crossing the $\delta - \delta^*$ phase boundary around 14 GPa[20]. Apart from the values for stressed single crystal, the FWHM of the (1 0 0) line is consistent, with a value of $FWHM_{wBN(100)} = 0.111 \pm 0.002^o$ below 10 GPa, thereafter increasing by a factor of about 0.005^o/GPa.

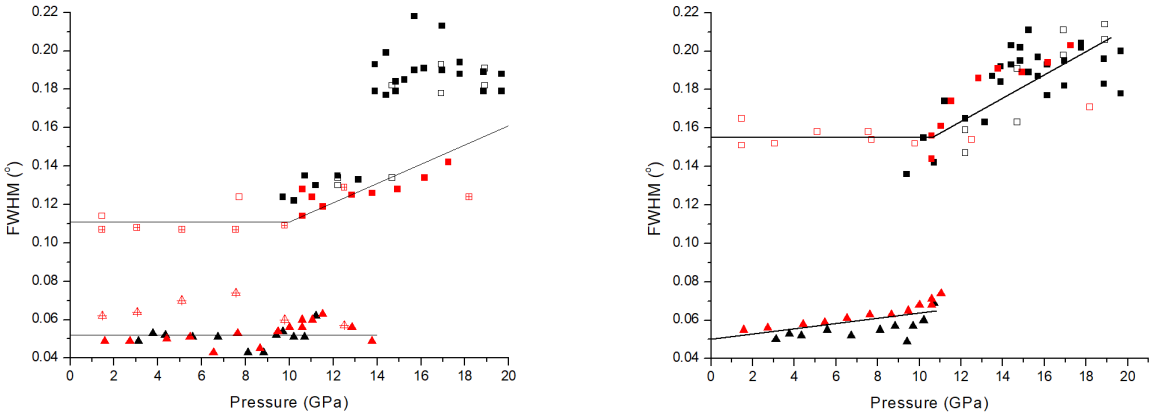

(A) (1 0 0). (B) (1 0 1).

FIGURE 3.7: Variation of the FWHM for selected diffraction lines under pressure. Data points for single crystalline sample are shown in black, while those from powdered sample are shown in red. Points corresponding to hBN are marked with triangles; those for wBN are noted with squares. Hollow symbols are for data taken upon decompression, and partially filled symbols for any following compression. Straight lines are guides to the eye.

The linewidth of the (1 0 1) diffraction lines tell a similar story. The (1 0 1) line is consistent below 10 GPa with a value of $FWHM_{hBN(101)} = 0.058 \pm 0.001^o$, which rapidly increases above 10 GPa as conditions become less hydrostatic. The lines from powdered samples are also noticeably higher than that of single crystalline sample. This can be attributed to grain size broadening: the peak width is inversely proportional to the crystallite sizes in XRD[21]. Below 10 GPa, the FWHM of the wBN (1 0 1) is also consistent, with a value of $FWHM_{wBN(101)} = 0.153 \pm 0.003^o$. Above 10 GPa, however, the linewidth spans a large range of values, ranging from 0.14^o to 0.022^o.

The substantial difference in FWHM between hBN and wBN lines indicates a difference in size, strain, or defect concentrations. The effect of crystallite size on the FWHM is shown more clearly in the (1 0 1) plot for hBN when comparing powder to single crystal, which is not nearly enough to explain the close to 3× difference following the phase transition. Strain undoubtedly plays a role, but nonhydrostatic strain is only observed above 10 GPa. This seems to imply that the origins of the large wBN line width could be due to defect concentration. Methods to determine this by XRD unfortunately require good data with a high S/N ratio, which is especially hard for microscopic quantities of low Z materials like BN. A high concentration of defects in the material that remains on the decompression corroborates that defects may help to stabilize the structure at low pressures[22]. Furthermore, luminescent defects could be the cause of the massive background observed in Raman spectroscopy experiments upon the phase transition, as discussed in Chapter 4. Around the coexistence region of hBN and wBN, wBN diffraction lines lay close to and are convoluted with those of other phases present; the marked difference in FWHM of lines in the two phases can serve to reliably distinguish the identity of diffraction lines within the coexistence region. Without proper use of these tools, incorrect structure fits can be (and have been) easily made, resulting in many hours of lost productivity.

As alluded in the linewidth analysis, no further phase transitions are observed in BN up to 20 GPa at room temperature. After releasing the pressure down to 1.46 GPa, wBN remains present and a small fraction of hBN reappears, indicating that the transition is partially reversible down to near ambient. The following recompression of wBN helps in giving insight into the structural response to pressure in lower pressure regions. This compression-decompression-recompression cycle was only successful for a single sample series, on a hBN powder sample due to gasket failures during other attempted decompressions.

Much like in the analysis of hBN, the response of the volume to pressure allows for an estimation of elastic parameters by fitting a high pressure equation of state. Interestingly,

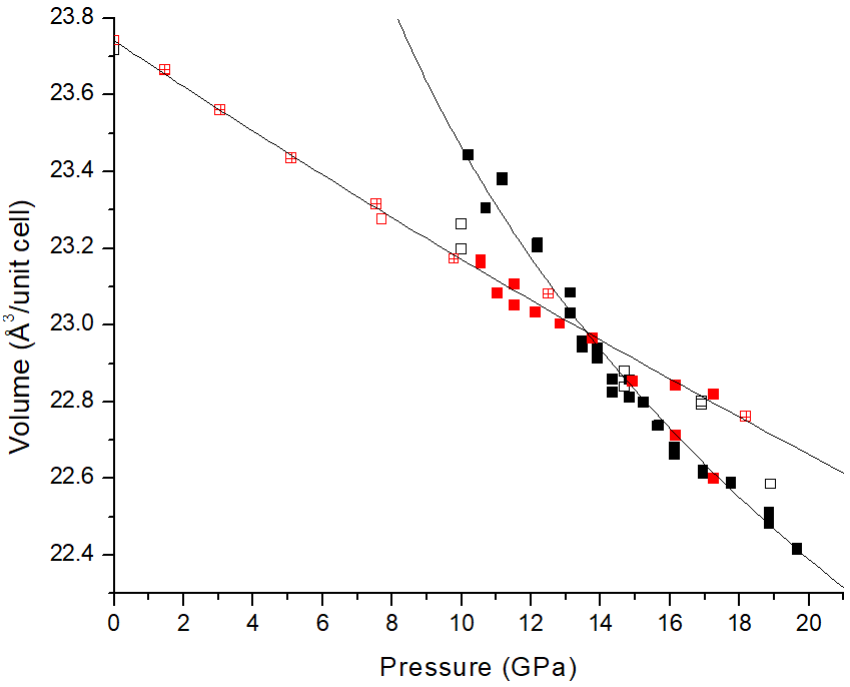

FIGURE 3.8: Cell volume data for wBN under pressure with fitted EoSs. Single crystal plotted in black, with powder samples in red. The empty data points denote decompression data, whereas the partially filled points note recompression. The lines represent the fitted EoS for the two high pressure trends.

as shown in Figure 3.8, two trends to this data appear. One trend is maintained upon decompression and subsequent recompression for both crystalline types, whereas the other, more compressible trend disappears upon decompression.

The emergence of such a splitting is due to identification of the (0 0 2) of wBN. Upon transition to the wBN phase, a new line appears with a d-spacing of 2.12 Å at 11.2 GPa. Because its emergence is paired with the other wBN lines, and because it persists across multiple phases of nitrogen, this diffraction line can be safely assumed to be associated with the sample. Furthermore, since it exists in the region where the wBN (0 0 2) would exist, and without any other nearby features for many patterns, this line is taken as the wBN (0 0 2) line, providing a good structural fit for the available wBN lines. However, it should be noted that this diffraction line is much sharper than the other wBN peaks, hosting a FWHM of around 0.06^o while the other major lines have a FWHM of closer to

0.14^o. Furthermore, for the powder samples, there is another line with a larger d-spacing similar to this line, which also provides an equally satisfactory fit to for the available diffraction lines, providing a much closer fit to the EoS expected by Solozhenko[23]. This raises the question: which diffraction line is the genuine (0 0 2)?

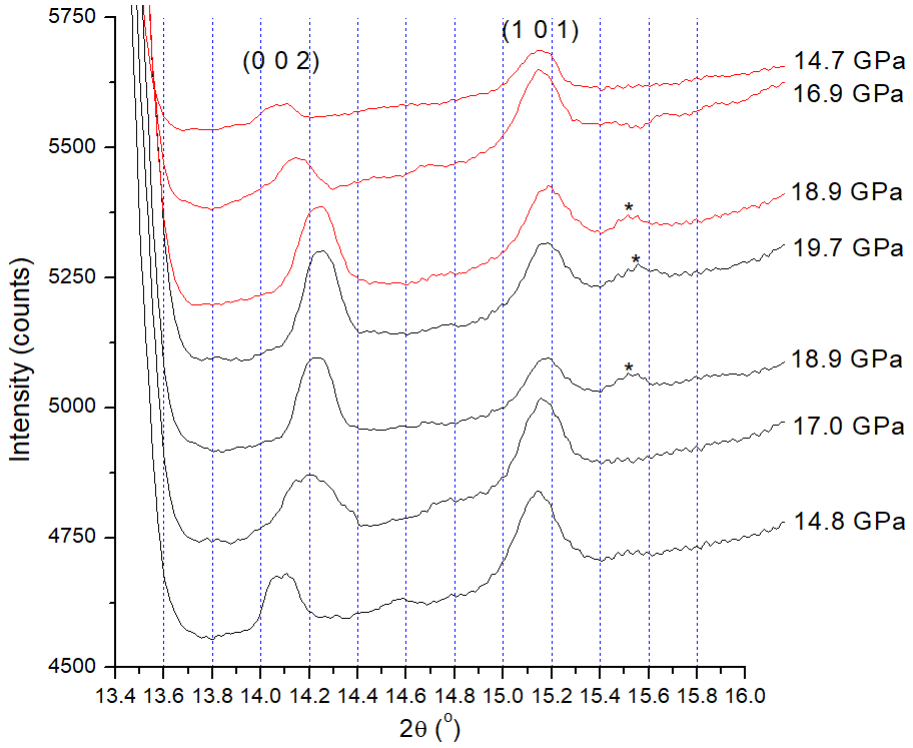

FIGURE 3.9: Close-up inspection of the (0 0 2) of wBN for similar pressures on the compression and decompression on the single crystal sample. The compression patterns are in black, while the decompression is in red. Both identified lines refer to the wBN structure. The large curve around 13.2 ^{o} leads to the wBN (1 0 0) line. The weak line the appears above 17 GPa, marked with "*" belongs to the nitrogen ϵ phase.

Comparing the identified wBN (0 0 2) diffraction line in Figure 3.9, there doesn't seem to be any major differences between the line at similar pressures on the upstroke or downstroke. The downstroke (0 0 2), however, is what causes the transition from one trend to the other, as marked in Figure 3.8. The lack of any other phase(s) leads us to believe this is the genuine behavior of wBN, and that our structural fits are accurate. For the two trends, we should then do two separate analyses. The resulting EoSs of both are plotted in Figure 3.8.

For low-compressibility materials such as diamond and cBN, an approximation to the equation of state can be used by taking $B_0' = 4$, leading to the second order BM EoS

$$P = \frac{3}{2}B_0((\frac{V_0}{V})^{7/3} - (\frac{V_0}{V})^{5/3}) \tag{3.7}$$

A χ^2 minimization is performed on this EoS, applied to the cell volume data for the low-compressibility trend of wBN. The bulk modulus of wBN is determined with a V_0= 23.74Å to be B_0= 391 GPa, which is higher than that measured for cBN with, Birch B_0= 369 GPa and B_0'= 4 with the Birch equation of state[24], or B_0= 387 GPa and B_0'= 3.06 with the Birch-Murnaghan equation of state[25]. As a high hardness is related to a high bulk modulus, this supports loosely proposal of wBN being harder than cBN. This hardness can be calculated, as

$$H_V = 2(\frac{G^3}{B_0^2})^{0.585} - 3 \tag{3.8}$$

where B_0 is the bulk modulus, G is the shear modulus, and H_V is the Vickers hardness as reported by Chen[26]. The shear modulus reported by Deura[27] lead to a value of 70.8 GPa, whereas cBN has a hardness of 67.1 GPa based on the values reported by Zhang[28]. In fact, using the bulk modulus of wBN reported by Deura[27], the hardness calculated in this case is 84 GPa. Comparisons are made in Table 3.3 with structurally similar materials such as the isostructural hexagonal diamond, or the softer wurtzite AlN, as well as other competing ultrahard materials of interest.

Since the secondary trend observed in Figure 3.8 demonstrates an appreciable compressibility, B_0' must also be considered, considering in for this case a VR EoS. The χ-squared minimization returned B_0=8.4 GPa, B_0'=21.4, and V_0=28.1Å^3. Such a small B_0 indicates this is an incredibly compressible structure, even more-so than hBN, which points towards this not being a genuine phase due to a misinterpretation of the (0 0 2) line. Otherwise, this phase may be caused by a high density of defects, which is corroborated by the

Material	$\rho(g/cm^3)$	B_0 (GPa)	B_0'	G (GPa)	H_V (GPa)	source
C (diamond)	3.52	446	4	538	115	[29]
		443		535	96	[30]
wAlN	3.26	220	3.6	139	17.9	[31]
C (lonsdaleite)	3.49	442	3.8	613	122 *	[32]
wBN	3.47	392 ±5	4	-	68±1 *, using G from[27]	this work
		330	-	410	84 *	[27]
	3.47	407		394		[33]
					46	[34]
cBN	3.49	381	4	399	67 *	[28]
					61	[35]
	3.48	401		410		[33]
	3.49	369	4			[24]
	3.49	387	3.06			[25]

TABLE 3.3: Elastic parameters of wBN and similar materials. H_V values marked with "*" calculation are based on the Chen model for hardness[26]. Our calculation for wBN uses the shear modulus reported by Deura[27].

large increase in other wBN, shown in Figure 3.7, for conditions where this potential (0 0 2) line exists. Studies of single crystal hBN to higher pressures, and especially with different PTMs or paired with IR studies, may help to elucidate the true nature of this diffraction line and potential phase. Unfortunately, attempts to do so revealed too low an XRD signal from the sample, due to having a sample thin enough to perform IR spectroscopic studies.

The end result of these studies can be shown in Figure 3.10, where data from both phases are plotted alongside one another. The planar d-spacings of uninterpreted diffraction lines are represented in Figure 3.11. For single crystal, no unidentified diffraction lines exist above 15.7 GPa, reaffirming the confidence in the identifications of existing lines. However, for the powder sample, many such unidentified lines persist throughout the decompression and recompression. Both powder and single crystal have such unknowns below 9 GPa, below the transition and within the easily fitted cubic δ phase of nitrogen, limiting opportunities for confusion with a more complicated structure arising from the PTM. Furthermore, based on the groupings shown by the colours in Figure 3.11, these unidentified lines are present in both single crystal and powder data.

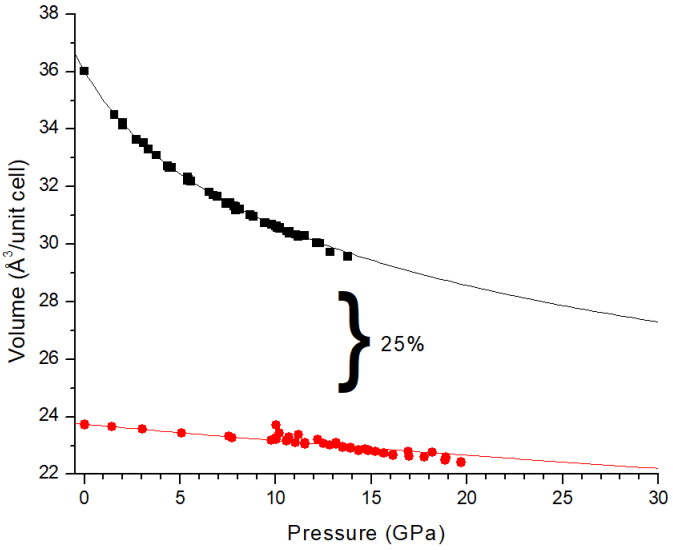

FIGURE 3.10: Compression of BN cell volume with pressure. The corresponding equations of state are drawn by lines. Data from phase I (hBN) are shown in black, with phase II (wBN) in red, with equations of state matching in colour. Note that the unit cells of both wBN and hBN contain the same number of B and N atoms, so the density changes in a similar fashion to the volume.

Considering these additional diffraction lines appear at pressures where only diffraction lines from hBN and δN are expected, and the fact that no new lines are observed in studies without N_2, a possible new phase with a different structure may have arisen from the incorporation of nitrogen into the hBN lattice: a new compound could have formed. This compound, if present, is more effectively stabilized in the powdered samples. This observation is certainly consistent with how intercalation occurs in layered materials. The structures of predicted hBN intercalation compounds, however, would not provide a diffraction pattern in agreement with the diffraction lines present. Furthermore, following the phase transition, the novel B_2N_3, B_3N_4, and B_3N_5 structures aren't formed either, as predicted in several other studies[36–38]. The intermediary phase of bct-BN[10,11,39] is not formed either, considering that the X-ray diffraction pattern expected for such a structure does not match. Vibrational spectroscopy does not reveal any new structures either, although Raman spectroscopy is a less practical tool upon formation of luminescent wBN. This means that if a new structure exists, it has no Raman-active modes and only

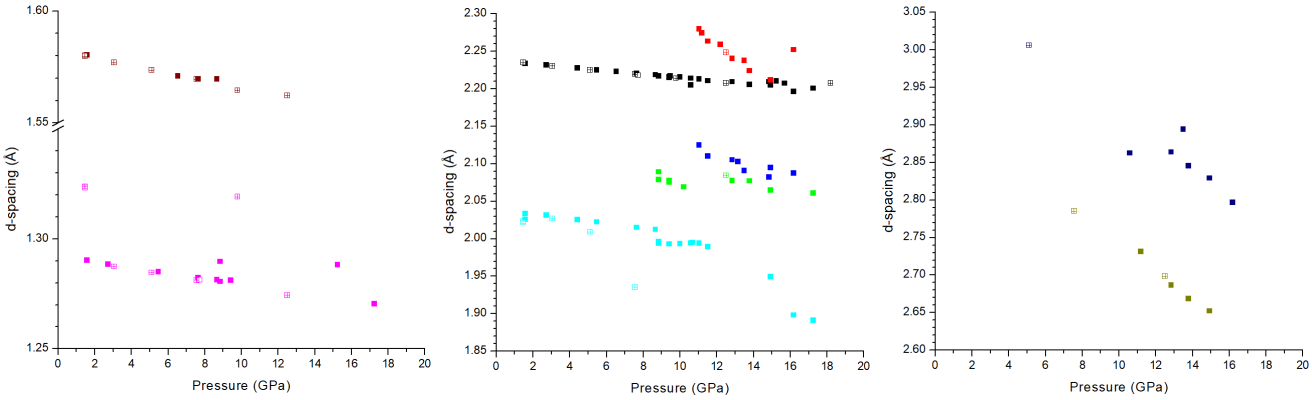

FIGURE 3.11: All planar d-spacings of unidentified diffraction lines from all XRD patterns. The colours represent like X-ray diffraction lines. Empty points note decompression, while partially filled points note recompression. Colours indicate like diffraction lines, meaning those that are likely related to the same hkl of the material.

exists in insufficient quantities well above the transition to wBN to be detected and well studied.

3.3 Analysis of retrieved samples

XRD analysis was performed on samples, retrieved (removed from the DAC) from high compression, using the in-house X-ray diffractometer. The analysis revealed that in all retrieved samples, including those used for studies using techniques other than XRD (such as spectroscopic methods) contained a mixture of hBN and wBN. The unit cell volume of retrieved hBN is observed to be slightly larger than the original V_0, by a maximum of 2.5% for any of the given samples. This corresponds with the estimation made based on the Raman shift of the E_{2g} line, confirming that the downshift is caused by structural expansion as discussed in Chapter 3.

A quantitative analysis was done to determine the relative concentrations of phases I and II. By dividing the integrated intensity of a given X-ray diffraction line by the scattering power calculated by the structure factor, a normalized intensity can be made. The sum of the integrated intensities of all available diffraction lines, divided by the sum of

sample type	PTM	% wBN
recompressed powder	N_2	>90
powdered	N_2	61
powdered	N_2	>70
powdered	N_2	40
single crystalline	N_2	>65
powdered	none	<55
powdered	none	40
powdered	none	<20

TABLE 3.4: Recovery phase ratios of several experiments, as determined by quantitative XRD analysis.

that for the expected scattering power can give a theoretical quantity, however this quantity would not be accurate due to beam interactions with the diamonds and gasket (the beam size of the in-house XRD system is larger than that of the gasket hole of most samples). However, by dividing the scattering quantity of one phase by the other, a more accurate account of the relative quantities can be ascertained.

The amount of phase II to phase I for several experiments are shown in Table 3.4. Impressively, the recompressed powdered sample in N_2 resulted in a 98.5% yield of wBN, despite the amount of unidentified X-ray diffraction lines present throughout the pressurization. This is many times more than any other similar series, which showed at most 75% wBN remaining. Meanwhile, powdered samples compressed without any PTM retained only 20-55% of the wBN. This points towards good PTMs, or at least nitrogen, being conducive to a higher retention of wBN since, for all but one sample, there was a higher concentration of wBN than in the worst of those without a PTM. The outlier for the powder in N_2 retention had graphite present in the cell (in the interest of heating), which would have provided a nucleation point for like structures, such as hBN, to grow, bringing the wBN yield down to 40%.

More of such quantitative analyses should be done on samples with other PTMs and samples that are recompressed to elucidate the weight of each factor in the retention of wBN. This should be paired with further experiments to answer outstanding questions,

such as the true nature of the possible wBN (0 0 2) line observed dominantly in single crystal samples. The initial compressions were kept to below a maximum pressure of 20 GPa to preserve gasket integrity with the intention of doing a recompression; this was an unexpected limitation on the single crystal data especially, so an experiment that goes to a much higher maximum pressure before decompression should give important insight into the nature of certain diffraction lines, and the corresponding structures. XRD was also not performed on any samples compressed without a PTM. The effect which this would have on the linewidths, insight into defect concentrations, and its effect on wBN retention would potentially lead to conclusive evidence about proposed wBN stabilization by defect networks[22]. Finally, none of our experiment was capable of pairing consecutive XRD and spectroscopic analyses on a single sample. While there is a wealth of data from experiments done on matching experimental assemblies for all techniques employed, one can't be used to fully describe any unknown issues with the other. Furthermore, as discussed in Chapter 4, pairing XRD with simultaneous measurements with Raman measurements would clarify the nature of heating due to laser-defect coupling and resulting spectroscopic shifts.

Bibliography

1. Bundy, F. P. & Wentorf, R. H. Direct Transformation of Hexagonal Boron Nitride to Denser Forms. *1144* **38,** 7 (1963).

2. Pease, R. S. An X-Ray Study of Boron Nitride. *Acta Cryst* **5,** 356–361. ISSN: 0365110X (May 1952).

3. Fuchizaki, K., Nakamichi, T., Saitoh, H. & Katayama, Y. Equation of State of Hexagonal Boron Nitride. *Solid State Communications* **148,** 390–394. ISSN: 0038-1098 (Dec. 2008).

4. Godec, Y. L. *et al.* Thermoelastic Behaviour of Hexagonal Graphite-like Boron Nitride. *High Press. Res.* **17,** 35–46. ISSN: 0895-7959 (Mar. 2000).

5. Solozhenko, V. L., Will, G. & Elf, F. Isothermal Compression of Hexagonal Graphite-like Boron Nitride up to 12 GPa. *Solid State Commun.* **96,** 1–3. ISSN: 0038-1098 (Oct. 1995).

6. Urakawa, S., Morishima, H., Kato, T., Suzuki, A. & Shimomura, O. Equation of State for *H*-BN. *Photon Fact. Act. Rep. 11196* 383 (2004).

7. Bosak, A., Krisch, M., Mohr, M., Maultzsch, J. & Thomsen, C. Elasticity of Single-Crystalline Graphite: Inelastic x-Ray Scattering Study. *Phys. Rev. B* **75,** 153408 (Apr. 2007).

8. Budak, E. & Bozkurt, Ç. Synthesis of Hexagonal Boron Nitride with the Presence of Representative Metals. *Physica B: Condensed Matter* **405,** 4702–4705. ISSN: 0921-4526 (Nov. 2010).

9. Xu, Y.-N. & Ching, W. Y. Electronic, Optical, and Structural Properties of Some Wurtzite Crystals. *Phys. Rev. B* **48,** 4335–4351 (Aug. 1993).

10. Hromadová, L. & Martoňák, R. Pressure-Induced Structural Transitions in BN from *Ab Initio* Metadynamics. *Phys. Rev. B* **84,** 224108. ISSN: 1098-0121, 1550-235X (Dec. 2011).

11. Wen, B., Zhao, J., Melnik, R. & Tian, Y. Body-Centered Tetragonal B_2N_2: A Novel Sp3 Bonding Boron Nitride Polymorph. *Phys. Chem. Chem. Phys.* **13,** 14565. ISSN: 1463-9076, 1463-9084 (2011).

12. Klotz, S., Chervin, J.-C., Munsch, P. & Le Marchand, G. Hydrostatic Limits of 11 Pressure Transmitting Media. *J. Phys. D: Appl. Phys.* **42,** 075413. ISSN: 0022-3727, 1361-6463 (Apr. 2009).

13. Celeste, A., Borondics, F. & Capitani, F. Hydrostaticity of Pressure-Transmitting Media for High Pressure Infrared Spectroscopy. *High Press. Res.* **39,** 608–618. ISSN: 0895-7959 (Oct. 2019).

14. *Excel Solver* Frontline systems, Inc.; Optimal Methods, Inc.

15. Ooi, N., Rajan, V., Gottlieb, J., Catherine, Y. & Adams, J. B. Structural Properties of Hexagonal Boron Nitride. *Modelling Simul. Mater. Sci. Eng.* **14,** 515–535. ISSN: 0965-0393, 1361-651X (Apr. 2006).

16. Hanfland, M., Beister, H. & Syassen, K. Graphite under Pressure: Equation of State and First-Order Raman Modes. *Phys. Rev. B* **39,** 12598–12603 (June 1989).

17. Parsafar, G. & Mason, E. A. Universal Equation of State for Compressed Solids. *Phys. Rev. B* **49,** 3049–3060 (Feb. 1994).

18. Kobayashi, K., Watanabe, K. & Taniguchi, T. First-Principles Study of Various Hexagonal BN Phases. *J. Phys. Soc. Jpn.* **76,** 104707. ISSN: 0031-9015 (Oct. 2007).

19. Zhao, Y., Dreele, R. B. V., Weidner, D. J. & Schiferl, D. P- V- T Data of Hexagonal Boron Nitride h BN and Determination of Pressure and Temperature Using Thermoelastic

Equations of State of Multiple Phases. *High Press. Res.* **15,** 369–386. ISSN: 0895-7959 (Mar. 1997).

20. Stinton, G. W., Loa, I., Lundegaard, L. F. & McMahon, M. I. The Crystal Structures of δ and δ* Nitrogen. *J. Chem. Phys.* **131,** 104511. ISSN: 0021-9606 (Sept. 2009).

21. Langford, J. I. & Wilson, A. J. C. Scherrer after Sixty Years: A Survey and Some New Results in the Determination of Crystallite Size. *J Appl Cryst* **11,** 102–113. ISSN: 0021-8898 (Apr. 1978).

22. Chen, C. *et al.* Stabilizing the Metastable Superhard Material Wurtzite Boron Nitride by Three-Dimensional Networks of Planar Defects. *Proc Natl Acad Sci USA* **116,** 11181–11186. ISSN: 0027-8424, 1091-6490 (June 2019).

23. Solozhenko, V. L., Häusermann, D., Mezouar, M. & Kunz, M. Equation of State of Wurtzitic Boron Nitride to 66 GPa. *Appl. Phys. Lett.* **72,** 1691–1693. ISSN: 0003-6951, 1077-3118 (Apr. 1998).

24. Knittle, E., Wentzcovitch, R. M., Jeanloz, R. & Cohen, M. L. Experimental and Theoretical Equation of State of Cubic Boron Nitride. *Nature* **337,** 349–352. ISSN: 1476-4687 (Jan. 1989).

25. Goncharov, A. F. *et al.* Thermal Equation of State of Cubic Boron Nitride: Implications for a High-Temperature Pressure Scale. *Phys. Rev. B* **75,** 224114 (June 2007).

26. Chen, X.-Q., Niu, H., Li, D. & Li, Y. Modeling Hardness of Polycrystalline Materials and Bulk Metallic Glasses. *Intermetallics* **19,** 1275–1281. ISSN: 0966-9795 (Sept. 2011).

27. Deura, M., Kutsukake, K., Ohno, Y., Yonenaga, I. & Taniguchi, T. Nanoindentation Measurements of a Highly Oriented Wurtzite-Type Boron Nitride Bulk Crystal. *Jpn. J. Appl. Phys.* **56,** 030301. ISSN: 0021-4922, 1347-4065 (Mar. 2017).

28. Zhang, J. S. *et al.* Elasticity of Cubic Boron Nitride under Ambient Conditions. *Journal of Applied Physics* **109,** 063521. ISSN: 0021-8979 (Mar. 2011).

29. Solozhenko, V. L. & Gregoryanz, E. Synthesis of Superhard Materials. *Materials Today* **8,** 44–51. ISSN: 1369-7021 (Nov. 2005).

30. Teter, D. M. Computational Alchemy: The Search for New Superhard Materials. *MRS Bull.* **23,** 22–27. ISSN: 0883-7694, 1938-1425 (Jan. 1998).

31. Zagorac, D., Zagorac, J., Djukic, M. B., Jordanov, D. & Matović, B. Theoretical Study of AlN Mechanical Behaviour under High Pressure Regime. *Theoretical and Applied Fracture Mechanics* **103,** 102289. ISSN: 0167-8442 (Oct. 2019).

32. Güler, E. & Güler, M. Elastic and Mechanical Properties of Hexagonal Diamond under Pressure. *Appl. Phys. A* **119,** 721–726. ISSN: 1432-0630 (May 2015).

33. Nagakubo, A., Ogi, H., Sumiya, H., Kusakabe, K. & Hirao, M. Elastic Constants of Cubic and Wurtzite Boron Nitrides. *Appl. Phys. Lett.* **102,** 241909. ISSN: 0003-6951 (June 2013).

34. Liu, Y. *et al.* Hardness of Polycrystalline Wurtzite Boron Nitride (wBN) Compacts. *Sci Rep* **9,** 10215. ISSN: 2045-2322 (Dec. 2019).

35. Deura, M., Kutsukake, K., Ohno, Y., Yonenaga, I. & Taniguchi, T. Mechanical Properties of Cubic-BN(111) Bulk Single Crystal Evaluated by Nanoindentation. *Phys. Status Solidi B* **255,** 1700473. ISSN: 1521-3951 (2018).

36. Li, Y., Hao, J., Liu, H., Lu, S. & Tse, J. S. High-Energy Density and Superhard Nitrogen-Rich B-N Compounds. *Phys. Rev. Lett.* **115,** 105502. ISSN: 0031-9007, 1079-7114 (Sept. 2015).

37. Lin, S. *et al.* Prediction of Superhard B_2N_3 with Two-Dimensional Metallicity. *J. Mater. Chem. C* **7,** 4527–4532. ISSN: 2050-7526, 2050-7534 (2019).

38. Xie, C. *et al.* Superhard Three-Dimensional B_3N_4 with Two-Dimensional Metallicity. *J. Mater. Chem. C* **5,** 5897–5901. ISSN: 2050-7526, 2050-7534 (2017).

39. Li, Z. & Gao, F. Structure, Bonding, Vibration and Ideal Strength of Primitive-Centered Tetragonal Boron Nitride. *Phys. Chem. Chem. Phys.* **14,** 869–876. ISSN: 1463-9076, 1463-9084 (2012).

Chapter 4

Vibrational Spectroscopy

4.1 Phonons in hBN and wBN

This chapter details the Raman and infrared spectroscopic studies of BN under high pressure. This section will discuss the phonon normal modes expected in the hBN and wBN structures. The following sections will be split based on the spectroscopic technique employed, i.e. Raman or infrared spectroscopy.

For hBN, the irreducible representation of normal modes gives a total of 12 modes, 3 being acoustic modes (one A_{2u} and a doubly degenerate E_{1u}), 3 infrared active optical modes (again, one A_{2u} and a doubly degenerate E_{1u}), 4 Raman active optical modes (2 doubly degenerate E_{2g}) and 2 inactive modes (both B_{1g})[1]. The calculated phonon frequencies at the Γ point for these normal modes are shown in Table 4.1.

	E_{2g}	B_{1g}	A_{2u}(TO)	A_{2u}(LO)	B_{1g}	E_{2g}	E_{1u}(TO)	E_{1u}(LO)
Phonon frequency (cm^{-1})	50	113	754	823	815	1382	1382	1614
Activity	R	N/A	IR	IR	N/A	R	IR	IR

TABLE 4.1: Calculated central frequency (in relative wavenumbers, cm^{-1}) for optical normal modes of hBN at the Γ point at room conditions[2]. "R" refers to Raman-active modes, "IR" refers to IR-active modes, and "N/A" refers to inactive modes.

For wBN, the phonon normal modes are listed in Table 4.2. The irreducible representation of the normal modes gives 3 acoustic modes (A_1 and E_1), 3 Raman- and infrared-active modes (also A_1 and E_1), 4 Raman-active modes (both E_2), and two silent modes (B_1)[3].

	E_2	E_2	B_1	A_1(TO)	A_1(LO)	E_1(TO)	E_1(LO)	B_1
Phonon frequency (cm^{-1})	475	979	982	1043	1280	1075	1293	1134
Activity	R	R	N/A	IR	IR	Both	Both	N/A

TABLE 4.2: Calculated central frequency (in cm^{-1}) for optical phonon normal modes of wBN at the Γ point at room conditions[2]. "R" refers to Raman-active modes, "IR" refers to IR-active modes, and "N/A" refers to inactive modes.

4.2 Raman Spectroscopy

The Raman spectrum of hBN exhibits two modes of the same symmetry at strikingly different energies. At room conditions, there is an in-plane Raman mode at 1366 cm^{-1} with E_{2g} symmetry, as well as an E_{2g} mode around 55 cm^{-1} related to a shear-type inter-planar mode[4]. This is a closely related with the Raman modes of graphite, which portrays a similar inter-planar shear mode near 42 cm^{-1} and an in-plane vibration around 1582 cm^{-1}, also both of E_{2g} symmetry[5]. Schematics of these phonon modes are shown in Figure 4.1.

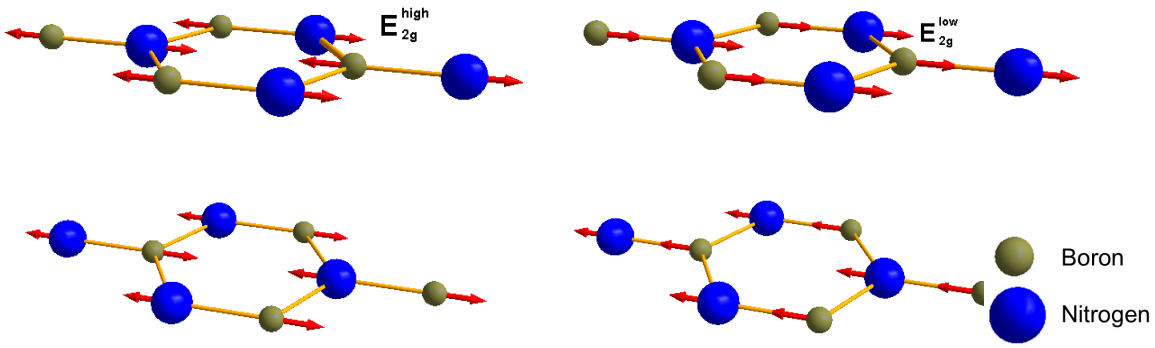

FIGURE 4.1: Schematics of the hBN Raman-active phonon modes.

For all samples, Raman spectra were taken at regular pressure intervals using the setup described in Chapter 2. After reaching their maximum pressure, spectra were taken on the decompression at pressure intervals of about double that of during the compression, barring complications such as diamond breakage. Both E_{2g} modes were tracked along the compression, the central frequency of both modes shifted to higher wavenumbers with increasing pressure, as shown in Figure 4.2 for a powder sample with N_2 used as a PTM. No overtones were observed.

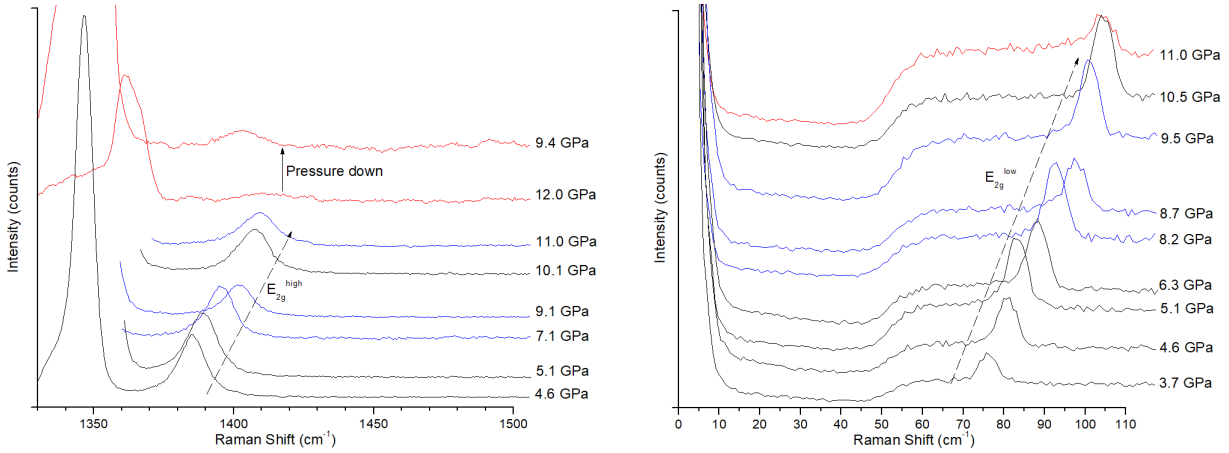

FIGURE 4.2: Raman spectra of hBN powder as they change with applied pressure. Spectra are stacked with a 10% vertical offset. The full structural transition is marked by a change in colour. The diamond T_{2g} Raman line, centered around 1333 cm^{-1} at ambient pressure, are cut from spectra at several pressure steps for clarity purposes. The observed stress shifting of these T_{2g} is due the presence of stressed and unstressed portions of diamond that are being probed, with the T_{2g} Raman mode of the stressed diamond anvil being at a higher frequency.

Raman spectroscopic studies were done on two types of hBN samples, powder and single crystal, both with and without N_2 at the PTM. There were two studies accomplished on single crystal hBN, one with and one without PTM, and five experiments carried out on powder hBN, two with PTM while three were done without. This allowed the systematical determination of whether phase transition characteristics could be related to crystallinity of the starting samples. Inspecting the pressure dependence of the Raman modes communicated by Figure 4.3, the pressure dependence of the frequencies for all samples seems to overlap. It would be safe to posit then that the PTM presence and the order of crystallinity has no major impact on the pressure dependence of Raman mode central frequency.

As shown by Hanfland *et al.*[6], a Murnaghan-type relation can be used to model the pressure dependence of phonon modes, taking the form of

$$\omega(P) = \omega_0[1 + \frac{\delta_0}{\delta'}P]^{\delta'} \tag{4.1}$$

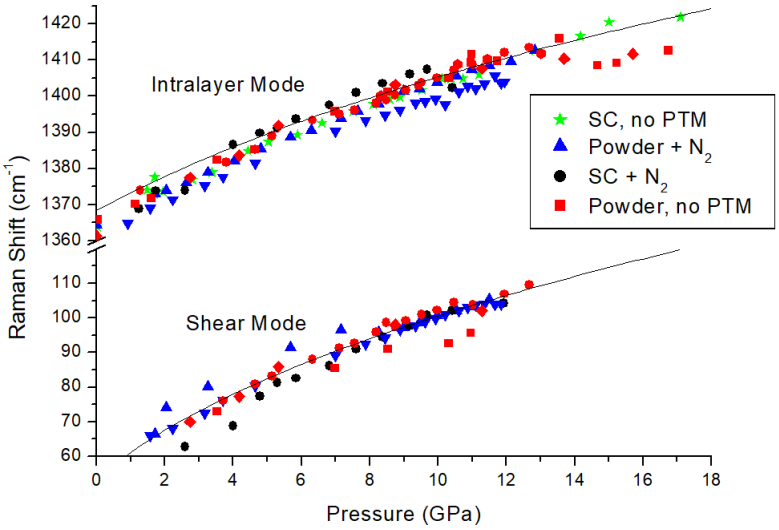

FIGURE 4.3: Pressure dependence of hBN E_{2g} mode wavenumbers. Rotations of the similar symbols indicate different series with the same experimental constraints. The plotted curves are a Murnaghan-type relation for phonon frequencies (eq. 4.1), fit to the respective Raman modes. "SC" refers to single crystal.

where $\omega(P)$ and ω_0 are the central frequencies of a given phonon mode at a pressure P, in GPa, and at room pressure, respectively, δ is the linear pressure derivative of the phonon frequencies at room pressure

$$\delta(P) = \frac{1}{\omega}\frac{d\omega}{dP} \tag{4.2}$$

and $1/\delta'$ is the linear pressure derivative of $1/\delta$, such that

$$\frac{1}{\delta(P)} = \frac{1}{\delta_0} + \frac{1}{\delta'}P \tag{4.3}$$

This model can be used to fit to observed data and retrieve the fitting parameters. These parameters can further be used to define the pressure coefficient at room pressure $\alpha = \delta_0\omega_0$ and the mode Grüneisen parameter $\gamma_G = B_0\delta_0$.

The model is fit to the data with a χ-squared minimization using

$$\chi^2 = \Sigma_i^n(\frac{E_i - O_i}{\sigma_i})^2 \tag{4.4}$$

where $\sigma_i = \frac{FWHM_i}{2.355}$ is the standard deviation of the observed value O_i for the phonon frequency, and E_i is the calculated phonon frequency based on the model using fitting parameters δ and δ'. The value for ω_0 for the E_{2g}^{high} mode is taken as the weighted average of the observed the central frequency at room pressure, using $1/\sigma$ as the weighting factor. Unfortunately, due to E_{2g}^{low} mode being of such low frequency, the spectral line is blocked by the Rayleigh line filter and is hard to discern below 1 GPa. As such, no observation of $\omega_0(E_{2g}^{low})$ is made, so ω_0 is used as a third fitting parameter.

The fitting parameters and related quantities can be found in Table 4.3 compared to those reported in a similar recent study by Cuscó *et al.*[7] Whereas in their study the value of B_0 wasn't calculated and rather quoted from literature for the purposes of calculating γ_G, we have previously measured a value of $B_0 = 30.4 \pm 0.5$ GPa (calculated in Chapter 3); as such, this calculation is likely more representative of our sample. The curves resulting from this model are plotted alongside the observed values in Figure 4.3.

Mode	ω_0 (cm^{-1})	δ_0 (GPa^{-1})	δ'	α ($cm^{-1}GPa^{-1}$)	γ_G	Study
E_{2g}^{high}	136(8)	0.003(6)	0.04(9)	5.(0)	0.1(1)	this study
	1367.3(3)	0.0039(1)	0.061(7)	5.3(2)	0.14(1)	Cuscó *et al.*[7]
E_{2g}^{low}	53.(6)	0.15(8)	0.3(8)	8.(5)	4.8(2)	this study
	52.1(2)	0.151(4)	0.48(1)	7.9(2)	5.5(2)	Cuscó *et al.*[7]

TABLE 4.3: Fitted and calculated vibrational parameters.

Because both observed modes are of the same E_{2g} point group, this can be used to inspect the vibrational anisotropy of the system. Here we will approximate using a simple spring model for binding forces.

The anisotropy in binding force related to interlayer and intralayer phonons can be calculated as

$$\alpha_{ani} = (\frac{\omega_{intra}}{\omega_{inter}})^2 \tag{4.5}$$

Where α_{ani} is the degree of anisotropy, and the ω_{intra} and ω_{inter} are the E_{2g}(high) and E_{2g}(low), respectively. The dependence on pressure of the anisotropy is plotted in Figure

4.4. The result corresponds very well with previous studies done using this model[8].

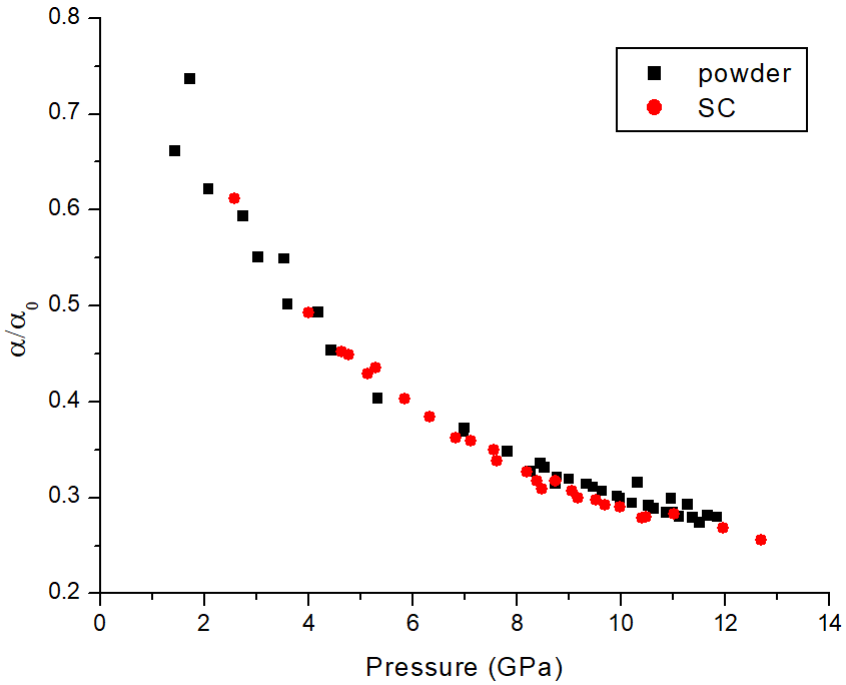

FIGURE 4.4: Normalized degree of anisotropy between hBN E_{2g} modes under increasing pressure. Data points from powder type samples are marked by black squares, whereas single crystal type is marked by red circles.

As shown in Figure 4.4, the anisotropy measured is not different between the two crystalline states, and the trend is continuous until the full transition to wBN around 12 GPa. Because the anisotropy depends on the relation between both E_{2g} modes, it is unfortunately missing above 12 GPa for the extremely non-hydrostatic cases, whose intralayer mode remained present much past the transition region but the low frequency inter-layer mode was lost, most likely into the background.

Near the hBN-wBN phase boundary at 9 GPa, the signal-to-background ratio of the E_{2g} lines becomes increasingly lower, until the lines corresponding to the modes are completely lost; this is likely influenced by a phase transition. The accompanying increase of photo-induced luminescence arising from the sample can be attributed to defects created upon the transition. As observed in the XRD studies, there is once again a region of coexistence of hBN and wBN. No new Raman lines are observed with this transition. For most

samples, the transition to wBN is assumed to be complete above 14 GPa, as no E_{2g}^{low} mode is not observed above 13 GPa for any samples and the E_{2g}^{high} mode is not observed above 13 GPa for any sample loaded with nitrogen; XRD studies showed no sign of hBN above 14 GPa, so the expected complete transition occurs within 1 GPa of the loss of hBN signal in the Raman spectrum. XRD results were shown in Chapter 3.

For the samples loaded without nitrogen as a PTM, while luminescence is observed to grow above the transition pressure, the intralayer E_{2g} mode is still observed up to very high pressures, while the low frequency mode is lost in the luminescent background, if it were to still exist; this could imply the existence of an incomplete transition. Indeed, all the samples did transition into the high pressure wurtzite phase to some degree, as confirmed by XRD of retrieved samples. However, our results in Chapter 3 showed that the transition to wBN is complete above 14 GPa for samples with a PTM, and partially reversible, with all samples partially reverting to hBN upon retrieval at room conditions. As such, we cannot use the relative concentrations of the retrieved samples to infer what the concentrations of any samples would have been at higher pressures. Nonetheless, for these samples that never underwent a full structural transition, we can still assume that the majority of the sample would have been converted considering the large presence of luminescence in their Raman spectra past the transition region and because their wBN recovery yields are close to that of some samples which had fully converted.

This incomplete transition can be related to the lack of hydrostatic conditions within the sample chamber. While non-hydrostatic pressure gradients exist, it is unlikely that these gradients would be large enough to keep some portion of the chamber below 14 GPa. Indeed, this is later confirmed by IR studies using a PTM with known pressure gradients, that the transition is incomplete above 14 GPa for non-hydrostatic conditions. It's likely then that the transition is inhibited by the non-hydrostatic stresses present. In the case of biaxial strain, we would expect to see that the interlayer E_{2g}^{low} mode does not follow the same trend as the intralayer E_{2g}^{high} mode. Unfortunately, as noted, the interlayer

mode could not be observed post transition region pressures.

Upon decompression, the E_{2g} mode is not observed becoming any more defined until under 2 GPa, where it remains still quite weak. This would seem to imply that the high pressure phase of wBN remains strongly metastable until near room pressure. This lack of a full conversion can likely be attributed to the incredibly non-hydrostatic conditions and high order of the crystal.

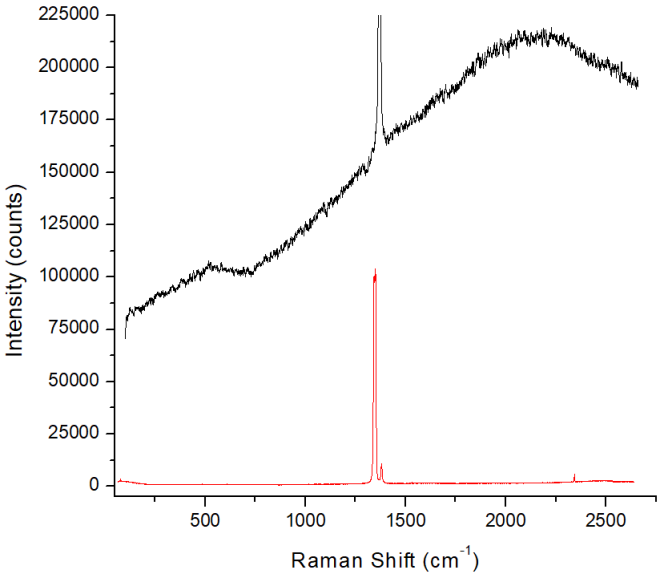

FIGURE 4.5: Extended Raman spectra of an hBN sample at low pressure before and after compression past the phase boundary. The red spectrum (bottom) is of a powdered hBN sample with a nitrogen PTM at 2.4 GPa during the pressure ramp. The diamond T_{2g} Raman line can be found near 1330 cm^{-1}, with the hBN E_{2g} Raman line just to the right at 1330 cm^{-1}. The black line spectrum (top) is of the same material upon decompression to 0.4 GPa from 18 GPa. As can be observed, the background is much more intense compared to the diamond T_{2g} line, which has a markedly lower signal to background ratio here. There is no vertical offset in this figure.

Throughout decompression there was intense luminescence and no observable hBN modes. A comparison of the spectrum before and after the phase transition is shown in Figure 4.5. hBN modes are only again observed once the sample is exposed to ambient conditions and removed from the DAC, marking a large hysteresis to room pressure.

Only the luminescence, and no new Raman lines, was observed across the phase transition above 14 GPa. The Raman modes of wBN are expected to be present though lost in the luminescent background. They have been demonstrated to be near 960 cm^{-1}, 1060 cm^{-1}, and 1310 cm^{-1} by Chen *et al.*[9], with one more Raman mode calculated to be near 475 cm^{-1} from Ohba *et al.*[2]. The luminescence is likely the result of many closely related electronic transitions. Luminescence masking could in principle be avoided by using a laser of shorter or longer excitation wavelengths, shifting the Raman light emission to a different part of the electromagnetic spectrum while having the luminescence remain at the same wavelength.

As demonstrated by Chen *et al.*[9], the Raman modes of wBN are incredibly weak compared to those of hBN, such that resolving them is even a challenge on a recovered sample of wBN of modest size under ambient conditions. Thus, impeded by the microscopic size of our sample, which is located in a DAC resulting in a weaker response, it is deemed challenging that a Raman signal from wBN would ever have been recorded *in-situ* with a satisfactory signal-to-background ratio during our experiment. A recent study by Cuscó *et al.* recently showed the Raman spectrum of wBN from a similar experiment, but only upon retrieval of the sample to room conditions[7].

Interestingly, from samples recovered from the DAC following a high compression above 14 GPa, the intralayer E_{2g} mode is at a lower frequency as compared to the initial value from a fresh sample. Furthermore, this spectral downshift seems to be correlated to the incident power of the laser, which leads to a difference of up to 20 cm^{-1} between the highest and lowest laser powers. This is shown in Figure 4.6, where the frequency of the E_{2g}^{high} mode converges to an accepted value as the power of the laser tends towards zero. We can therefore expect that this is still related to the same hBN mode as before, and attribute the additional shift to the newly introduced structural defects. Later inspection by quantitative XRD confirmed that the yield recovery ratio of wBN to hBN was much higher for samples containing a PTM, but that there is still hBN present in all these samples, as

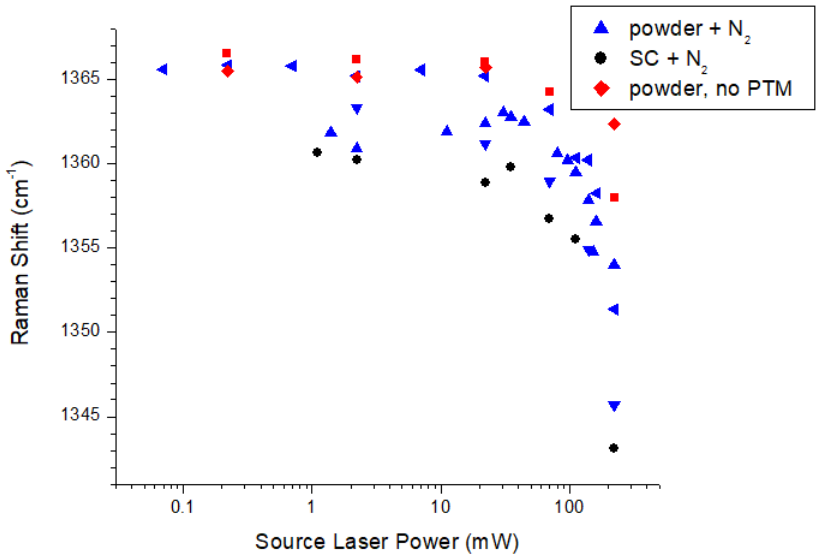

FIGURE 4.6: Raman shift of intralayer E_{2g} mode with relation to incident laser power, as measured at the source, recorded from different powdered and single crystal sample of hBN recovered from high pressure. Different symbols are used for different samples. Rotations of the similar symbols indicate different series with the same experimental constraints. The laser source power is estimated from the laser output (200 mw) and the attenuation provided from calibrated neutral density filters.

discussed in Section 3 of Chapter 3. The structural defects would manifest themselves in the form of colour centers; this is supported by the orange colour the crystal takes on upon re-conversion to hBN in contrast with the white, translucent colour that it has prior to being exposed to these high pressures. The colour centers act to absorb incident photons (at a wavelength of 532 nm) rather than scattering, which leads to an increase of temperature of the sample, and with that an increased volume of spacing of the crystal lattice and a reduction of the phonon mode frequency. This is in contrast with what was reported by Cuscó *et al.*[10], who predicted a frequency increase with temperature.

The important parameters leading to this thermal shift are hard to determine. The characteristic of the laser power dependence such as the high power frequency $\omega_{HP} = \omega(P = 200 \text{ mW})$, low power frequency $\omega_{LP} = \omega(P \to 0 \text{ mW})$, their difference $\Delta\omega = \omega_{LP} - \omega_{HP}$, the difference between these parameters to ω_0, and the slope of this relation

were all recorded and compared to experimental parameters. None of these characteristics showed any trend with any given experimental parameters, such as maximal pressure, wBN/hBN relative yield, crystallinity, PTM presence. The underlying phenomenon occurring most likely requires a more in-depth analysis of the related defects, which unfortunately fell outside the scope of this project.

In Chapter 3, the pressure dependence of the unit cell volume of hBN was effectively modeled with three equations of state (EoSs, the Murnaghan equation among them). In this chapter, the pressure dependence of the Raman mode central frequencies has been modeled. With these two together, devising a relation between the frequency and cell volume should be possible. This could potentially be a way to estimate expansion due to heating.

This relation was explored in two different ways. First, using the Murnaghan equation of state,

$$P = \frac{B_0}{B_0'}[(\frac{V}{V_0})^{-B_0'} - 1] \tag{4.6}$$

the pressure can be calculated based on a given unit cell volume, or vice-versa. For an observed frequency, the unit cell volume can be calculated using the observed pressure in this EoS. A fit could then be performed between the two to model the trend. However, a more physical model is desired. This can be obtained by combining equations 4.6 and 4.1 to produce

$$\omega(\frac{V}{V_0}) = \omega_0[1 + \frac{\delta_0}{\delta'}\frac{B_0}{B_0'}(\frac{V}{V_0})^{B_0'} - 1]]^{\delta'} \tag{4.7}$$

which is now an effective model between the Raman mode frequencies and the unit cell volume. The samples for which we are observing these heating effects in, however, are not pristine. At low laser powers (less than 10 mW), where there is limited laser heating effects, there is already a downshift of the phonon frequencies and an expansion of unit

cell volume, which would incorrectly translate to an effective temperature. To account for this, the low power, room pressure frequency observed for a given material is taken as ω_0, and the calculation is done in terms of the frequency difference $\Delta\omega = \omega_0 - \omega$ rather than in terms of ω.

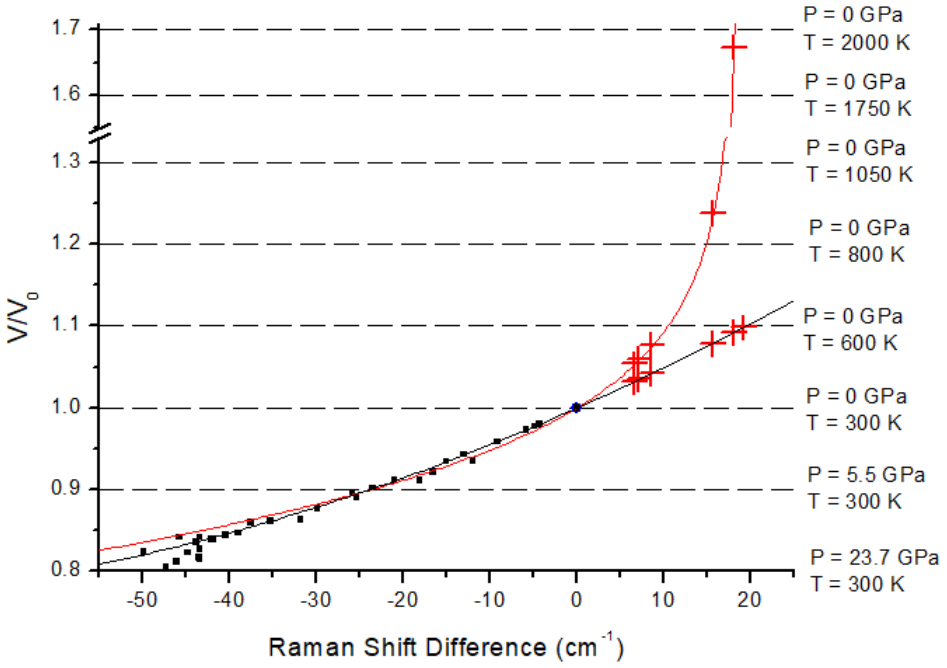

FIGURE 4.7: Estimation of thermal expansion/static compression based related to difference in frequency. The black points are from static compression at room temperature, where V/V_0 is calculated based on eq. 4.6. These points are extrapolated with a quadratic fit to form the black line. Equation 4.7 forms the red line. Red crosses are placed along both lines to show the observed thermal measurements based on both models.

Plotted alongside each other in Figure 4.7, there is an obvious divergence between both estimates of thermal expansion. The polynomial fit estimates that the thermal expansion lies below $V/V_0 = 1.1$ for any observation, relating to a temperature of less than 600 K based on previous reports[11]. Meanwhile, equation 4.7 diverges asymptotically around a frequency difference of 20 cm^{-1}, which is just above the highest observation, leading to an estimated expansion upwards of $V/V_0 = 1.7$, or 2000 K. This is quite a bit higher than we would believe reasonable. A comprehensive model would consider the effect of temperature on the present parameters as well, such as B_0 and δ_0. Attempts to make

this consideration for $B_0(T)$ based on Solozhenko's work[11] led to even higher, less realistic values of temperature (up to 8500 K). While there is potential to use this model for thermal measurements, it would be necessary to first perform similar Raman experiments under a range of temperatures before this model, let alone the estimated temperatures, can be considered genuine.

While there still exists many outstanding questions from the Raman spectroscopy experiments, there has also been plenty answered. The observed E_{2g} mode parameters correlate well with those previously reported in literature, and there is good correlation of measured parameters between all sample configurations attempted. The underlying dynamics of the recovered, defective hBN remain uncertain, and subject for a compelling future investigation.

4.3 Infrared Spectroscopy

4.3.1 IR-Active Vibrational Modes of hBN

Similar to the E_{2g} Raman modes, the IR active modes of hBN consist of a low frequency out-of-plane A_{2u} mode and a high frequency in-plane E_{1u} mode, represented by Figure 4.8. Both these modes have been observed to possess LO-TO splitting, though reports on the A_{2u}(TO) are rare[12,13]

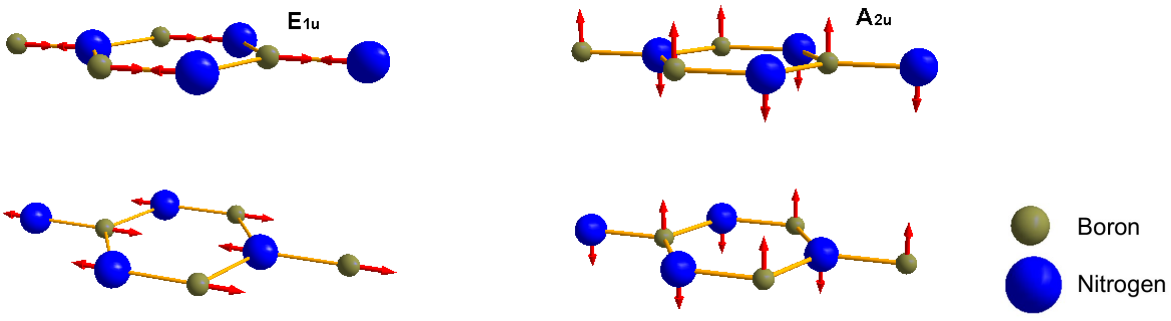

FIGURE 4.8: Schematics of the hBN IR-active phonon modes.

LO-TO splitting is much less for polycrystalline samples, leading to unsplit or unresolvably small split for the A_{2u} at 811 cm^{-1} and a split for E_{1u}, which has a TO mode at 1377 cm^{-1} with weak LO mode at 1514 cm^{-1}[14]. Considering we don't see the split A_{2u} mode, and the LO of E_{1u} is much weaker than the TO, it is likely our crystalline samples are ordered hBN flakes, but necessarily polycrystalline.

The refined band breakdown of the hBN IR absorption spectrum provided many challenges. While the IR spectrum of bulk hexagonal and nanostructured BN has been reported in several studies, to our knowledge only few exist on hBN at high pressures; those studies that do exist presented either saturation for the E_{1u} band[13], or lower resolution[12]. As such, some of the finer structures of the spectra are missing from high pressure analyses.

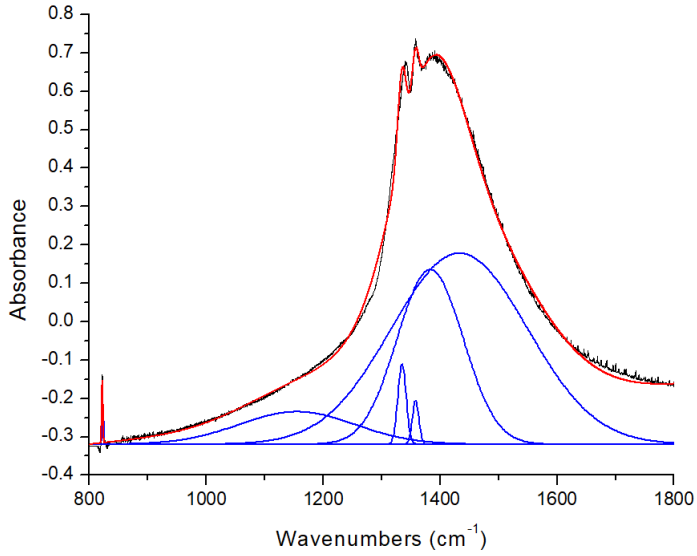

FIGURE 4.9: Deconvolution and fitting of the IR absorption spectrum of an hBN sample at 0.36 GPa. An R^2 value of 0.998 was achieved for the fit.

In the current study, no LO-TO splitting is observed for the A_{2u} mode; this is consistent with studies that have shown that smaller samples exhibit less LO-TO splitting[14]. This means that the band near 830 cm^{-1} can just be labeled as A_{2u}. Zhi *et al.* reported a visible shoulder on the low wavenumber side of the broad band for BN nanotubes[15], which we believe to observe; the origins of this peak are unfortunately still unclear. Most IR

studies on BN materials assign the remaining broad band around 1370 cm^{-1} to be the E_{1u} (TO) mode, with a broad, weak shoulder at higher wavenumbers as the E_{1u} (LO) mode. However, this model overlooked some of the finer features of the band.

Visible in Figure 4.9 are two sharp features that break out from the broader band, at 1335 and 1358 cm^{-1}, respectively. These features are referred to as "fingers" within the confines of this research (due to their reminiscence to the foam fingers that are/were often seen at sports exhibitions). These fingers were initially thought to be artifacts caused by Fabry-Perot type interference due to the cavity formed by the diamond anvil surfaces. Once an effective method for filtering was developed, these features remained; they were then ascribed to being artifacts resulting either from Fourier filter "ringing", as often observed near the frequency of the A_{2u} peak, or from insufficient filter effectiveness. However, the bandwidth of these features are observed to be independent of the period of the interference fringes. Furthermore, similar features have been shown in nanostructured hBN spectra outside of a DAC, where there wouldn't be any Fabry-Perot effects, though they have either been labeled as E_{1u}(TO) modes or otherwise undetermined[14–16]. Furthermore, in any of these studies only one such feature is observed, never two. Whether or not one of these fingers is truly the E_{1u} (TO) mode, the other finger is a new observation.

Fourier self-deconvolution[17] was considered to elucidate the central frequencies of each feature in this band. The main requirements for a successful and meaningful deconvolution with this method is that the bands be all of similar widths (which they are not), and that the S/N be no less than 100, preferably above 1000; because of strong IR absorption introduced by atmospheric moisture, the S/N is at worst 20 for some spectra and only around 100 at best. This type of deconvolution was attempted nonetheless and, as expected, returned only meaningless results. The method was thus not pursued.

Peak fittings were performed based on a band model which includes 6 peaks: the low A_{2u} mode near 830 cm^{-1}; a weak shoulder to the broad band, near 1250 cm^{-1}; the two sharp fingers observed around 1330 and 1360 cm^{-1}; a broad, intense line central to the

band around 1370 cm^{-1}, which has classically been assigned to the E_{1u} (TO) mode; a high wavenumber shoulder to the broad band around 1600 cm^{-1}, classically assigned to the E_{1u} (LO) mode. This fitting was done using the Matlab curve fitting toolbox[18] for selected spectra, with each peak being Gaussian profiles with central frequency bounds set to be within twice the expected bandwidth. The other parameters were adjusted to produce a fit that well represented the features of interest and provided an R-squared result of no less than 0.998. In the interest of time, deconvolution of remaining spectra was performed using XRDA[19].

With these fits, the convoluted line profiles were estimated. For the near-ambient pressure (0.36 GPa) spectrum shown in Figure 4.9, the fingers were found to have central frequencies of 1335 and 1358 cm^{-1}, with FWHM of 10 and 8 cm^{-1}, respectively. One of the main objectives of this part of the project was elucidating the reason for the difference in band profiles between the A_{2u} mode and the E_{1u} mode. Should these fingers truly be the manifestations of the E_{1u} mode, then the difference in intensity and bandwidth isn't quite as marked as earlier thought. Comparing values for $\frac{\nu}{FWHM} \times 100\%$ both the values for the A_{2u} mode is 0.18%, while the fingers have values of 0.75% and 0.59%, whereas all the other peaks are much more than one percent. While this normalized width for A_{2u} is still a fraction of that for the E_{1u} fingers, it is much more comparable. Furthermore, because the E_{1u} mode is an intralayer vibration, it is likely to be much more sensitive to defects than the interlayer A_{2u} mode, leading to more broadening. Additionally, the intensity of the A_{2u} mode is between the values for intensity of respective fingers.

Interestingly, upon turning the sample about the probing axis, a change is observed in the large band profile. This change is caused by an increase by around 50% in the intensity of the lower wavenumber finger, while the other features remain more or less the same. This was initially interpreted as a third finger resulting from the turn, and much of the analysis has been done considering such a model, but as shown in Figure 4.10, a model with 2 fingers is sufficient to fit the band with a high degree of confidence. The higher

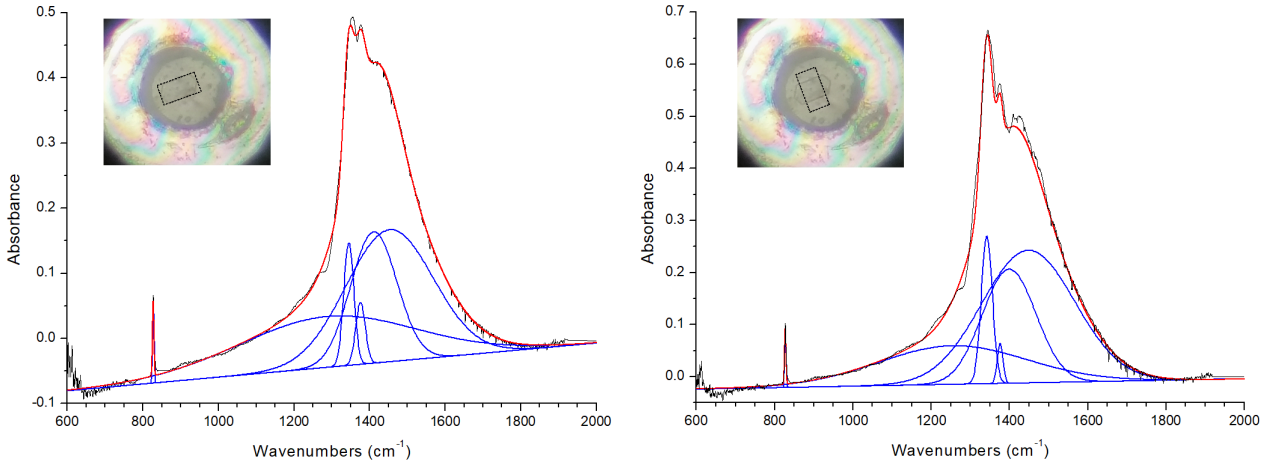

(A) Aligned. (B) Turned.

FIGURE 4.10: Spectral fitting of IR absorption spectra from a sample of hBN at 5.18 GPa, for 90^o rotations between them. The recorded spectra are drawn in black, with the band breakdown in blue and fitted equation shown in red. the inset shows an image of the sample, with the respective orientation of the IR aperture overlaid. The cumulative R^2>0.999 for both fits.

wavenumber mode demonstrates a pressure coefficient similar to that calculated for E_{1u} (TO)[13], with a value of 4.3 cm^{-1}/GPa compared to the calculated value of 4.1 cm^{-1}/GPa. This would lead us to believe that the higher wavenumber finger is the E_{1u} (TO) mode, while the turn-dependent finger is possibly something else entirely.

Above 9 GPa, a transition is observed with many marked differences to the spectrum. Several new peaks appear in the span between the two bands in phase *I* (hBN), and with increasing pressure the original bands weaken in intensity. Interestingly, while the sharper yet weaker A_{2u} band disappears well before the full transition at 14 GPa, the broad intense band associated with the E_{1u} continues to weaken across the transition and is still present, though quite weak, even at incredibly high pressures. This corresponds with reports of the E_{1u} mode persisting to pressures of 23 GPa[12]. Considering that partial conversion to wBN is observed by Raman spectroscopy only in samples loaded without a PTM, the transition could be inhibited by non-hydrostatic stresses, because KBr has been shown to be an imperfect PTM[20]. While XRD was performed on samples with a similar quality PTM in Chapter 5, these were only brought up to a maximum pressure of 12 GPa, so an

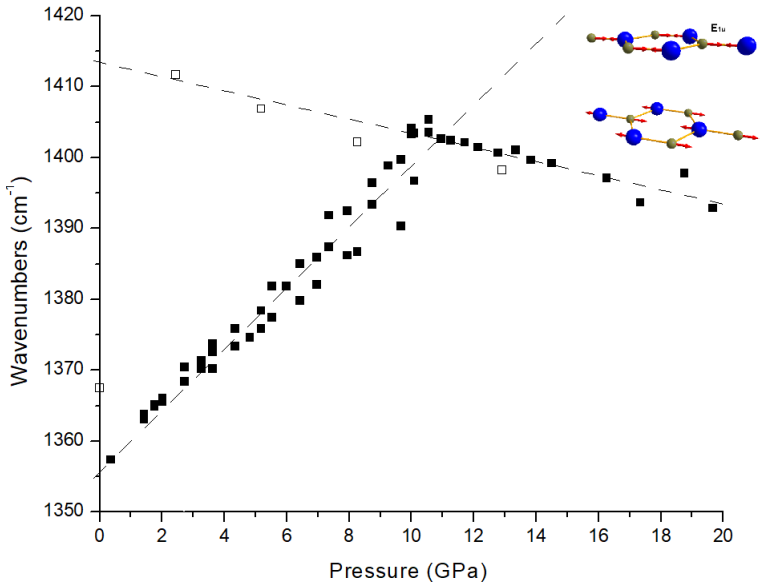

FIGURE 4.11: Central frequency of E_{1u} mode with pressure. Linear fits are displayed for the data before and after transition to the wBN phase. Empty points represent values measured upon decompression.

incomplete transition could not be confirmed.

While this large band persists to high pressures, only one of the fingers persists, the one without a turn-dependence; though it is only observed in the spectrum for turned samples above 10 GPa. Across the phase boundary, this mode develops a negative dependence on pressure, which is maintained upon decompression, as shown in Figure 4.11. This makes sense should this mode be the E_{1u}, which is a vibration in the a-direction, as the a-parameter increases in the transition to wBN. This increase in the a-parameter isn't manifested in the hBN structure as detected by XRD (Chapter 3), however , and this type of deformation still doesn't explain the increasing frequency upon decompression. XRD analysis of an hBN sample with a similar PTM across the phase boundary pressures is necessary to elucidate the relation between this mode softening and the a-parameter. It may be that above the line being observed with a negative pressure coefficient is a different mode entirely, one related to wBN; however, this wouldn't explain why the intensity decreases with increasing pressure, nor aids in identifying the mode, as no phonon mode is predicted with such a high frequency and such a narrow distribution isn't expected for

any 2-phonon processes.

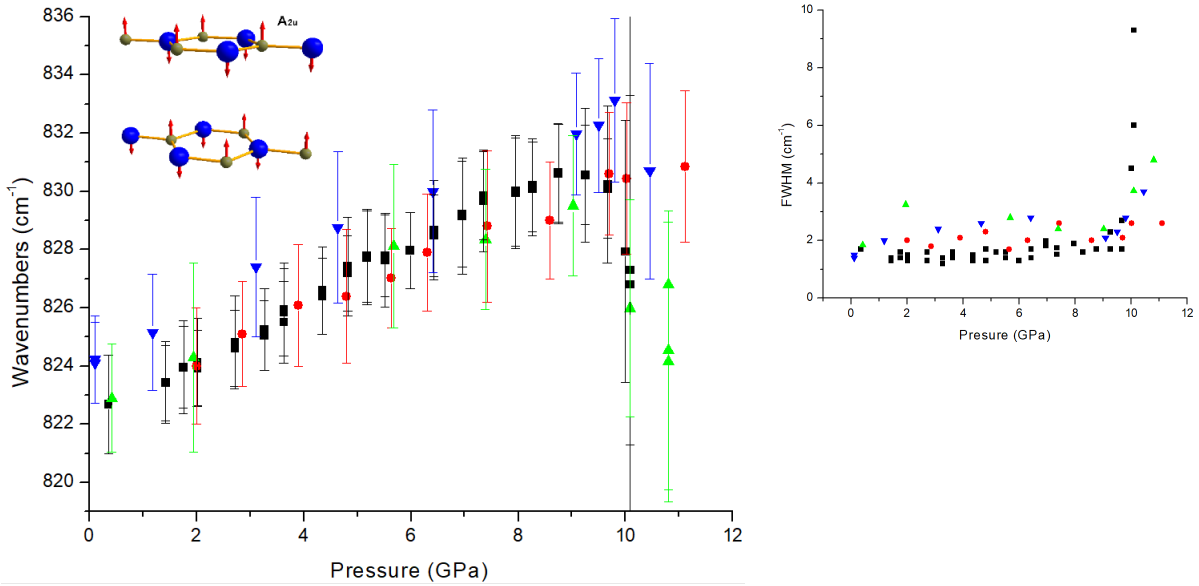

FIGURE 4.12: Central frequency of A_{2u} mode with pressure. Vertical bars indicate the standard deviation of the Gaussian fit. Data from different series are defined with different colour and symbols.

The pressure dependence of the A_{2u} mode is plotted for several sample series in Figure 4.12. Up to the transition, a similar progression is shown for each sample, with pressure coefficients ranging from 0.78 to 1 cm^{-1}/GPa (corresponding well to previous calculations predicting a value of 0.88 cm^{-1}/GPa for the A_{2u} (LO)[13]). Measurement of the A_{2u} under a pressure ramp by FTIR reflectance and absorption methods was used to reaffirm correspondence between the two. The sample was then left just below transition pressure and taken to the Canadian Light Source Mid-IR 01B1-1 beamline. Spectroscopy was then performed during a decompression and secondary compression ramp on the sample. For both cases, the difference between values measured with each method is much less than the resolution at of 4 cm^{-1} at 4000 cm^{-1}.

Above 9 GPa, the peak width of the A_{2u} mode increases, while the intensity and central frequency rapidly decrease, as shown in Figure 4.12. Because this occurs at the same pressure that new peaks related to the wBN phase appear, this effect is attributed to the phase transition. This effect is consistent whether the A_{2u} band fitting takes into account LO-TO

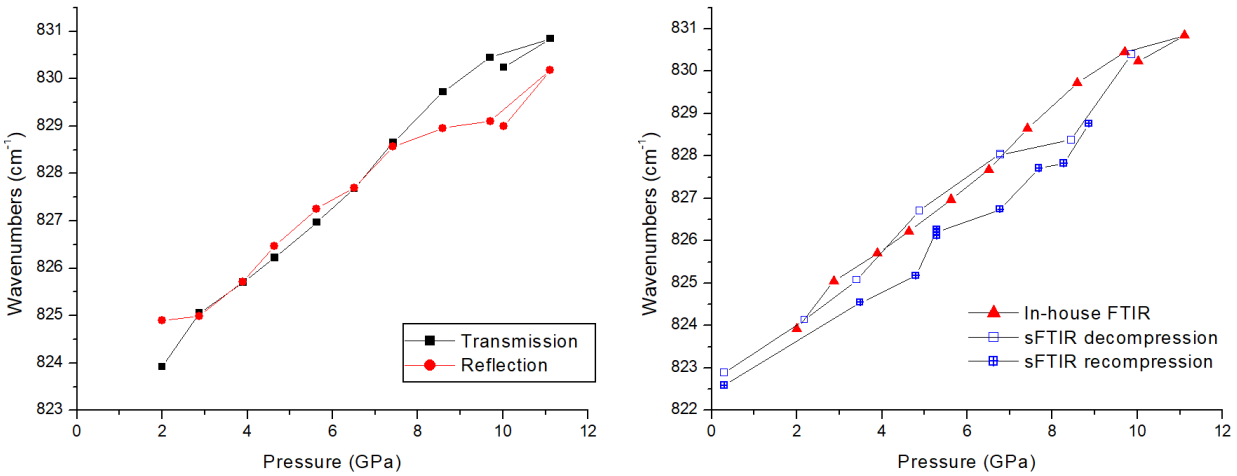

FIGURE 4.13: Pressure dependence of the hBN A_{2u} mode using difference techniques and sources. Linking lines are added to guide the eyes. The accuracy of the measurements are within 1 cm^{-1}.

splitting or not (whether the fit has two profiles or one). While softening under pressure has been observed for the A_{2u} (TO) mode, this effect is a linear effect beginning at room pressure, and no softening is expected nor observed for the LO mode[13]. Further, this softening of the A_{2u} band is not consistent between sample series. The degree to which this softening occurs is proportional to the depth of the sample chamber (unfortunately, the crystallite size was not measured in these experiments), with the smallest sample chamber producing little to no softening above 9 GPa. This shift is independent of the sample pressure coefficient.

4.3.2 IR Modes of wBN

Along with changes in the hBN phonon modes, the transition at 9 GPa is characterized by the appearance of new spectral features, as shown in Figure 4.15. These new features are expected to be related to the phonon modes of wBN. At 9.3 GPa, there are sharp features at 870 and 995 cm^{-1}, and two broader weak peaks at 1040 and 1092 cm^{-1}. There additionally seems to be a large background above 700 cm^{-1} to somewhere near the hBN E_{1u} band,

which indicates one or more additional peaks that are masked by convolution with these modes.

FIGURE 4.14: Schematics of the wBN IR-active phonon modes.

Two phonon modes are expected in wBN, with A_1 and E_1 symmetry like in Figure 4.14, and each with LO-TO splitting for a total of four expected modes. The peak found at 1092 cm^{-1} lays right between the predicted value for the A_1 (TO) and E_1 (TO) modes by density functional perturbation theory[21]. Previous studies of wBN have not been able to deconvolve the two modes either[12,21] and have assumed the band to be formed of equal contributions of both. However, the sharpness and lack of any shoulder to the peaks may imply it's just one. Because the sample is oriented such that the IR radiation probes through the c-direction, electric field oscillations would be in the a-direction and couple better with the a-direction E_1 vibrations. This may results in negligible contributions to the band from the A_1.

The case is similar for the A_1 and E_1 (LO) modes. Though they not shown in Figure 4.15 due to convolution with the intense hBN E_{1u} band at lower pressures, the mode observed that is attributed to the A_1 and E_1 (LO) modes is incredibly sharp and lies right between the expected value for both modes, as shown in Figure 4.16. Because of the incredible sharpness of the mode, it is a safe assumption that it is only one mode there; this is likely the E_1 (LO) mode, using the same logic applied to the TO modes.

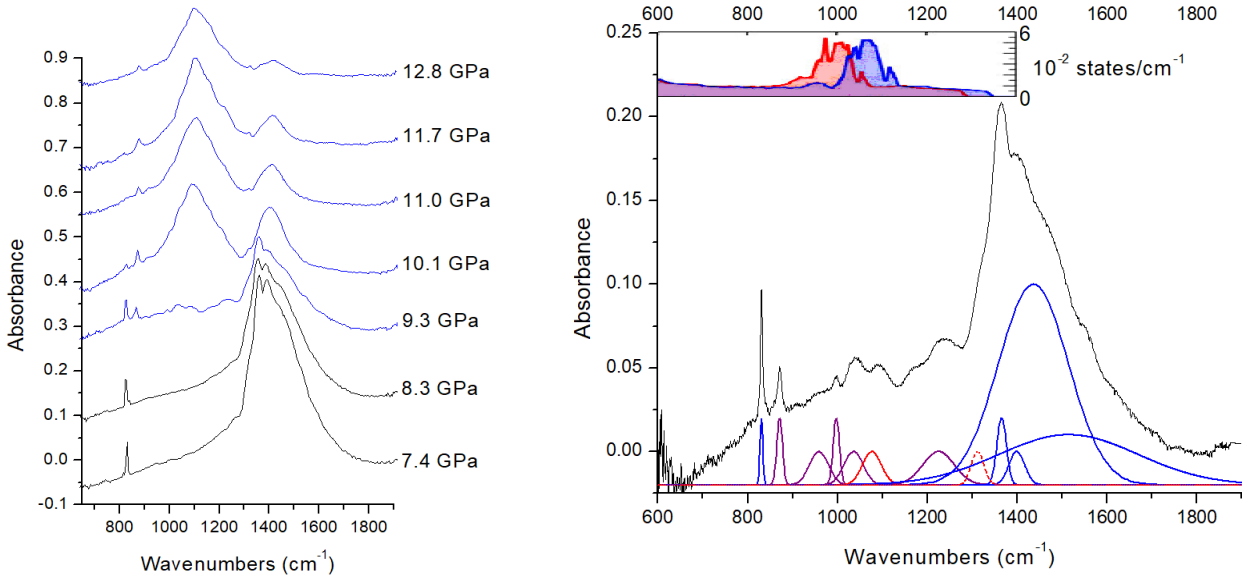

FIGURE 4.15: IR absorption spectroscopy of the hBN-wBN phase transition. The waterfall plot (left) displays a series of IR absorption spectra before and after the phase transition in near 1 GPa steps. Spectra containing only hBN are shown in black, spectra with coexistence of hBN and wBN shown in blue. A vertical offset is added for clarity. The figure on the right displays a deconvolution of the spectrum at 9.3 GPa. Fit curves are displayed in blue for normal modes of hBN, red for optically-active normal modes of wBN, and purple for defect-activated modes of wBN. The expected curve for the A_1/E_1 (LO) of wBN is plotted with a dotted line. The inset shows the phonon density of states for wBN at ambient pressure in red, for 20 GPa in blue, and is adapted with permission from Segura *et al.* 2019. Copyright 2019 American Chemical Society.[21].

The remainder of the new modes in Figure 4.15 are not predicted IR-active modes of hBN, nor of wBN. Of these new features, only the sharp one at 870 cm^{-1} have been observed before, begin attributed to either the Raman-active E_2 mode[12], or because of a large peak in the phonon density of states (PDOS)[21], in both cases the mode becomes IR-active due to the wBN being highly defective around the transition. Because the observed peak at 9.3 GPa is much lower frequency than the one in the PDOS (even at ambient pressure), it is more likely that this mode is due to the activation of the wBN E_2 mode; however, the pressure coefficient of this mode is calculated to be around 2 cm^{-1}/GPa, almost half the 3.5 cm^{-1}/GPa that was previously calculated[21]. Though it does weaken at high pressures, the mode is still observed up to 20 GPa and throughout the decompression, as shown in Figure 4.17a. The other additional peaks can be described by the shape of the PDOS at

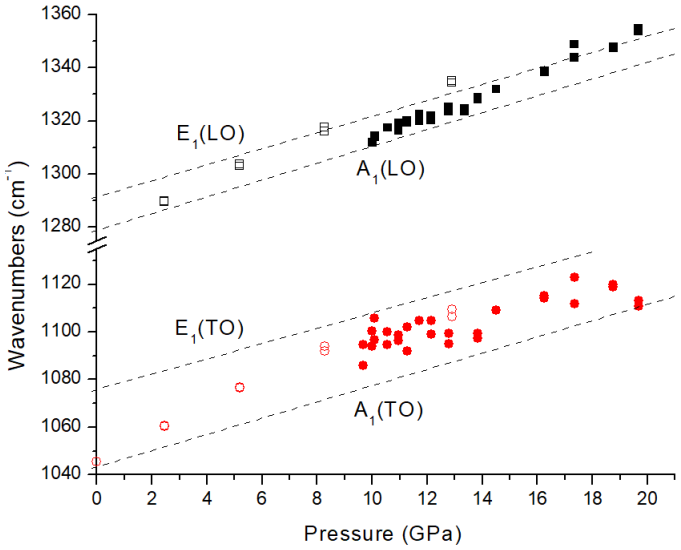

FIGURE 4.16: Pressure dependence of the LO/TO bands of the wBN normal modes. Empty symbol note the values measured on decompression. The lines indicate the lines progression predicted by density functional calculations by Segura *et al.*[21].

those energies. The peaks at 995 and 1092 cm^{-1} both respectively lie between where corresponding peaks in the PDOS are at 0 and 20 GPa; because this measurement is done at 9.3 GPa and often phonon modes have a nearly linear pressure dependence, it is expected that they would be halfway. Furthermore, the additional background that is observed below 1400 cm^{-1} is also expected with more phonons far from the Γ-point become IR-active.

Unfortunately, most of these novel spectral features could not be clearly observed at higher pressures due to convolution with the wBN A_1/E_1 TO band. The sharp feature at 870 cm^{-1} was still observable to higher pressures. This mode decreases in intensity with pressure and the growing intensity of the IR-active wBN modes, reassuring that this is a defect-activated mode.

A mode with a negative pressure dependence is observed between 9-14.5 GPa, shown in Figure 4.17b with the finger mode that showed negative pressure dependence. Unlike the finger mode, this new mode is broad, has a large pressure dependence close to 8 cm^{-1}/GPa, and is short-lived, disappearing above 14.5 GPa and not reappearing upon decompression.

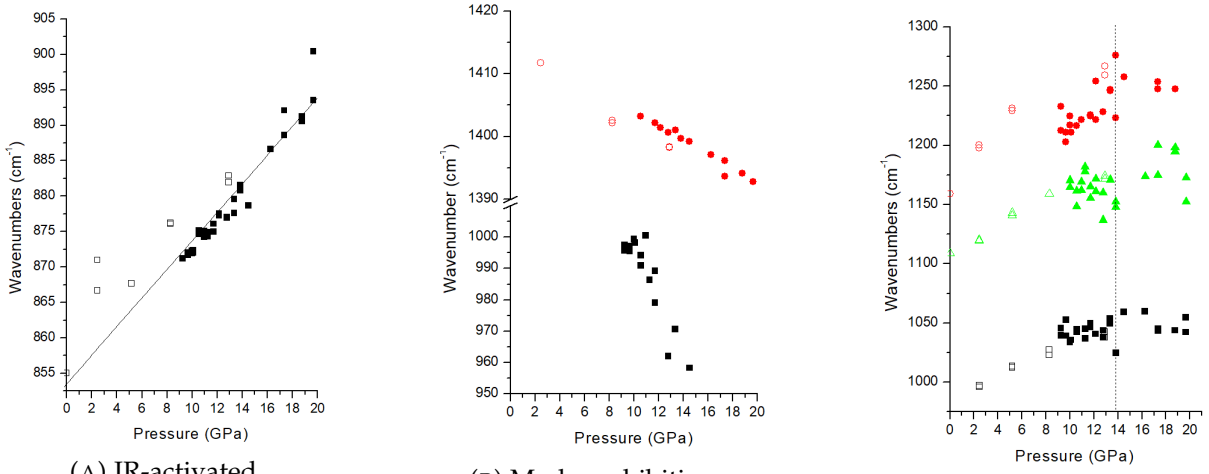

(A) IR-activated wBN E_2 mode.

(B) Modes exhibiting a negative pressure coefficient.

(C) Additional modes.

FIGURE 4.17: Pressure dependence of anomalous and defect-activated modes after wBN transition. Empty symbols are values recorded on decompression. The higher frequency mode with negative pressure dependence, describe with the red circles in Figure 4.17b, is the same mode that has been related to the E_{1u} mode shown in Figure 4.11.

The remaining new modes display a positive pressure dependence to 14.5 GPa. As shown in Figure 4.17c, the pressure dependence of these modes plateaus above 14.5 GPa. Interestingly, upon decompression, these modes regain their original pressure dependence, unlike the finger mode which retains its negative pressure dependence throughout the decompression. While this is certainly a shocking result, the prior mentioned fact that these modes are so heavily convoluted casts a shadow of uncertainty over any insight these modes may give. Nonetheless, this change in pressure dependence could be explained by a slight structural modification. For wBN under bi-axial compression, sheer stresses leading to a bond flippage was predicted by Pan *et al.*[22] to lead to a stronger material. This structural modification was predicted to cause no change in wBN volume, making it consistent with our XRD results. Such a structural modification may be possible at high pressures, possibly with the pressure gradients imposed by a KBr PTM. It's interesting that this phenomenon is not shown at all in the expected A_1/E_1 LO or TO

modes, but the reversibility of the pressure dependence of the modes in Figure 4.17c signals that such a transition may be reversible. The fact that many of these defect-activated modes exist at all corroborates the predictions of wBN being stabilized by the presence of defects[9].

Whether the effects of these defects is consistent across the many experimental series remains to be seen and should provide explanations or improve confidence for many of the new results. It is interesting that our results differ so greatly with those from Segura et al.[21]. The lack of novel defect modes in Segura's report is possibly due to a lack of filtering the interference, leading to a different model for present modes being applied to our respective spectra. They also report a complete, irreversible transition to wBN by 20.5 GPa, whereas our reports show all samples are partially reversible, even if taken to higher pressures. It could be that these effects are sample-dependent, in which case more experiments are necessary.

4.4 Summary

Raman spectroscopy was performed on several configurations of powder and single crystal hBN samples with and without a PTM at high pressures, while IR spectroscopy was performed almost exclusively on single crystal hBN in KBr. Both E_{2g} Raman modes of hBN were observed and tracked to high pressure, and their pressure dependent parameters were in good agreement with prior reports. No correlation could be drawn between the type of sample configuration and pressure dependence of the modes, mode anisotropy, or observed defective properties of recovered sample. The phase transition to wBN produced a large luminescence background such that the Raman modes of wBN were not observable, even for the recovered samples. The hBN E_{2g}^{high} mode was observed above 14 GPa, but only for samples loaded without a PTM. Thus, it is likely that pressure gradients inhibit the transition to wBN; this is corroborated by the incomplete transitions

observed in IR spectroscopy, where a KBr PTM was used, providing small but substantial pressure gradients.

Recovered hBN was defective, gaining a yellow-orange tint as observed by optical microscopy. A softening of the frequency of the E_{2g}^{high} mode is observed in recovered hBN, which is highly power dependent. This is attributed to heating effects due to the hBN defects coupling with the laser. A model was developed to attempt to describe the temperature based on the shift of the E_{2g} and previously determined parameters; the model diverges near the maximal shift observed, and is therefore expected to be greatly overestimating the temperature. Raman spectroscopy on these samples under variable temperatures, better yet variable pressures and temperatures, could elucidate the accuracy and oversights with the model, such as the temperature dependence of the vibrational pressure coefficients.

Infrared absorption spectroscopy of hBN proved to be nontrivial. Because appropriate filtering methods, to remove interference features due to the Fabry-Perot cavity, weren't developed until later into the project, finer features of the spectra were obfuscated by periodic interference. Until then, many spectral features were overlooked, attributed to artifacts, and an incomplete model for the spectral bands was applied. Nonetheless, a complete model was eventually developed, providing a good fit to the IR absorption spectra. Two sharp features of the hBN E_{1u} band were fitted to have similar profiles to the A_{2u} mode. One was therefore considered to be the E_{1u} (TO); the other showed a strong dependence on the sample orientation. Above 10 GPa, the mode attribute to E_{1u} (TO) developed a negative pressure dependence, which it retained throughout the decompression. This was attributed to the increase of planar bond length about the transition to wBN. A more rapid softening, coupled with broadening, is also observed for the A_{2u} mode around the same pressure. Interestingly, the degree to which this softening occurs shows a correlation to the depth of the cell.

Many new IR modes were observed upon the transition to wBN. While there are 4 IR-active modes expected for wBN, LO and TO modes of both A_1 and E_1 modes, only 2 are observed in the predicted regions. Previously this has been attributed to convolution of the A_1 and E_1 modes, where both their LO and TO counterparts are respectively predicted; however, no indication of any sort of convolution is observed. In fact, the sharp feature observed where the LO modes are predicted makes convolution doubtful. This would imply that one mode is contributing much more. We propose this mode is the E_1 mode, which has a vibration parallel with the IR beam electric field. The other modes are attributed to other defect-activated modes, only one of which has been reported previously. The other modes showed interesting dependence on pressure, 3 of which developing a reversible change in pressure dependence above 14.5 GPa to a minimal value. This may be related to the structural modification predicted by Pan *et al.*[22] for wBN under bi-axial compression and sheer stress.

Many of the outstanding questions relating to the IR spectra may be solved by thorough analysis of outstanding IR spectra using a more rigorous fitting to the newly developed spectral model. Bridging the gap between IR and Raman experiments, it would be interesting to see what type of correlation the defect hBN E_{2g} mode has with the intensity of defect-activated IR bands in the sample. Vibrational spectroscopy at low temperature conditions may help to improve understanding of the intrinsic IR spectrum of wBN, greatly reducing defect-activated modes and 2-phonon bands, while also providing insight into the temperature dependent model developed based on the Raman E_{2g} mode.

Bibliography

1. Geick, R., Perry, C. H. & Rupprecht, G. Normal Modes in Hexagonal Boron Nitride. *Phys. Rev.* **146,** 543–547. ISSN: 0031-899X (June 1966).

2. Ohba, N., Miwa, K., Nagasako, N. & Fukumoto, A. First-Principles Study on Structural, Dielectric, and Dynamical Properties for Three BN Polytypes. *Phys. Rev. B* **63,** 115207. ISSN: 0163-1829, 1095-3795 (Mar. 2001).

3. Gil, B. in *Physics of Wurtzite Nitrides and Oxides: Passport to Devices* 65–129 (Springer International Publishing, Cham, 2014). ISBN: 978-3-319-06805-3.

4. Kuzuba, T., Era, K., Ishii, T. & Sato, T. A Low Frequency Raman-Active Vibrations of Hexagonal Boron Nitride, 3 (1978).

5. Reich, S. & Thomsen, C. Raman Spectroscopy of Graphite. *Philosophical Transactions of the Royal Society of London. Series A: Mathematical, Physical and Engineering Sciences* **362** (eds Ferrari, A. & Robertson, J.) 2271–2288. ISSN: 1364-503X, 1471-2962 (Nov. 2004).

6. Hanfland, M., Beister, H. & Syassen, K. Graphite under Pressure: Equation of State and First-Order Raman Modes. *Phys. Rev. B* **39,** 12598–12603 (June 1989).

7. Cuscó, R. *et al.* Pressure Dependence of the Interlayer and Intralayer E_{2g} Raman-Active Modes of Hexagonal BN up to the Wurtzite Phase Transition. *Phys. Rev. B* **102,** 075206 (Aug. 2020).

8. Kuzuba, T., Sato, Y., Yamaoka, S. & Era, K. Raman-Scattering Study of High-Pressure Effects on the Anisotropy of Force Constants of Hexagonal Boron Nitride. *Phys. Rev. B* **18,** 4440–4443. ISSN: 0163-1829 (Oct. 1978).

9. Chen, C. *et al.* Stabilizing the Metastable Superhard Material Wurtzite Boron Nitride by Three-Dimensional Networks of Planar Defects. *Proc Natl Acad Sci USA* **116,** 11181–11186. ISSN: 0027-8424, 1091-6490 (June 2019).

10. Cuscó, R., Gil, B., Cassabois, G. & Artús, L. Temperature Dependence of Raman-Active Phonons and Anharmonic Interactions in Layered Hexagonal BN. *Phys. Rev. B* **94,** 155435. ISSN: 2469-9950, 2469-9969 (Oct. 2016).

11. Solozhenko, V. L. & Peun, T. Compression and Thermal Expansion of Hexagonal Graphite-like Boron Nitride up to 7 GPa and 1800 K. *J. Phys. Chem. Solids* **58,** 1321–1323. ISSN: 0022-3697 (Sept. 1997).

12. Dong, Z. & Song, Y. Transformations of Cold-Compressed Multiwalled Boron Nitride Nanotubes Probed by Infrared Spectroscopy. *J. Phys. Chem. C* **114,** 1782–1788. ISSN: 1932-7447, 1932-7455 (Feb. 2010).

13. Segura, A. *et al.* High-Pressure Softening of the Out-of-Plane A_{2u} (Transverse-Optic) Mode of Hexagonal Boron Nitride Induced by Dynamical Buckling. *J. Phys. Chem. C* **123,** 17491–17497. ISSN: 1932-7447, 1932-7455 (July 2019).

14. Borowiak-Palen, E. *et al.* Infrared Response of Multiwalled Boron Nitride Nanotubes. *Chem. Commun.*, 82–83. ISSN: 13597345, 1364548X (Dec. 2003).

15. Zhi, C. *et al.* Phonon Characteristics and Cathodolumininescence of Boron Nitride Nanotubes. *Appl. Phys. Lett.* **86,** 213110. ISSN: 0003-6951, 1077-3118 (May 2005).

16. Zhong, B. *et al.* Preparation and Ultraviolet-Visible Luminescence Property of Novel BN Whiskers with a Cap-Stacked Structure. *J. Phys. Chem. C* **114,** 21165–21172. ISSN: 1932-7447 (Dec. 2010).

17. Tooke, P. B. Fourier Self-Deconvolution in IR Spectroscopy. *TrAC Trends in Analytical Chemistry* **7,** 130–136. ISSN: 0165-9936 (Apr. 1988).

18. *Curve Fitting Toolbox* The MathWorks Inc. Natick, Massachusetts, United State. https://www.mathworks.com/products/curvefitting.html.

19. Desgreniers, S. & Lagarec, K. XRDA: A Program for Energy-Dispersive X-Ray Diffraction Analysis on a PC. *J. Appl. Crystallogr.* **27,** 432–434. ISSN: 1600-5767 (1994).

20. Celeste, A., Borondics, F. & Capitani, F. Hydrostaticity of Pressure-Transmitting Media for High Pressure Infrared Spectroscopy. *High Press. Res.* **39,** 608–618. ISSN: 0895-7959 (Oct. 2019).

21. Segura, A. *et al.* Nonreversible Transition from the Hexagonal to Wurtzite Phase of Boron Nitride under High Pressure: Optical Properties of the Wurtzite Phase. *J. Phys. Chem. C* **123,** 20167–20173. ISSN: 1932-7447, 1932-7455 (Aug. 2019).

22. Pan, Z., Sun, H., Zhang, Y. & Chen, C. Harder than Diamond: Superior Indentation Strength of Wurtzite BN and Lonsdaleite. *Phys. Rev. Lett.* **102,** 055503 (Feb. 2009).

Chapter 5

Heating Under Pressure

5.1 Introduction

Inspections of hBN under high pressure and high temperature are motivated in the search for new BN crystallographic networks. As outlined in Chapter 1, in their separate computational results, Hromadová[1] and Wen[2] have predicted a meta-stable body-centered tetragonal phase of BN (bct-BN) that would be formed at HPHT conditions near, but below, the hBN-wBN transition pressure. This phase has yet to be observed experimentally. Furthermore, heating hBN in a N_2 atmosphere could potentially promote the incorporation of N_2 molecules into the hBN network, essentially creating an intercalation compound. Nitrogen intercalation compounds of BN under sufficient pressures (10-15 GPa) could lead to BN networks possessing single bonded nitrogen, and other features of great interest[3–5], as discussed in Chapter 1.

We have experimentally explored the changes of dense hBN at elevated temperature with the goal to find pathways to synthesize novel phases of BN, like the predicted bct-BN and the intercalation and related compounds.

5.2 Experimental Procedure

Laser heating on samples at high pressures was performed at the SPring-8 synchrotron radiation facility, BL10XU beamline, and the Advanced Photon Source (APS), HPCAT (16ID-B) beamline. The heating apparatuses included a near infrared laser directed by glassy carbon mirrors into the DAC from both sides, simultaneously both sides. At the

BL10XU and 16ID-B beamlines, laser heating and X-ray diffraction could be performed simultaneously, probing through the glassy carbon mirrors. The incoming laser power from upstream and downstream directions, defined with respect to x-ray propagation as shown in the setup in Figure 5.1, could be adjusted independently to provide the same amount of heat from both sides, judged by the measured temperature from blackbody radiation. The blackbody radiation produced in response to being heated was reflected by the glassy carbon mirrors and collected in a spectrograph, where the spectral profile would be fitted to the Plank radiation function[6]. Though the reported standard deviation of the temperature measurement is reported to be around 5 K for their for an extended exposure (1-2 hours)[6], we would observe fluctuations in the hundreds of degrees K for a given laser power incident on our samples.

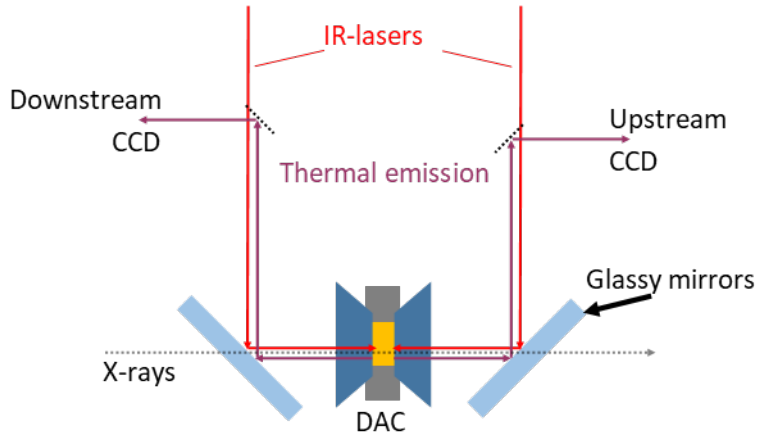

FIGURE 5.1: Schematic of the laser heating setup that was used at the APS 16ID-B beamline.

Because hBN has a very large band gap (6 eV, corresponding to a wavelength around 200 nm[7]), it does not couple with the heating lasers emitting at 1.15 ev ($\lambda = 1.07\mu m$), and thus it cannot be heated directly (this was realized after two attempts to do so led to anvil fractures). To perform laser heating, there needs to be a heating element to couple with the laser light and impart the heat into the surrounding environment and hBN sample. In our studies, we will describe 2 such methods.

index	PTM	Heating element	Facility used
1	NaCl	Re ring	APS
2	none	Li	APS
3	NaCl	Graphene nano-platelets	APS
4	NaCl	Boron	APS
5	N2	graphite	APS
6	N2	Boron	APS and SPring-8

TABLE 5.1: A quick summary of the different heating configurations attempted. The APS and SPrin8 facilities used were the HPCAT (16ID-B) and BL10XU beamlines, respectively. The two additional samples without any pressure transmitting medium resulted in an anvil fracture and no observed heating. The graphene nano-platelets, amorphous boron, and graphite heating elements all were used as powder heating elements. The configuration containing lithium is discussed in the following chapter.

The first method employed a single, solid metal heating element with the sample enclosed. In this method, a thin ring of rhenium packed with hBN, was placed under high pressure conditions. This thin metal ring was used to couple with the near-IR laser and provide a concentric source of heat, radially diffusing to the enclosed material. The procedures and results of these methods make up the following sections. Care was taken to ensure that layers of thermally insulating NaCl separated the ring from the edges of the gasket and the diamond anvils, lest the heat be conducted through them. This assembly is presented in Figure 5.2.

The other heating method used was in the form of powder light absorbing elements. Here, a powder of a non-reactive heating material is mixed with hBN powder. This mixture is then placed within an insulating medium within the DAC, as shown in Figure 5.10. When irradiated by the heating laser, this powder radiates heat into the surroundings, including the hBN which has been mixed with it.

The many different configurations employed are summarized in Table 5.1. The results of the successful experiments are discussed for the remainder of this chapter.

5.3 Rhenium Ring Heating Element

The ring-shaped heating element was assembled in a two stage fabrication process. First, the hBN powder was compressed inside a 20 μm thick Re gasket. Then the sample-packed gasket was cut out and placed in an excavated bed of NaCl packed in the compression chamber of a final gasket. Figure 5.2 shows the schematic diagram of the sample configuration and a photograph of the sample assembly. Additional NaCl was layered on top of the ring to ensure thermal isolation of the sample. In sealing the DAC, the sample was initially compressed to 1.41 GPa.

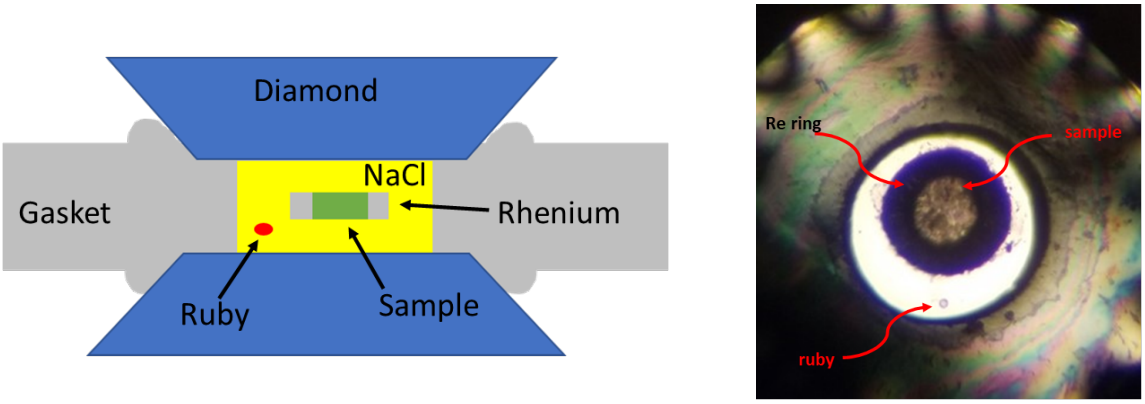

FIGURE 5.2: Cross-section schematic and top-down picture (through diamond) of the rhenium ring heating assembly within a DAC.

Laser heating cycles were performed at 7 pressure steps from 1.4 to 12 GPa. Diffraction images were taken at the heating position for several laser powers during each heating cycle. X-ray transmission/diffraction scans were performed before and after each heating cycle to closely monitor the status of the sample, like the one shown in Figure 5.3 for 1.4 GPa. For the scan map illustrated in Figure 5.3, the first position within the bulk of the NaCl region contains only NaCl X-ray diffraction lines, likewise for the third position probing the gasket, which only shows Re lines. The second position shows X-ray diffraction from both species, as there is NaCl separating the Re ring from the anvils. Note the

lesser intensity of the X-ray diffraction lines in the third plot. This is due to the immense scattering intensity from Re, reducing the transmitted signal.

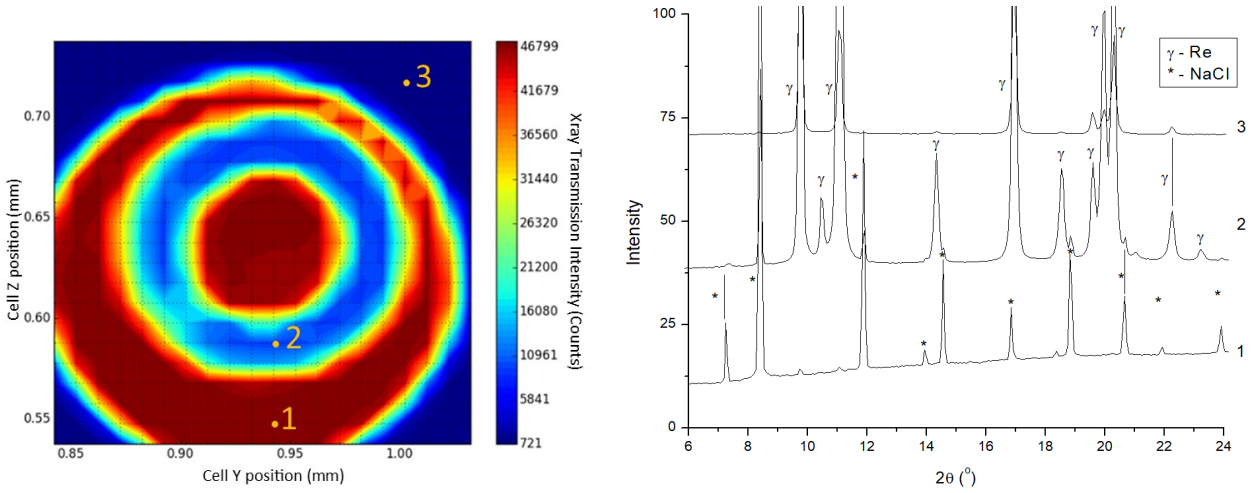

(A) X-ray transmission scan.

(B) Corresponding XRD patterns for the positions in Figure 5.3a.

FIGURE 5.3: X-ray transmission scan of the rhenium ring system at 1.41 GPa. 5.3a shows x-ray transmission across the cell. The frame of dark blue (low transmission) is the rhenium gasket, while the interior light blue section is the rhenium ring. The red areas (high transmission) are where there is NaCl, the section interior to the blue ring also containing hBN. For the selected regions in 5.3a, the diffraction pattern is shown in 5.3b.

During most laser heating cycles, the signal from the heated source would drop due to the ring moving away from the beam, by a combination of thermal displacement, laser pressure, or from excavation of the target by the focused laser beam. The position of the laser beam within the cell would be adjusted accordingly to maintain a continuous heating over the course of the heating cycle. At the initial pressure of 1.41 GPa, heating was performed to a temperature of 1280-1485 K, as measured by upstream and downstream blackbody emission, respectively. The pressure was then increased to 7.34 GPa in 1 GPa steps before heating was performed again, as this pressure was well above the predicted 6 GPa stability point for the bct-BN phase[2]. All heating cycles following the initial one at 1.41 GPa reached a maximum temperature of 2100-2500 K, with the exception of one at 7.34 GPa which reached a maximum of 1650 K.

5.3.1 NaCl as a pressure and temperature gauge

Since the ruby microsphere was located outside the rhenium ring, local pressure difference due to any existing pressure gradient would not be observed by this pressure gauging method. Furthermore, the ruby fluorescence gives a measure non-representative of the pressure within the adjacent ring. As such, the NaCl cell volume was used as a localized sensor. NaCl has has been studied in depth[8–12]. As a soft material with a small bulk modulus, NaCl has a dramatic dependence on pressure. For this reason, the use of the change of the unit cell of NaCl as a pressure gauge has been investigated[13], where the compression of NaCl under pressure would be consistent with it's equation of state. The Vinet-Rydberg equation of state (EoS)[14] was chosen such that the corrections can be made accurately for HPHT conditions. For the EoS,

$$P_{NaCl}(V) = 3B_0(\frac{V}{V_0})^{-\frac{2}{3}}(1-(\frac{V}{V_0})^{\frac{1}{3}})\exp(\frac{3}{2}(B_0'-1)(1-(\frac{V}{V_0})^{\frac{1}{3}})) \tag{5.1}$$

the bulk modulus B_0 and derivative bulk modulus $B_0' = \frac{dB_0}{dP}$ used were reported by Chauhan and Singh *et al.*[8].

Entering the observed unit cell volume V_0 for NaCl into this EoS yields the pressure expected for that region, with a precision related to the measured volume by X-ray diffraction. As shown in Figure 5.4, P_{NaCl} and P_{ruby} correspond well around the position of the ruby. Meanwhile, the difference in pressure between the interior and exterior of the ring is significant. The pressure difference between the P_{NaCl} at the ring interior and P_{ruby} remained about 5.5% at room temperature, reaching up to $\pm$10% at some points in the heating cycle. Using the X-ray diffraction pattern of NaCl, we now can calculate the pressure local to the X-ray probe.

During the heating process, there was pronounced thermal splitting of the NaCl diffraction lines, due to the fact that the X-ray beam passes through the entire depth of the DAC, including the heated regions and the more distant, unheated regions. The splitting and

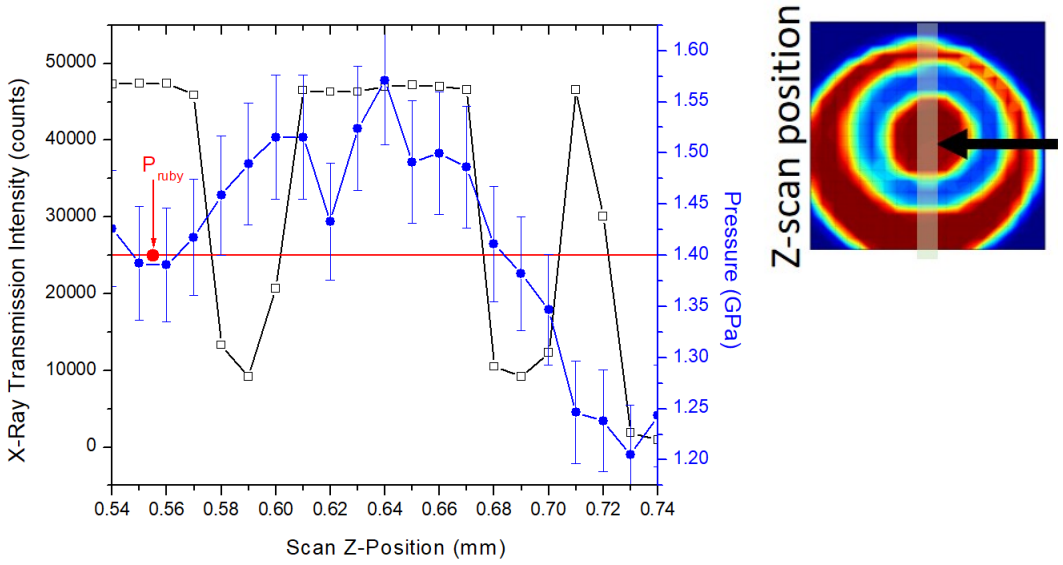

FIGURE 5.4: Pressure distribution at room temperature across the z-axis (radial) in the centre of the sample assembly, as measured by the NaCl compression in blue. The X-ray transmission intensity is plotted (black) alongside for reference, the two large dips in transmission marking ends of the rhenium ring. The red line indicates the pressure measured by ruby fluorescence, which is around a 0.1 GPa or 7% difference from the interior of the ring. Inset: the path (shaded in grey) which is being referred to.

broadening was so pronounced that many of the XRD lines were split beyond convolution, meaning that distinct X-ray diffraction lines were present from the heated NaCl, as well as from the unheated NaCl environment, as shown in Figure 5.5a. The unheated NaCl could therefore be used to determine the local pressure during heating, but the shifted NaCl lines could also be used to determine the local temperature with a much better local accuracy than the blackbody emission calculation, which only describes the highest temperature with the most intense emission.

Using thermal expansion of NaCl as a temperature gauge is much more complex than for pressure. Using the same EoS is no longer an option since the majority of the given parameters have a temperature dependence, and the volume of the heated, expanded NaCl unit cell can only be calculated if the diffraction lines can be sufficiently de-convoluted. A temperature-dependent representation of the equation 5.1 would be:

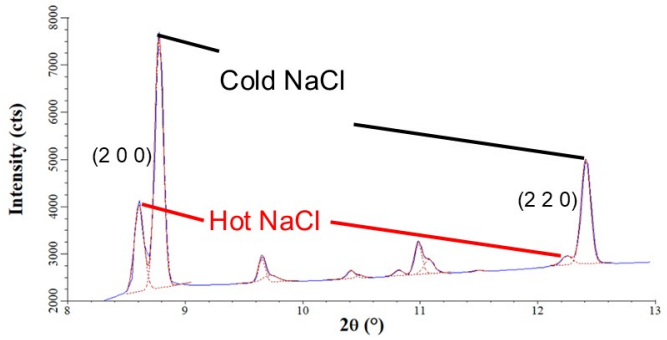

(A) XRD pattern during a heating cycle at 7.3 GPa, showing a distinct splitting in NaCl lines.

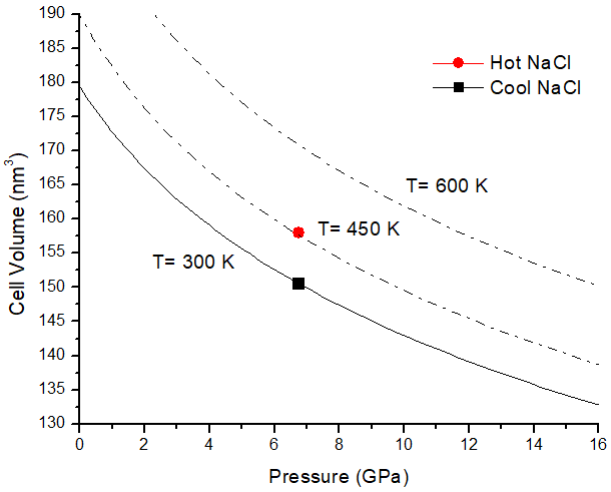

(B) Vinet-Rydberg equations of state for different temperatures.

FIGURE 5.5: Example of an XRD pattern (left) and EoSs of NaCl (right) during heating to 451 K. The unit cell volumes of NaCl are calculated from the pattern in Figure 5.5a and plotted in Figure 5.5b against the isothermal equations of state at 3 different temperatures for reference. The black square corresponds to the pressure calibrating cold NaCl data, and the red circle to the temperature calibrating red circle.

$$P(V,T) = 3K_0(T)\left(\frac{V}{V_0(T)}\right)^{-\frac{2}{3}}\left(1-\left(\frac{V}{V_0(T)}\right)^{\frac{1}{3}}\right)\exp\left(\frac{3}{2}(K_0'(T)-1)\left(1-\left(\frac{V}{V_0(T)}\right)^{\frac{1}{3}}\right)\right) \quad (5.2)$$

where T is the temperature of the system, in Kelvin, for the given measurement. Finding a relation for $V_0(T)$ is an essential first step. The important parameters in determining thermal expansion are the thermal expansivity α and the Andersen-Grüneisen parameter δ_T, defined such that

$$(\alpha/\alpha_0) = (V/V_0)^{\delta_T} \quad (5.3)$$

Where α_0 and V_0 are the values of thermal expansivity and volume at P=0 and T=0. Pressure and temperature both influence these parameters, the bulk modulus K_0 and its pressure derivative K_0'. This means that finding the expected change in volume due to an

elevated temperature - or even more useful, the temperature based on a change in volume - requires the consideration of the EoS for both room temperature and heated conditions.

Using the HPHT data for NaCl from Sheelandra and Vijay[10], the bulk modulus, derivative bulk modulus, thermal expansivity, and Andersen-Grüneisen parameter at zero pressure were numerically interpolated in relation to temperature, ensuring a goodness-of-fit of no less than $R = 0.9995$ within the 300-1050K temperature range. This produces an EoS for that temperature, as shown in Figure 5.5b.

Knowing the local pressure from the cold NaCl and being able to come up with a series of equations of state for any given temperature, the temperature estimation is simply a matter of finding the EoS that includes the observed volume at the calculated pressure. With all the independent relations feeding into the EoS, the temperature can be estimated by a numerical modulation of temperature for a chi-squared minimization of the difference between the calculated pressure and observed pressure: respectively, the pressure calculated from the EoS and the pressure estimated by the unheated NaCl cell volume calculation (using the same EoS at room temperature) with modulation of the temperature. The chi-squared curve shown in Figure 5.6 is much more precise than the blackbody emission calculation, with a statistical uncertainty of several degrees rather than several tens to hundreds of degrees for the latter.

Performing these temperature corrections for the heating cycles, we find that despite some of the blackbody temperature measurements reaching well above 2500 K, the NaCl temperature measurement barely estimated anything over 500 K, a temperature which a DAC can safely achieve in an evacuated oven. These two measurements are still compatible given that the temperature of the NaCl is likely to be much less than that of the rhenium which is the cause of much of the blackbody emission. This means that the rhenium much likely imparts much less heat inwards onto the sample than optimally desired. Further disappointingly, Figure 5.7 shows that there seems to be no obvious relation between the blackbody measurement temperature and the calculated NaCl temperature,

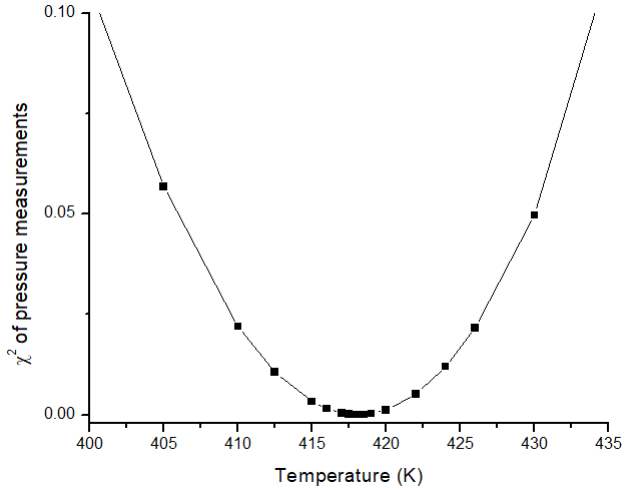

FIGURE 5.6: Chi-squared difference of pressure calculations, between that calculated by the HPHT EoS, and that calculated by the low temperature EoS. Modulation of temperature in the temperature dependent EoS modulated the pressure in order to minimize this difference and calibrate for temperature. The values shown are of the temperature calculation for the sample at 7 GPa and heated by lasers above 16 W on both upstream and downstream side of the DAC.

indicating that the probe being used was unreliable for the purposes of this experiment. This non-correlation between estimated temperatures an be related to several aspects. The main two possible explanations are considered next.

The rhenium heating target may indeed not be imparting enough heat onto the surroundings to sufficiently or reliably raise the temperature, whether that heat be transferred into the rest of the rest of the ring or just not far enough into its surroundings. Much of the thermal energy could also be lost from the ring by thermal conduction through the NaCl to the diamond heat sink. Simulations of heat losses could help in understanding the problem but has been judged beyond the scope of the present work. Another explanation could be imperfect alignment between the X-ray probe and laser heating/blackbody spectrometer focus, where the spot closer to the laser is of higher temperature than the region probed by the X-rays. While this is certainly true to some degree, the post-heating X-ray transmission scans yielded no sign of any substantial difference in temperature, such as recovered metastable phases.

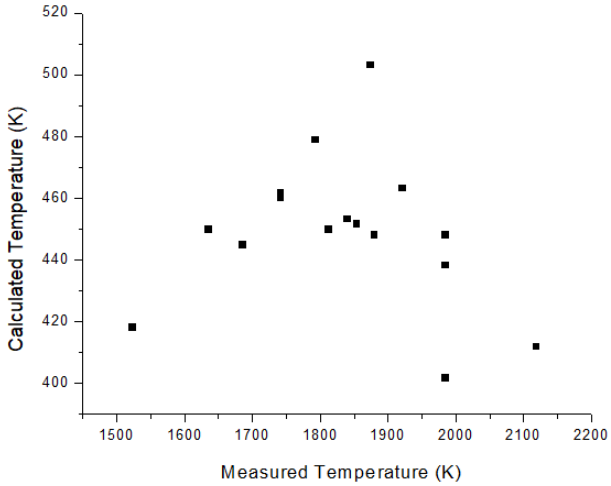

FIGURE 5.7: Relation between the temperature estimate from the NaCl EoS method and the measured temperature from blackbody emission. The odd, triangular shape of the data points seems to imply that there is a nontrivial relation between the two measurements.

5.3.2 Analysis with improved P-T measurements

With better estimations of the local pressure and temperature, the effect of laser heating on the hBN sample can be investigated more accurately. Unfortunately, since too little heat was imparted to the material under study to reach the desired temperatures, no novel phase transition behaviors in BN were realized. The observed expansion which results from increased temperature is shown in Figure 5.8. The correlation between temperature and sample expansion is weakly in agreement with previous literature[15]. Were higher temperatures reached, the relation here would presumably be much clearer.

Upon nearing the 9 GPa hBN-wBN transition pressure boundary, the pressure rapidly increased, surpassing the pressure for the expected transition, reaching a pressure of $P_{ruby} = 12.0$ GPa ($P_{NaCl}(ring\ interior) = 14.2$ GPa). Figure 5.9 shows that this lead to hBN being totally converted to wBN. This is in interesting contrast with the spectroscopic studies of BN in KBr, where non-hydrostatic strain inhibited the hBN-wBN transition.

The results for the wBN heating cycle were interesting from the beginning. The difference between P_{ruby} and P_{NaCl} at the ring interior was more than 2 GPa, with P_{ruby} =12.0

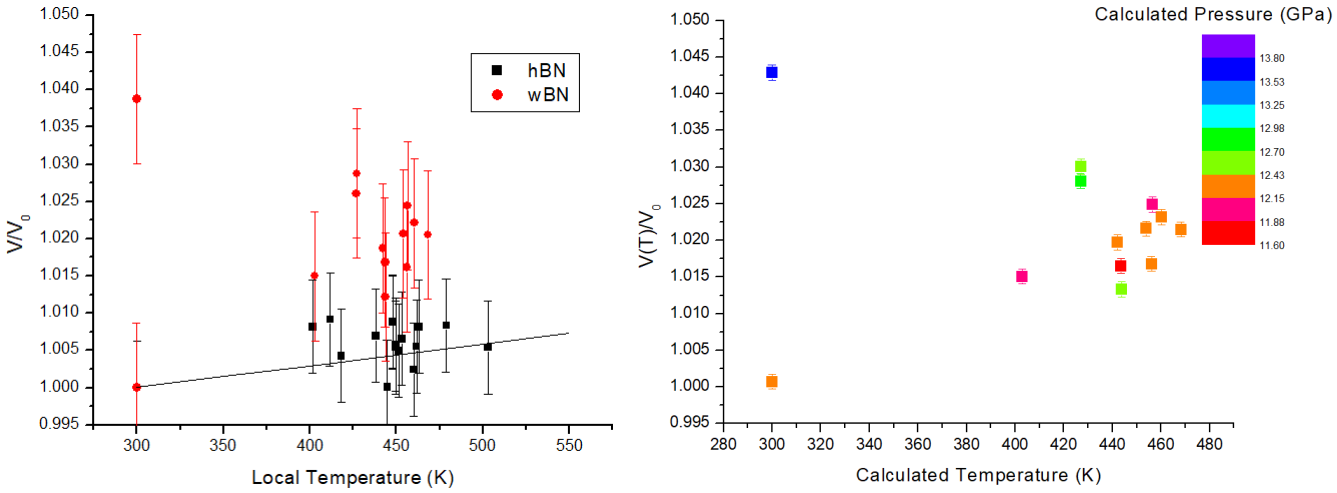

FIGURE 5.8: Thermal expansion at $P_{ruby} = 7$ GPa and $P_{ruby} = 12$ GPa for hBN and wBN, respectively. There seems to be some expansion caused by heating, but it is not much more than the uncertainty (error bars). The line describes the expected value at the given conditions for hBN according to Solozhenko[15], while no reports can be found for wBN. The colour plot adds context to the state of the pressure within the wBN cell.

and P_{NaCl} =14.2 GPa, respectively. Following the heating cycle, this difference closed by half, measuring P_{ruby} =11.1 GPa and $P_{NaCl}(ring\ interior)$ =12.3 GPa. In Figure 5.8, the $V/V_0(T = 300K) > 1$ point occurs just before the heating cycle, indicating a reduction in volume after the heating cycle. Interestingly, the cell volume is largest for the larger values of P_{NaCl}. This is the opposite of what would be expected from a either a reduction in pressure or an increase in temperature, while here we observe both! If, as claimed by Chen *et al.*[16], the wBN structure is stabilized by a network of defects, the heating may have annealed some of these defects out of the network, resulting in a more condensed network. The thermal expansion also seems to be much greater than that of hBN, owing to the 3-dimensional bonding of wBN, and possibly due to the laser coupling with defects in wBN. Nonetheless, the degree of volume change is shocking and deserving of further investigation.

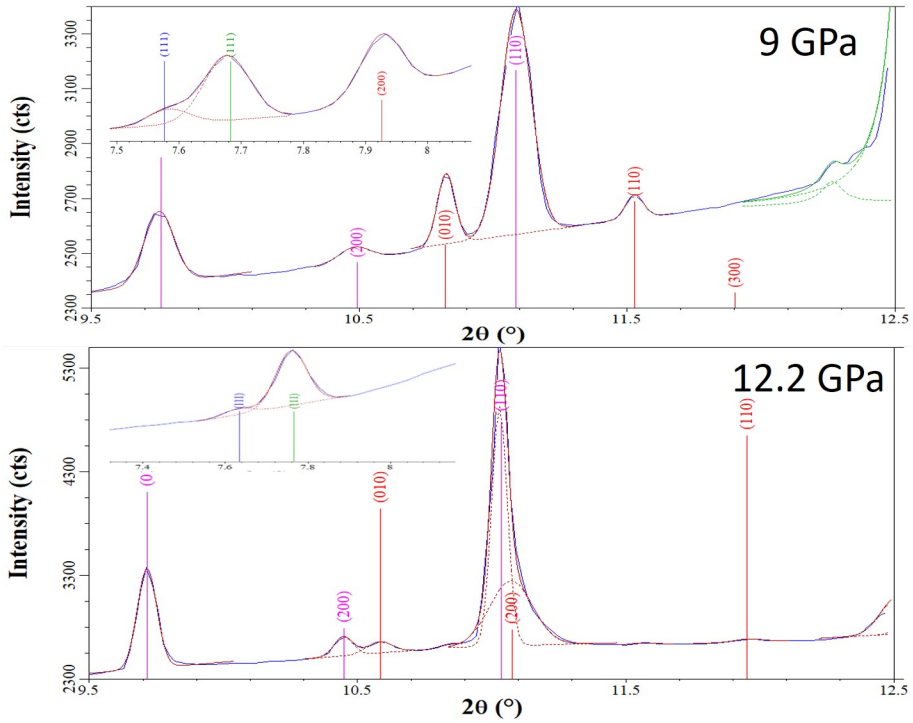

FIGURE 5.9: XRD patterns of the sample before and after the hBN-wBN transition above 12 GPa. The BN species, noted in red by the histogram, is completely different between the two pressures, meaning that all hBN was converted to wBN in the second image. The pink lines (vertical) denote Re X-ray diffraction lines, while green and blue lines denote cold and hot NaCl, respectively.

5.4 Powder heating element

For the following experiments, powder heating elements were mixed with the sample in a fashion similar to shown in Figure 5.10. As given in Table 5.1, many sample configurations with powder heating elements were attempted. While some showed no signs of heating in hBN, neither an increase in the lattice parameters nor additional X-ray diffraction lines, interesting effects were observed among the rest of the data.

For sample 6, by the index given in Table 5.1, hBN powder was mixed with amorphous boron powder (98% purity) for the purpose of coupling with the heating laser and loaded under a N_2 atmosphere. Heating was done under 3.7 GPa to a maximum average temperature of 1650 K, as observed by thermal emission. At this temperature, no more than 0.6% increase in volume was observed in hBN, relating to 500K according to calibration

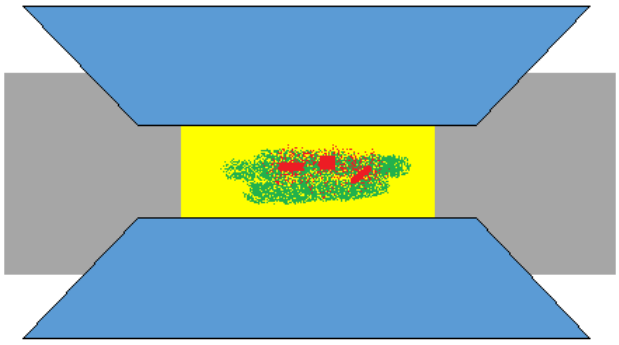

FIGURE 5.10: Sample assembly for laser heating using a powder heater. The sample (green) is roughly mixed with a laser absorbing powder (red) and placed in an insulating PTM (yellow). The diamonds are shown in blue and the metal gasket in grey.

reported by Solozhenko[15]. Several additional X-ray diffraction lines were observed in the pattern following the heating, as shown in Figure 5.11. The new existing X-ray diffraction lines could be resolved with the combination of two structures, one hexagonal and the other tetragonal. The structural parameters of the proposed structures are listed in Table 5.2 alongside that of the potentially corresponding compounds.

The hexagonal structure fitted to the parameters is what could be expected of an hBN lattice that has expanded due to the intercalation of light material. The difference in lattice parameters between this new phase and that of hBN would an increase of 2% and 12.5% in the *a*- and *c*- directions, respectively. This is strikingly similar to the expansion that has been observed for lithium intercalation compounds, which may be noted from Table 5.2 to be an increase of 2.48% and 12.9% along *a* and *c* directions, respectively, compared to hBN[18]. Furthermore, an expansion along the *c*-axis of 11-23% has been shown for intercalation of larger molecules[19], placing our observations well within the appropriate range.

Our reported tetragonal structure would have lattice parameters consistent with those calculated for the proposed bct-BN structure. At the reported pressure, the observed unit cell volume has less than a 0.08% difference with the bct-BN reported by Hromadová[1]

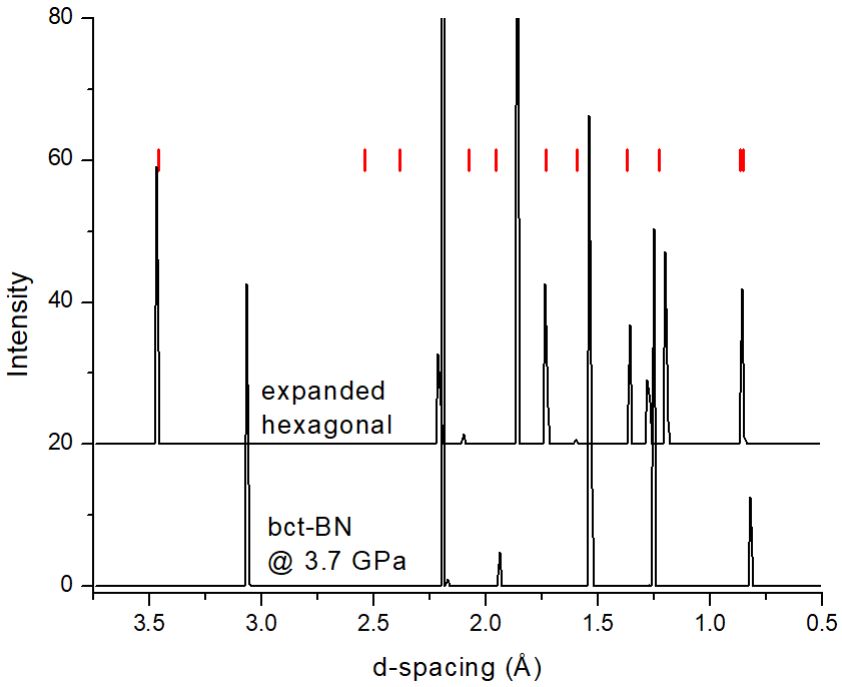

FIGURE 5.11: Histogram of novel XRD lines from hBN heating experiments and simulated XRD patterns of proposed. All unidentified X-ray diffraction lines observed at 3.7 GPa after heating are represented by the red symbols. The powder patterns for proposed structures, simulated in Diamond 3.2[17], are shown with a vertical offset for clarity.

after accounting for pressure effects. While these proposed structures account for numerous of the new diffraction lines, neither incorporates all of them, and most of those used for each one's refinements are shared between them. Due to the lack of additional X-ray diffraction patterns displaying this, the weak intensity of these lines, and the low maximum temperature observed, it is not very convincing that the potential tetragonal structure observed could be the predicted bct-BN.

Substantial heating of hBN was observed for another sample (index 3), which provided a good opportunity to compare the optical thermometry carried out by thermal emission to that of the NaCl thermal expansion approach. For this case, graphene nano-platelets were used as a laser light absorbing material for another study of laser heating of hBN. For this sample, the nano-platelets were mixed with hBN powder and placed in the compression chamber surrounded by NaCl powder within a Re gasket. A heating

Substance	a/c (Å) at P=0 GPa	a/c (Å) at P=3.7 GPa	Unit cell volume (Å^3) at P=3.7 GPa	Source
hBN	2.505/6.66	2.496/6.15	33.227	this work
Li-intercalated BN	2.567/7.5198	N/A	39.383	[18]
Observed hexagonal	N/A	2.55/6.925	38.867	this work
bct-BN (simulated)	4.37/2.52	N/A	47.659	[1]
Observed tetragonal	N/A	4.33/2.54	47.622	this work

TABLE 5.2: Structural parameters of the observed HPHT structure/s and similar reported ones. The unit cell volume of bct-BN at P=3.7 GPa is calculated based on the BM-EoS and the structural parameters given from Hromadová[1]. The unit cell volume of Li-intercalated BN at P=3.7 GPa is calculated based on the approximation that the % increase of both a and c parameters relative to the bulk hBN remains the same at the same at this pressure. While the Li-intercalated BN structure is not fully representative of a N_2-intercalated BN, it is the obvious comparison to make because it is a light element and the only elemental intercalant experimentally observed in hBN.

cycle was performed under 4.17 GPa, as measured by the ruby gauge, to a maximum of 2200 K upstream, or 1781 K downstream, as measured by blackbody emission. However, the maximum T_{NaCl} recorded by XRD was only 434 K, and measured much earlier in the heating cycle than the highest $T_{blackbody}$. The XRD diffraction pattern related to the highest calculated temperature by our NaCl method also showed new peaks, reaffirming the need for the second temperature measurement. No additional peaks were observed for any following acquisition.

Thermal expansion of hBN was observed, reaching a maximum expansion of 1.4% by volume. As shown in Figure 5.12, the thermal expansion expected by Solozhenko[15] lies in between both schemes, where the 1.4% expansion relates to about 700 K, between the highest NaCl temperature ($T_{NaCl} < 500K$) and the lowest blackbody temperature ($T_{blackbody} > 700K$). The expansion curve cuts through the space between both measurements. Interestingly, although the NaCl temperature data lies more closely to the expansion curve, the blackbody data has a much more linear correlation. Our findings are that these measurement schemes are complimentary. Even without considering the incredible speed of the blackbody method for estimating temperature, the trend of expansion compared to this scheme is much more linear, but further from the expected value.

As the blackbody emission method is related to the thermal emission from the hottest

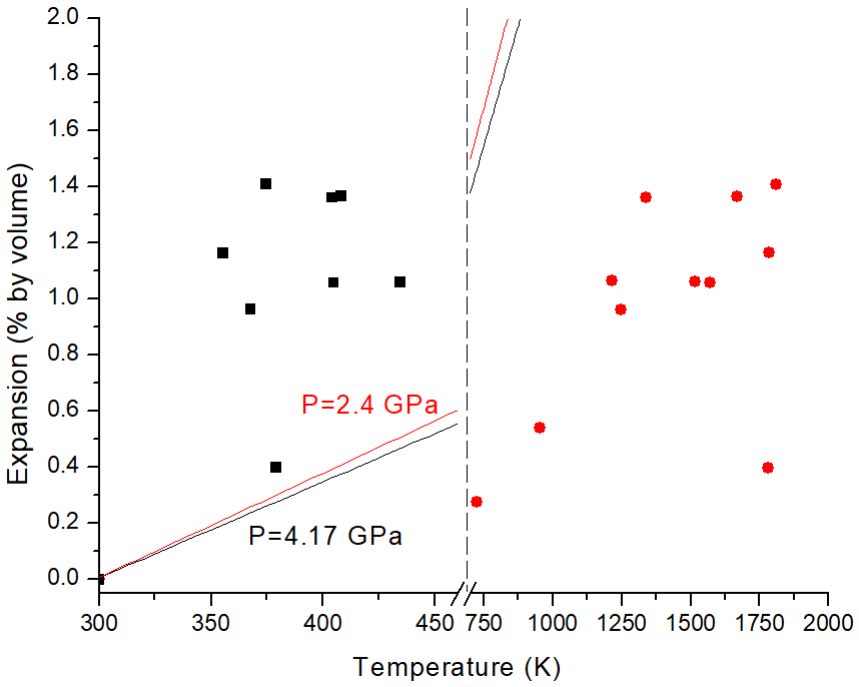

FIGURE 5.12: Thermal expansion of hBN under P_{ruby} =4.17 GPa (P_{NaCl} =2.4 GPa at cell interior). Values are given with respect to both temperature measurement schemes, with the NaCl thermal measurement left of the break and blackbody measurement to the right. The expansion lines expected, those reported by by Solozhenko[15], are shown for both reported pressures and indicate that the pressure difference between the two would have a minimal effect on thermal expansion. Note the different scales on the x-axis.

source in the probing region, this measurement sets an upper bound for the temperature, we would propose that the NaCl temperature measurement would similarly communicate a lower bound. The directly heated region of the sample is expected to be tiny (powder grains are submicron in diameter). The laser is absorbed, the highest temperature is measured by thermal emission, and heat is radiated into the surroundings by grains of the present powder, in this case graphene nano-platelets. The amount of nano-platelets (or other heating particles) present is so small that no XRD signature is observed from those. Because the heat imparted by these nano-flakes is less further away from their location with the sample, there is a greater amount of sample to probe which has a lower temperature, as shown in Figure 5.13. The diffraction lines from heated NaCl is then giving insight into the temperature distribution about the depth probed, even if it lacks the

small portion at the highest temperature where the signal is too weak to measure.

With the NaCl gauge describing of the temperature distribution as a lower bound, and the blackbody gauge as a description of the upper bounds, it can be inferred the true temperature the bulk of the hBN sample is exposed to lay somewhere in between. As shown in Figure 5.12, this is the case, with the expected temperature from the hBN EoS laying effectively between the two measurements for all points. Theoretically, for an assembly with a higher density, or a more even distribution of heating element, much more of the surroundings would be closer to the maximum observed temperature, leading to a more bimodal temperature distribution (one mode at room temperature, the other near the maximum temperature experienced by element particles), and the readings measurements from both gauges would approach both each other and the sample EoS line.

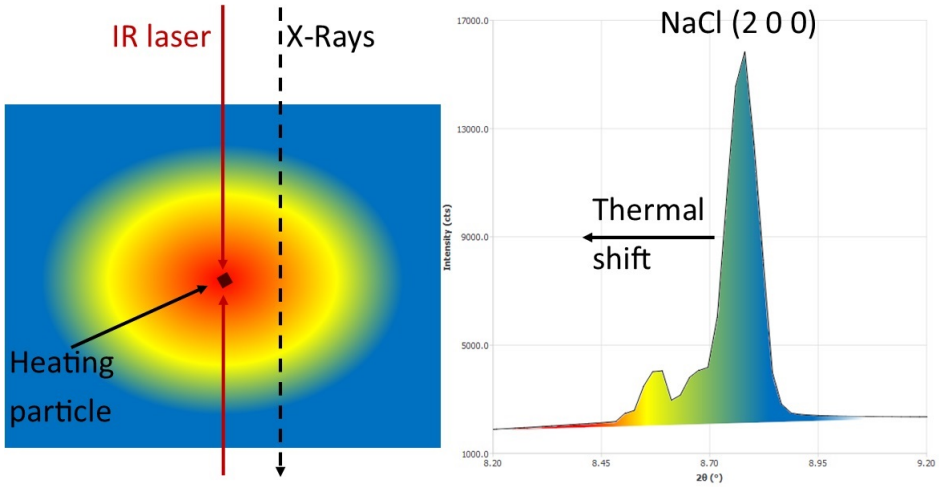

FIGURE 5.13: Schematic of the heat dispersion of a piece of powder heating element and its effects on a sample diffraction pattern. Regions of higher temperature are represented in red, and lower temperature in blue.

Based on the data recovered, the hBN unfortunately did not attain the temperatures where we would expect the novel phase transitions of interest (i.e., bct-BN), around 1200K or more[1]. Following heating, new X-ray diffraction lines were observed relating to interplanar distances of 2.50 and 1.46 angstroms. These new lines being weak and few, no new structure could be ascertained nor even prepared; It can be confirmed, however, that the

additional X-ray diffraction lines observed do not belong to an annealed graphitic carbon structure (which could have arisen from the carbon-based heating elements) and don't correlate with any other lines from other heated samples. They could arise from some form of C-B-N system, which is known to have numerous structures[20,21].

Laser heating was also performed on a sample of hBN mixed with lithium; this experiment will be discussed in the following chapter.

5.5 Summary

Several combinations of different PTM and heating elements were used to heat samples by mean of intense laser illumination. While all the heating elements were shown to heat the sample, not all the experimental assemblies were successful in this goal. Notably, only one of the samples loaded with a N_2 PTM was showed a significant thermal expansion. Several additional diffraction lines were present following heating cycles for some of the series, but were too few and too weak to determine the structure responsible. One of these series of novel diffraction lines seemed to fit either an intercalated hBN or bct-BN structure, though the conditions it was under make this improbable.

An alternative pressure and temperature measurement technique was explored. Using the unit cell volume of NaCl has been shown to be an effective way to get localized pressure and temperature measurements, possibly synchronously for high enough thermal expansion of NaCl. While these measurements will not replace the rapid thermal emission or ruby fluorescence measurements for many reasons, it has been shown to be highly complimentary to the existing methods. While the standard method approach to temperature measurement by spectral fitting of blackbody emission is rapid, it only sets an upper bound to the measured temperature for indirect heating experiments, so the slower NaCl EoS fitting gives insight to the temperature distribution and sets a lower bound for the

temperature. In reality, the temperature experienced by the bulk of the sample will be somewhere between the two temperature measurements.

5.5.1 Going Forward

One of the major challenges in the data analysis resulted from the fact that probing through glassy carbon mirrors led to reduced visibility of some sample peaks and made analysis of the sample imprecise or impossible in some cases. Future HPHT studies should consider using a much larger volume of sample in order to secure the chances of observing vital diffraction lines.

An alternative design for heating would be simply to heat recovered samples of hBN. As shown in Chapter 4, upon retrieval of a sample which had majorly converted to wBN, the transition was reversed resulting in varying relative quantities of hBN. This recovered hBN showed a different colour, as well as the E_{2g} Raman active mode having a frequency shift dependent on the incident laser light power. This indicates colour centres which cause a heating and expansion of the crystal structure. Considering the amount of heating we report due to coupling of the 532 nm laser used for Raman spectroscopy, the capability of heating these samples in a DAC without the presence of a heating element should be fully possible. The experiment may prove challenging due to the presence of unconverted wBN, but the lack of other foreign material and the more even distribution of heating source should provide a good setup for testing prior hypotheses. Unfortunately we did not have the time to realise nor prepare a sample of recovered, colour centre-dense hBN prior to the final synchrotron excursion. This is not very present in current literature, but whether this is because it is a new idea or something that wouldn't work is unclear. Most likely, under increased temperature, the defects would anneal and heating would stop, but this has still yet to be confirmed. This would nonetheless be a fruitful area of interest for future research.

Because the results from the rhenium ring assembly showed that it could be effective for indirect heating, it would be worthwhile to perform further experiments with a similar geometry. Other more complex heating element geometries could also be explored, such as a metallic screen geometry that could be micro-fabricated, a series of smaller rings, or a similar ring which is fragmented to reduce heat loss from conduction through the ring. An element made of a material with a higher heat capacity, such as epoxy+cBN (which could potentially cause confusion between the two phases) could be considered in order to impart more heat onto the system rather than further down the element.

Another area for which heating would be crucial is the intercalation of lithium metal into an hBN matrix, providing an intrinsic metallicity and further possibilities of novel phase transitions. This idea will be discussed more in the following chapter.

Bibliography

1. Hromadová, L. & Martoňák, R. Pressure-Induced Structural Transitions in BN from *Ab Initio* Metadynamics. *Phys. Rev. B* **84,** 224108. ISSN: 1098-0121, 1550-235X (Dec. 2011).

2. Wen, B., Zhao, J., Melnik, R. & Tian, Y. Body-Centered Tetragonal B_2N_2: A Novel Sp3 Bonding Boron Nitride Polymorph. *Phys. Chem. Chem. Phys.* **13,** 14565. ISSN: 1463-9076, 1463-9084 (2011).

3. Li, Y., Hao, J., Liu, H., Lu, S. & Tse, J. S. High-Energy Density and Superhard Nitrogen-Rich B-N Compounds. *Phys. Rev. Lett.* **115,** 105502. ISSN: 0031-9007, 1079-7114 (Sept. 2015).

4. Lin, S. *et al.* Prediction of Superhard B_2N_3 with Two-Dimensional Metallicity. *J. Mater. Chem. C* **7,** 4527–4532. ISSN: 2050-7526, 2050-7534 (2019).

5. Xie, C. *et al.* Superhard Three-Dimensional B_3N_4 with Two-Dimensional Metallicity. *J. Mater. Chem. C* **5,** 5897–5901. ISSN: 2050-7526, 2050-7534 (2017).

6. Meng, Y., Hrubiak, R., Rod, E., Boehler, R. & Shen, G. New Developments in Laser-Heated Diamond Anvil Cell with in Situ Synchrotron x-Ray Diffraction at High Pressure Collaborative Access Team. *Review of Scientific Instruments* **86.** APS HPCAT methodology, 072201. ISSN: 0034-6748 (July 2015).

7. Cassabois, G., Valvin, P. & Gil, B. Hexagonal Boron Nitride Is an Indirect Bandgap Semiconductor. *Nature Photonics* **10.** Comment: To appear in Nature Photonics, 262–266. ISSN: 1749-4885, 1749-4893. arXiv: 1512.02962 (Apr. 2016).

8. Chauhan, R. S. & Singh, C. P. Equation of State and Thermal Expansivity of NaCl under High Pressure and High Temperature. *Physica B: Condensed Matter* **387,** 352–357. ISSN: 0921-4526 (Jan. 2007).

9. Shanker, J., Kushwah, S. S. & Kumar, P. Equation of State and Pressure Derivatives of Bulk Modulus for NaCl Crystal. *Physica B: Condensed Matter* **239,** 337–344. ISSN: 0921-4526 (Aug. 1997).

10. Sheelendra, K. & Vijay, A. Equation of State, Thermoelastic Properties and Melting Behavior of NaCl at High Temperatures and High Pressures. *Journal of Physics and Chemistry of Solids* **123,** 364–370. ISSN: 0022-3697 (Dec. 2018).

11. Sumita, T. & Yoneda, A. Anharmonic Effect on the Equation of State (EoS) for NaCl. *Phys Chem Minerals* **41,** 91–103. ISSN: 1432-2021 (Feb. 2014).

12. Vinet, P., Rose, J. H., Ferrante, J. & Smith, J. R. Universal Features of the Equation of State of Solids. *J. Phys.: Condens. Matter* **1,** 1941–1963. ISSN: 0953-8984 (Mar. 1989).

13. Dorfman, S. M., Prakapenka, V. B., Meng, Y. & Duffy, T. S. Intercomparison of Pressure Standards (Au, Pt, Mo, MgO, NaCl and Ne) to 2.5 Mbar. *J. Geophys. Res. Solid Earth* **117.** ISSN: 2156-2202 (2012).

14. Vinet, P., Smith, J. R., Ferrante, J. & Rose, J. H. Temperature Effects on the Universal Equation of State of Solids. *Phys. Rev. B* **35,** 1945–1953 (Feb. 1987).

15. Solozhenko, V. L. & Peun, T. Compression and Thermal Expansion of Hexagonal Graphite-like Boron Nitride up to 7 GPa and 1800 K. *J. Phys. Chem. Solids* **58,** 1321–1323. ISSN: 0022-3697 (Sept. 1997).

16. Chen, C. *et al.* Stabilizing the Metastable Superhard Material Wurtzite Boron Nitride by Three-Dimensional Networks of Planar Defects. *Proc Natl Acad Sci USA* **116,** 11181–11186. ISSN: 0027-8424, 1091-6490 (June 2019).

17. Putz, H. & Bradenburg, K. *Diamond - Crystal and Molecular Structure Visulatization* Crystal Impact. 102, 53227 Bonn, Germany. http://www.crystalimpact.com/diamond.

18. Sumiyoshi, A., Hyodo, H. & Kimura, K. Structural Analysis of Li-Intercalated Hexagonal Boron Nitride. *Journal of Solid State Chemistry* **187,** 208–210. ISSN: 00224596 (Mar. 2012).

19. Kovtyukhova, N. I. *et al.* Reversible Intercalation of Hexagonal Boron Nitride with Brønsted Acids. *J. Am. Chem. Soc.* **135,** 8372–8381. ISSN: 0002-7863, 1520-5126 (June 2013).

20. Kouvetakis, J. *et al.* Novel Aspects of Graphite Intercalation by Fluorine and Fluorides and New B/C, C/N and B/C/N Materials Based on the Graphite Network. *Synth. Met.* **34,** 1–7. ISSN: 0379-6779 (Dec. 1989).

21. Yao, B., Chen, W. J., Liu, L., Ding, B. Z. & Su, W. H. Amorphous B–C–N Semiconductor. *Journal of Applied Physics* **84,** 1412–1415. ISSN: 0021-8979 (July 1998).

Chapter 6

Lithium-BN Mixture

This chapter details the brief side-project pertaining to mixtures of lithium and hBN under HP and HPHT conditions. The motivations for these investigations, the experimental procedures, results, and future research potential are discussed below.

6.1 Motivations

The objective of intercalating nitrogen into the hBN network is a large scale challenge with solid support of creating useful materials if the compound synthesized would be stable. One of the main issues with that proposal is that it is still not certain that nitrogen intercalation in BN is even possible, nor how an intercalated hBN compound (BNIC) will behave under increasing pressure (at least until the predicted phase transitions[1–3]). So the initial motivation for this side project was to find something else that could more easily or reliably be intercalated into hBN. By studying such a material under extreme conditions, insight would be gained into the potential behavior of a N-BNIC under similar conditions. After all, nitrogen has often been used as a PTM in conjunction with hBN. It stands natural to explore the possibility of any interaction of N2 with the BN compound.

Previous studies have shown intercalation in hBN to be much more challenging than with its iso-structural analogue of graphite. Intercalation for graphite and transition metal dichalcogenides are quite readily and regularly done; such materials compose massive field of materials chemistry due to the reliability of their intercalation compound's creation and applications for the ion battery industry. The standard way this is done in

industry is by redox reaction where the reaction between host and guest is sufficiently energetically favorable such that they can overcome the van der Waals attraction between the sheets. The difference for the case of hBN is that it is a large bandgap semi-conductor with a much stronger interlayer attraction, too strong for the redox reaction to produce a favorable result[4]. Reductive intercalation of potassium with hBN thin films has been shown[5], and bulk BN has been intercalated with certain Brønsted acids through thermal drying[6], but none of the successfully intercalated acids had any nitrogen; as a reminder, our interest in intercalated BN compounds is to increase the nitrogen content of the material, in order to enhance N-N interactions. The other current hBN intercalant and the most well studied would be lithium, having been intercalated into bulk hBN[7], hBN heterostructures[8], and hBN thin flakes[9]. Lithium has even been intercalated into hBN electrochemically, though likely just on in the surface[10]. This is still a new area of research, and as such, much has yet to be studied, including the properties of this class of materials under extreme conditions.

Insofar, bulk lithium-hBN intercalation compounds (Li-BNICs) have been synthesized, by way of milling and heating hBN powder with beads and powders of lithium nitride[11] or elemental lithium[12,13], with considerable success. An initial interest in having an Li-BNIC under pressure was inspired by the relationship between lithium nitrides of different stoichiometry as formed under pressure. Upon densification, the stable stoichiometry becomes increasingly nitrogen dominated, with the ambient being Li_3N and many other phases, with increasing nitrogen content, with Li_5 being favourable above 45 GPa[14] and metastable to ambient pressure[15]. While this isn't evidence that lithium intercalation will promote nitrogen intercalation, it is encouraging that some mix of the two are cause of interest at high pressure. It is therefore worth looking into whether nitrogen is capable of intercalation into Li-BNICs.

Nitrogen intercalation potential aside, Li-BNICs would be an interesting subject of research at high pressures in it's own right. The introduction of Li atoms to the hBN lattice would alter the structure of the compound, with the most likely result of changing

its properties. The symmetry is also expected to change from a 2L to 1L stacking[7,16], which would make the interlayer A_2u mode in hBN R-inactive, and make another Raman phonon mode become active, still with A_{2g} symmetry and similar energy. The relationship of this mode under pressure would be interesting to compare with the IR-active A_{2u} mode of bulk hBN. Furthermore, the electronic properties would be changed. The atoms introduced between the planes would supply extra electrons, closing the bandgap of the material. The calculated band dispersions predict that this would make hbn-Li-hBN layers become metallic. They would also be promising candidates for high-temperature, phonon-mediated superconductors, with a calculated critical temperature of 25K[16], while most of these types of superconductor having a T_C of less than 10K and the highest reported being 39K (in MgB_2[17]), both of these values for room pressure.

The metallic properties of a Li-BNIC compound could be exploited as a laser light absorber for heating purposes, with the plan to solve most of the problems discussed in Chapter 5. The hBN-wBN-type transition may be inhibited to higher pressures in a Li-BNIC compound. Lithium intercalated graphite transitions into the a diamond-type phase only at much higher pressures than for bulk graphite[18]. Li-BNICs, then, would not likely undergo the expected transition to a wBN-type structure until much higher pressures than that in bulk hBN. With this extended pressure upstroke hysteresis and heating potential, the conditions illustrated in[19] would then be much more accessible, and a HPHT transition into a bct-type structure might be greatly simplified, even made possible. As implied, the phase transitions of Li-BNIC wouldn't necessarily be into wBN or the predicted bct-BN phase, but potentially into a similar but distorted structure with a notable lithium content. They would possess similar, though likely weakened, elastic properties while greatly different electronic properties, such as the LiC_6 hexagonal diamond being a metallic state[18]. We would also expect a large hysteresis on the down-stroke in pressure for potential metastability in ambient conditions.

A notable by-product that is sometimes observed[11] in these processes is the creation of

a Li_3BN_2 composite. There exists 3 closely-related phases of the composite[20]. The research on these composites seems quite limited, and no reports could be found on them under high pressure conditions, meaning that if the intercalation ends up unfavorable compared to the composites, the research will still be on a novel subject.

6.2 Experimental Setup

Sample preparation for a lithium mixture with BN poses several experimental challenges. Foremost, lithium is incredibly unstable, and readily reacts with air under ambient conditions to form lithium hydroxide, lithium nitride, or lithium oxide. Furthermore, the low Z number of the element makes it to be a weak X-ray scatterer; detection and quantification by XRD proved to be more difficult. Moreover, the small size of lithium atoms makes it prone to diffusion into it's surrounding materials. This is the case in diamond, where lithium has been observed to diffuse, resulting in the cracking of diamond anvils while under pressure[21]. A pressure-induced reaction has also been observed above 200 K, leading to damage of the diamond anvils[22]. The challenge then is to prepare a sample of the lithium-BN mixture without exposing it to air and moisture, while limiting the contact of lithium with the diamond anvils.

It might not be necessary to mill the mixed sample to produce intercalation, heating a mixture of hBN and either lithium or lithium nitride above 1000 K under standard pressure seems to be enough to produce BNICs[11,23]. Consequently, in our experiment, it was decided that a sample would be produced from a simple hBN/Li mix that would be put under pressure. In the case that the application of mutli-gigapascal pressure is not enough to promote intercalation of lithium, heat would be necessary. To that end, the encased lithium, as a metal, would couple to an IR laser light, acting as a heating element (as discussed in Chapter 5). This approach may reasonably be capable of heating the mixture above 1200K where lithium intercalation has been observed to occur in hBN.

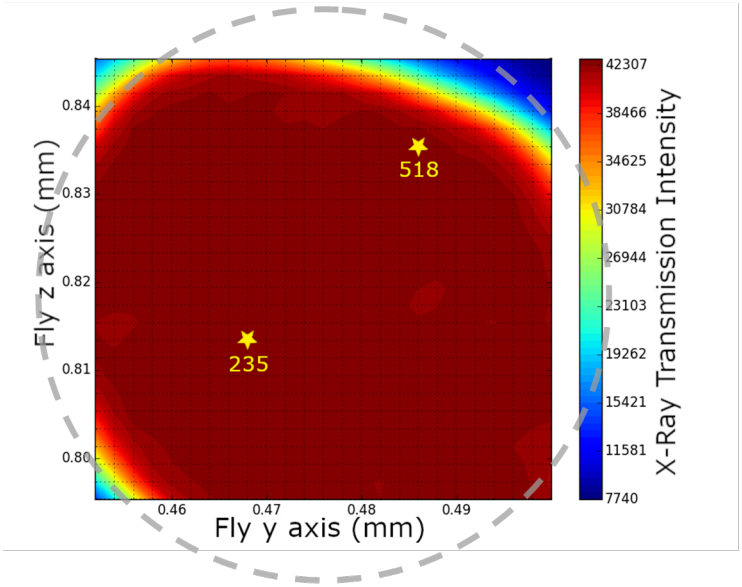

FIGURE 6.1: A 2D-map of X-ray transmission values of the Li+hBN sample area. The sample is in a DAC. Each intersection of the overlaid cross-hatching indicates the location assigned for each X-ray transmission measure and the corresponding X-ray diffraction pattern, for a total of 650 separate measurement points and patterns in this case. A circle of 60μm diameter is overlaid to represent the dimensions of the sample chamber. The numbered stars indicate specific positions referenced within the text.

A diamond anvil was fitted with a rhenium gasket with a 60 μm diameter sample cavity. hBN powder was packed into the cavity by applying a load from the piston, then the cell was placed under a controlled argon atmosphere in a glove-box for loading of the lithium. Pure lithium beads were placed on top of the packed hBN pellet. The sample cavity was capped off with additional hBN powder, hence creating a lithium sandwich, isolating the metal from the diamond anvil surfaces. No pressure transmitting medium (PTM) was included in this sample.

The cell piston was replaced and a small load applied to the sample in order to seal it off from the atmosphere prior to its removal from the glove box. Upon application of the load, the initially whitish hBN powder turned dark and opaque on one side. Ruby fluorescence showed a pressure of 4.3 GPa.

This sample was brought to the Advanced Photon Source (APS) at Argonne National Laboratory for XRD. X-ray diffraction patterns were recorded at the central position for

the cell with a 10s exposure. An initial 2D area scan which was a 50x50 μm region, centered on the central position. The scan took measurements at 26x26 points within the region, forming a grid of patterns that were recorded with a 1s exposure per point. The transmission measurement for each point in this scan forms the map shown in Figure 6.1. The mismatch between the initial and measured sample cavity dimensions indicates that the cavity deformed substantially upon applying pressure. With the X-ray beam aligned with the counter-propagating infrared heating lasers set in the centre of the sample, heating was attempted. The incident laser power was slowly increased up to 13.1% (of the maximum 100 W) before quenching the sample to room temperature. The black-body emission from the sample was too weak for recording and curve fitting, and thus we were unable to measure a temperature during the heating cycle. An X-ray diffraction pattern was taken while the sample was illuminated at the highest incident laser power; no X-ray diffraction was recorded after quenching, unfortunately. While it would have been useful to keep this sample for future experiment, one of the diamond anvils broke shortly after this experiment, following the heating, potentially compromising the sample with exposure to ambient atmosphere at the very least.

6.3 Analysis

Due to the limited time and resources, analysis of the data was held until after the run of beamtime at the APS. The X-ray diffraction images were processed using the Dioptas software[24] for the purpose of processing and integration to obtain a 2 theta diffraction plot. Of the 650 images produced by this map, 36 were selected for in-depth analysis using the XRDA program[25]. This selection was made based on (i) the features of their image and processed 2θ plot; (ii) whether they had new features that weren't present or clear in other selected images; (iii) sufficient separation from the gasket in order to reduce the appearance of X-ray diffraction lines or pressure effects related to the gasket, though

an image directly on the gasket and 2 images on opposing gasket edges were taken as references; (iv) an image was selected for thorough analysis at least once every 3 passes (about $6\mu m$). The selection is shown in Figure 6.2.

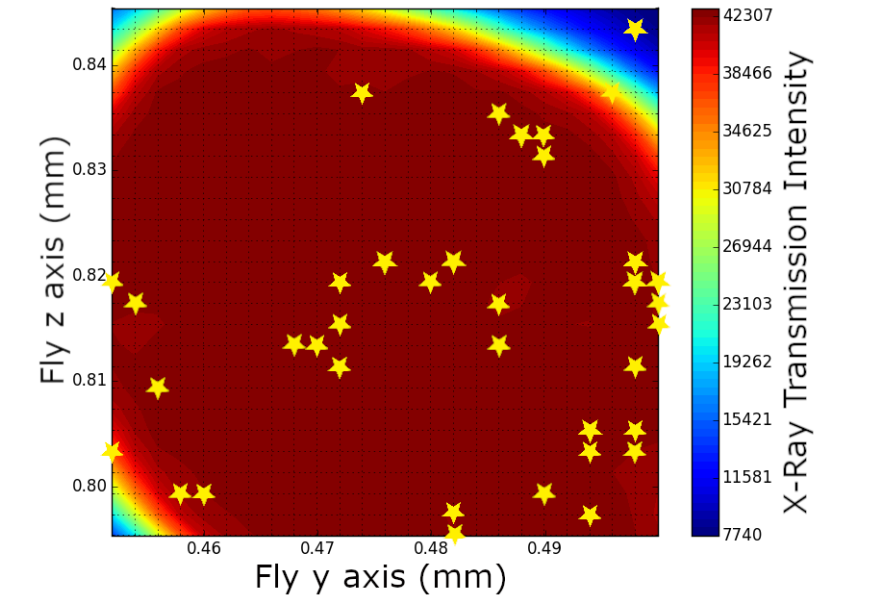

FIGURE 6.2: The same X-ray transmission mapping of the 2d scan taken of the Li+hBN sample seen in Figure 6.1, now marked off with all the locations of which the corresponding x-ray diffraction pattern was selected for in-depth analysis.

The analysis of the reference gasket X-ray diffraction image revealed a sustained signal from hBN and, on the edges of the gasket, a stronger X-ray diffraction signal was received than that in any position interior the sample chamber. This observation seems to imply that upon the preparation of the sample and the final placement of the piston anvil, there was a significant overflow of hBN from the sample chamber onto the gasket. The extra spread of the capping hBN may provide an explanation of the failure of the diamond anvil observed at the end of the experiment. If enough of this capping material had indeed spread away from its initially intended central position, the likelihood for lithium to be in contact with the diamond anvil is higher; lithium is known to diffuse in diamond and cause breakage at 21 GPa and room temperature[21]. This is what is assumed to have taken

place for this experiment. Even though the pressure was well below 21 GPa, the laser heating process could reasonably have increased the diffusion of the lithium.

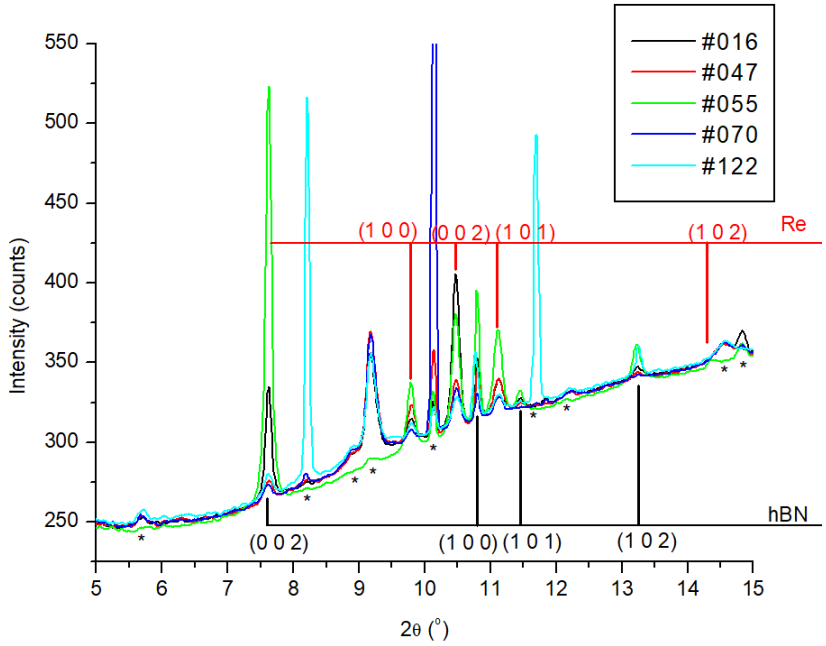

FIGURE 6.3: A collection of X-ray diffraction patterns from various regions of the sample (Figure 6.2) depicting the general distribution of diffraction lines. Patterns from different positions are marked by a difference in colour. In most regions of the scan, these were all the lines observable, often with varying relative intensities. Interestingly, while the majority of these features can be assigned to the structures of hBN or Re, there are still a number of relatively prevalent lines which cannot be assigned to any expected structure.

Initial inspection of the X-ray diffraction patterns revealed what was anticipated: a very weak diffraction signal. In fact, no X-ray diffraction lines related to the Li metal structure were observed from the sample. Given its small amount compared to hBN powder and its low Z number, it can be argued that our observation does not prove to whether pure Li was still present in the compression chamber. Surprisingly, the X-ray diffraction signal from hBN was just as weak as the signal from Re at positions deep into the sample area, i.e., far away enough to expect a minimal to no diffraction signal from the gasket. The sustained presence of such X-ray diffraction lines was discussed already in Chapter 5: it is potentially due to the incident X-ray beam having a larger size than expected with

a distribution having substantially extended tails.

Most of the mapped area showed X-ray diffraction patterns that were very similar in features, the main differences between them being the relative intensities of the XRD lines, as shown in Figure 6.3. Most of these common features at different positions of the samples were complete or nearly complete X-ray diffraction rings, therefore arising from either powders or highly polycrystalline materials and the majority of these X-ray diffraction lines were with no doubt related to the structures of hBN or (hcp)Re. The remaining X-ray diffraction lines recorded are not easily accounted for with anything else expected. The weak line at $2\theta = 5.7^o$ is especially concerning, as it relates to a d-spacing too large for any known lithium nitride, oxide, or hydroxide structures (with the exception of a form of hydroxide hydrate, which has no other suitable diffraction lines in these given patterns), nor for any other forms of BN or Re according to a thorough database search[26].

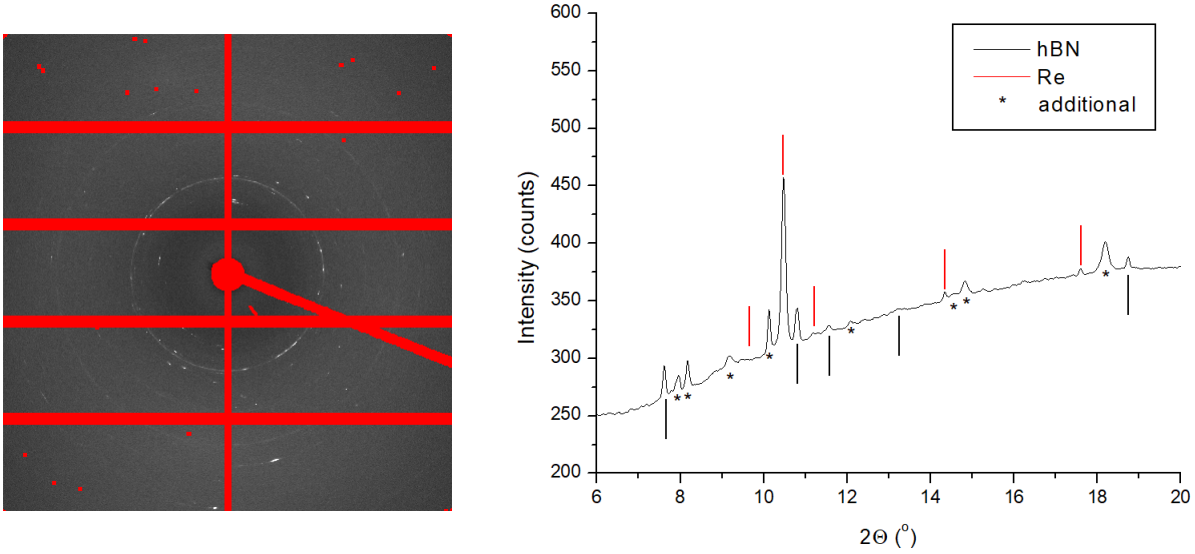

FIGURE 6.4: The recorded X-ray diffraction image (left panel) and corresponding pattern (right panel) from the # 234 location shown within the Figure 6.1 scan, as obtained within the Dioptas interface[24]. Red regions in the image show where a mask is applied to negate the contributions of certain regions, due to either gaps between detectors (leading to 0 counts) or any points of saturation, often from diffraction through the DAC itself rather than sample.

Focusing more on the XRD line at $2\theta = 5.7^o$, a convincing proposal for this line would

be that of the (0 0 2) of hBN, with an expanded lattice due to the presence of an intercalant. Calculations and experiments reported in by Kim *et al.*[23] predict an expansion of the c-parameter by 12-17% with respect to pure hBN, whereas an expansion of 33.4% would be required to produce this expected line, providing initial disapproval of the proposal. However, the appearance of new features observed in the X-ray diffraction pattern provided weight to the proposal of BNIC assignment for this line by considering 2- and 3-stage intercalations.

In certain regions of the scan area, new features appear in the X-ray pattern corresponding to larger d-spacing. In the pattern, the have a have a partial ring quality, confined along a small arc; this is best seen in the XRD image # 234 at position highlighted in Figure 6.4. This 'smeared line' feature would seem to imply that they have a highly preferred orientation, while also not being a collection of single crystals, meaning this is likely either co-oriented poly-crystals or possibly a powder with an incredibly preferred orientation. These features are located in close proximity to the (0 0 2) line of pure hBN, and are radially just past an intense region for that hBN line. The logic used before extended in this direction can be summarized as "what if these, too, are (0 0 2) lines".

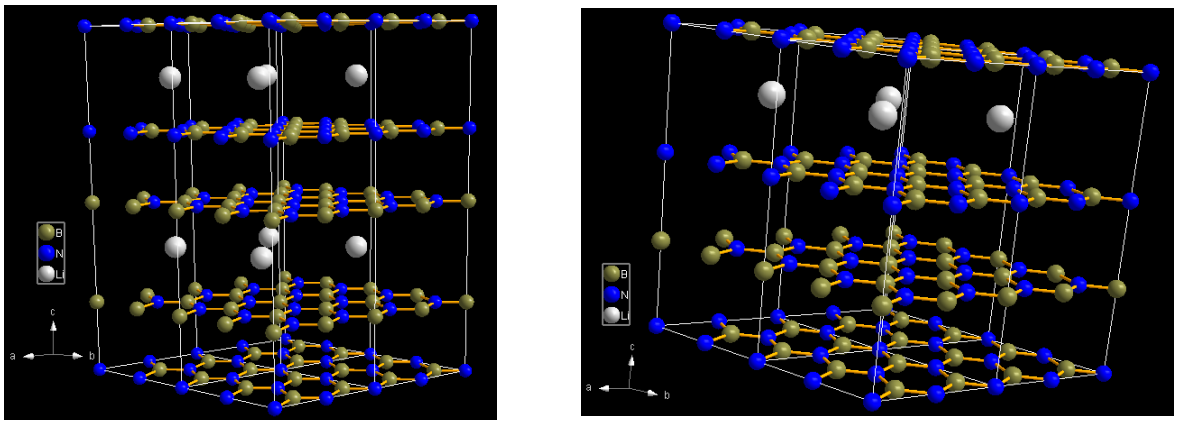

(A) 2-stage. (B) 3-stage.

FIGURE 6.5: The BNIC structural models developed based on the proposed expansion/compression staging. From these models, X-ray diffraction patterns were calculated and compared to the observed lines.

Considering a multi-stage intercalation structure like those shown in Figure 6.5, the expansion of the stages that have the intercalant may arguably express a 'crystallographic pressure' on the unintercalated stages, causing a reduction of those planes. The resulting compression of these stages would be 4 or 8% for a respective 3- or 2-stage model, according to our diffraction data. The mix of compression and expansion of the opposite stages would result in an overall expansion of 12.7 or 16.7% respectively for the 3- or 2-stage models, which is well in-line with the 12-17% expected. A change between interlayer spacings in different staging models may also help explain why the interlayer diffraction line presumably witnessed around $2\theta = 5.7^{o}$ is so broad and weak. As no structural data has been published for these models, let alone with the specific lattice parameters and expansion-compression considerations, the structures were modeled in Diamond 3.2[27] in order to provide a structural basis to analyze and a simulated powder diffraction pattern to compare to our diffraction data to fit the structures as proposed present species. These models were constructed considering those produced by *Kim et al.*[23], the A-Li-A stacking shown by Sumyoshi[11] and Shimada[16], and our own data, resulting in the structures shown in Figure 6.5. These structures were utilized for the calculation of a corresponding powder X-ray pattern.

The majority of the scan region remained this way, with all the patterns showing a mix of the features seen in Figures 6.3 and 6.4. In the upper portion of the scan area, new diffraction spots started to appear, bringing additional features to be considered in the fitting of structures. These singular spots are of high intensity, in very precise regions, and sharing no others at that diffraction angle, as seen by Figure 6.6. These spots seem to imply a single crystal of some kind. This would mean this is quite likely from a different compound than those shown in Figure 6.5, implying the existence of a second unknown species within the sample chamber.

The histogram was only analyzed from 5-15^{o}, as above 15^{o} the distribution of lines from the simulated patterns became too dense, the observed lines were too weak, and the

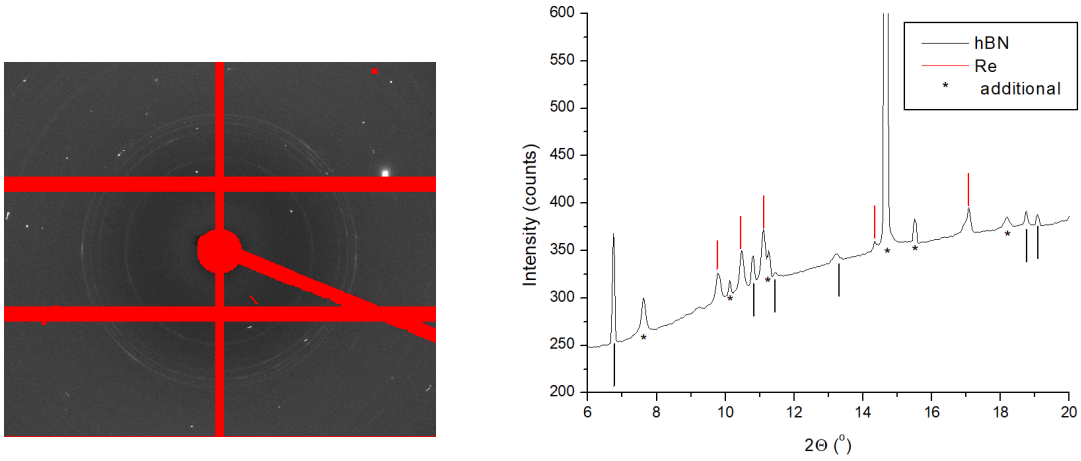

FIGURE 6.6: X-ray diffraction image (left) and processed plot (right) of scan # 518 of the Li+hBN sample. The corresponding region can be found in 6.1. It is immediately obvious that there are different diffraction characteristics and corresponding diffraction lines than that seen in Figure 6.4, such as the incredibly intense Bragg spot near 14.7^o, hinting at different specimen within this region.

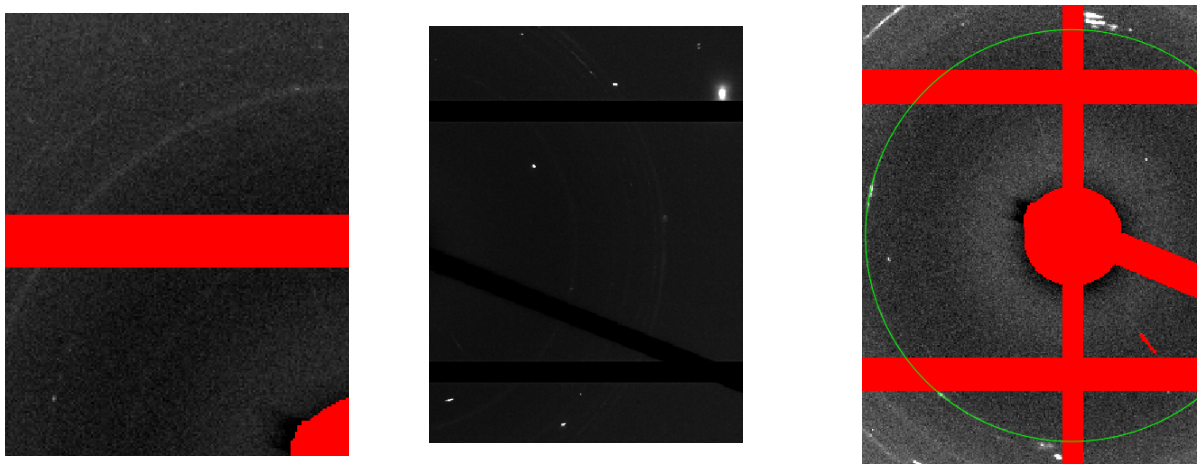

FIGURE 6.7: The XRD feature types in which Figure 6.8 has unlabeled peaks separated into. Two of the most prominent additional rings are shown on the leftmost image, representing powder-type X-ray diffraction (from the 211 position of the chamber). Intense X-ray diffraction spots are shown in the middle image(from the 494 position). In the rightmost image, an XRD pattern (from the 235 position) shows smeared-type features laying close to the (0 0 2) of hBN, marked by the green circle.

reliability of the relation of observed lines to hBN or Re even became uncertain, meanwhile nothing was observed below 5^o. Within this range, the lines that were associated

to the known expected hBN and Re structures were removed and other simulated patterns were compared with variable success. The BNIC models fit many of the observed lines, which could be expected considering the models were simulated using an observed line for their (0 0 2) d-spacing. Disappointingly, most other structures only provided 1-3 lines, if any, that were in somewhat close relation to those observed. One structure stood out, however. The $LiOH(H_2O)$ structure fit many lines, including the weak, prevalent 5.7^o line that most were unable to approach. The structural parameters were fit based on observed lines, providing a revised simulated powder pattern that could be compared with the BNIC models as seen in Figure 6.8.

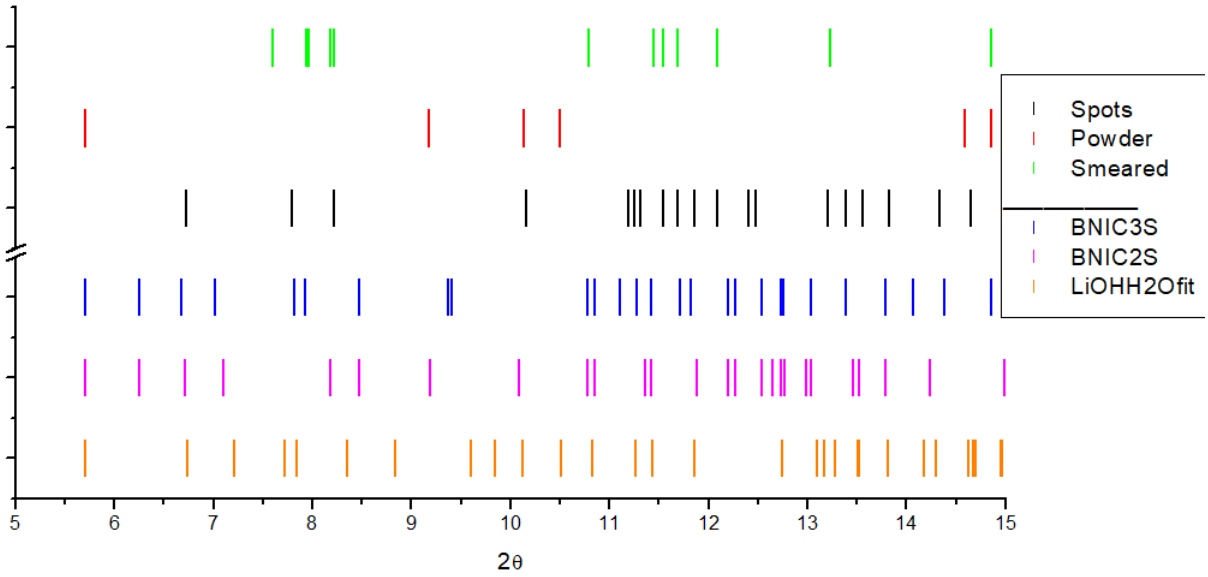

FIGURE 6.8: Histograms showcasing observed lines from the Li+hBN sample which are not related to Re or hBN structures (top three histograms) and simulated powder patterns (bottom three histograms) for the structures with the best match of the observed lines.

Through systematically comparing powder patterns of possible structures, the three contenders were considered to be the BNIC structures, both 2-stage and 3-stage, and the $LiOH(H_2O)$ structure. In order to determine which one was the more likely between the two, the number of corresponding observed lines for each structure was recorded, the results of which are presented in Table 6.1. The table accounts for the number of comparable lines for each structure to each pattern type, be it spotty, powder-like, or smeared,

	Material		Spots			Powder			Smeared			Problem lines		
Contenders	**Matched**	**Total**	**Matched**	**Total**	**Error**	**Matched**	**Total**	**Error**	**Matched**	**Total**	**Error**	**Matched**	**Total**	**Error**
LiOH (H_2O)	16	27	10	19		4	6	0.25	3	11.5	0.25	0	8	
Li-BNIC - 3S	11	26	10	19	3	2	6	1	5	11.5	2	0	8	
Li-BNIC - 2S	16	25	10	19	1.5	3	6	0	5	11.5	0.25	0	8	
Combined BNIC		37	12	19		4	6	0	6	11.5	0	0	8	
Alternatives														
dH LiBN composite	10	20	8	19	2	0	6		5	11.5	1.5	2	8	
Li_3N	5.5	13	5.5	19	0.5	0	6		5	11.5	1.5	2	8	
Li_2N_2	5	13	1.5	19	0.5	3	6		0.5	11.5	0.5	1	8	

TABLE 6.1: X-ray diffraction featured that correspond to the lines of the powder patterns of proposed structures . "Total" columns denote the number of observed lines, that may be matched with them, and "Matched" the number that may correspond. "Material" shows the total number of present and matching lines, indiscriminate to the type of diffraction. "Problem lines" are the lines which aren't aligned with any of the top contenders proposed which are considered in the histogram in Figure 6.9.

and compares it to the total the exist within the presented histogram shown in Figure 6.8. The material columns consider how many observed lines total match with a unique simulated line for the "matched" column, and the maximum number of observed lines from a certain species are matched with a unique simulated line in the "matched" column. Since the smeared pattern types could arguably be from the same species creating the powder or spot type diffraction patterns (but not both), it is included in the totals within the "material" columns

As can be seen from Table 6.1, the LiOH(H_2O) structure has an equal potential to the BNIC models. Considering one of the proposed staging models exists in the sample, the other similar model has definite potential of existing. As such, the correlation from both BNIC models is considered as "combined BNIC", which considers any overlapping simulated lines from the 2 staging models as 1, as they are non-unique. Only with this does the BNIC model correspond to more observed lines than the LiOH(H_2O) model with fitted parameters, and only just by a few. As such, it is hard to say definitely which one is expected within this sample, and without more, higher quality data, no quantitative analysis with a proper figure of merit can be developed to consider either with a given level of confidence.

Despite the BNIC and LiOH(H_2O) structures correlating with a good number of lines,

there still exist numerous X-ray diffraction lines that these structures cannot account for entirely. These "problem lines" are taken for another round of structure fitting. Much like what was done for Figure 6.8, the lines which are related to the proposed structures were removed and the remaining observed lines are what are left in the histogram shown in Figure 6.9 for the third order structural fits. Once again, most of the reported species which could have been created, lithium nitrides, oxides, hydroxides, and composites didn't have many corresponding diffraction lines, but of those lines remaining following the removal of the LiOH(H_2O) and BNIC correlated lines, most of these structures had NO corresponding lines. Those that had one or more potentially corresponding line were the dehydrogenated Li_3BN_2 composite (or dH Li_3BN_2), Li_3N, and Li_2N_2, which are included in the histogram presented in Figure 6.9. The correlation of the powder pattern of these structure with the remaining observed lines is still not perfect, but more considerable than any other previously reported crystal structure that may be found in this sample. The correspondence of these structures with these remaining "problem peaks" is reported in Table 6.1. Li_3N has been reported as a by-product of mixing liquid Li with hBN[28], so it is interesting to note that there is such weak evidence for any being present.

Of course, there may be an entirely new compound with a unique crystal structure that is responsible for some or many of these XRD lines, but with the data available it wouldn't be possible to even propose what this would be.

6.4 Conclusions and Future Potential

This work on the BNICs is obviously in its very early stages of development in our group. Nonetheless, it has high potential as a research topic and constitutes a promising avenue to generate novel compounds, while posing an incredible technical challenge in sample

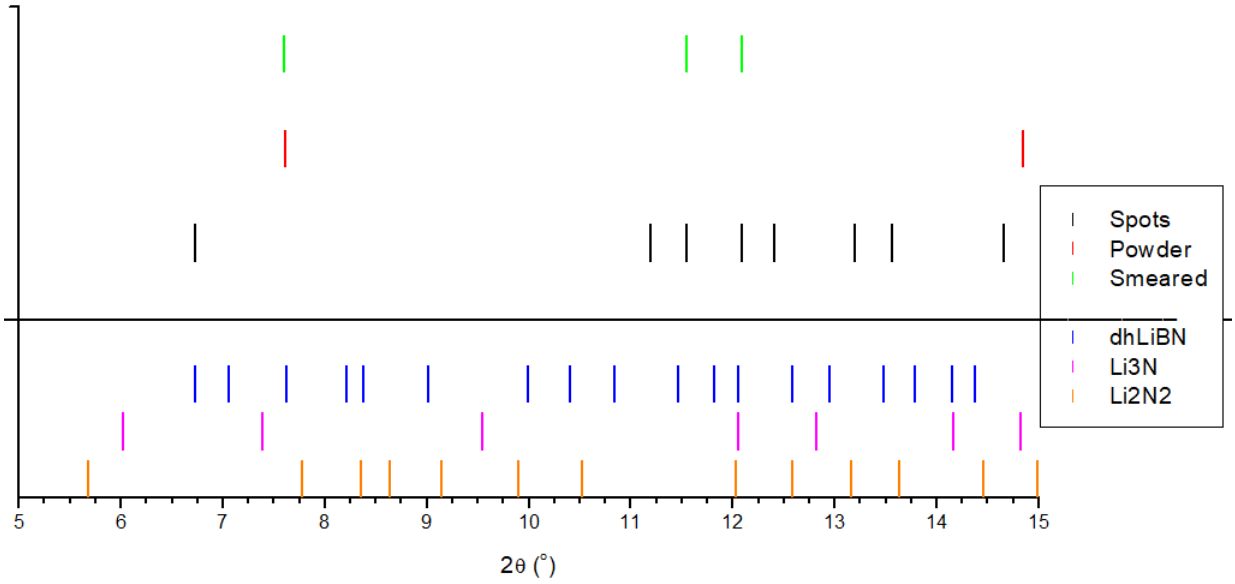

FIGURE 6.9: Histogram of powder patterns of other potential species within the Li+hBN sample compared to the remaining unlabeled diffraction lines not relatable to Re, hBN, or those considered in Figure 6.8.

preparation and XRD data analysis. With suitable samples and more XRD results, questions regarding the nature of any potential compounds that were produced in this experiment may be revealed. But there exists even greater potential to this project. The analysis of confirmed Li-BNICs under pressure would be a very clean and revealing experiment. Following the guidelines of the reproducible intercalation method described by Sumiyoshi[11], it would be interesting to observe lithium - hBN mixtures under pressure that have undergone treatments of milling, heating, and both, as well as both these treatments with mixtures of hBN with stable lithium nitrides.

Equally, the performance of these experiments with a mixture of hBN and graphite could produce further advantages, as this has already been addressed[29] in producing good BNICs at hundreds of kelvin lower than what could be achieved from the mix without the graphite. Furthermore, graphite could serve in this case as a viable heating element for further promotion of lithium atoms into the hBN lattice. Whether or not this level of intercalation would be sufficient to allow the BNIC to transition into a metal wouldn't

matter for the purpose of heating in that case, and experiments on a hBN-like structure and high pressures and high temperatures may be done with the potential of generating novel and useful compounds, such as a lithiated bctBN structure.

At low temperatures the Li-BNIC compound should demonstrate equally interesting properties. Under ambient pressure LI-BNIC may be a high temperature superconductor, with a critical temperature of around 25 K[16]. It would be interesting to inspect those properties and how they change with increasing pressures, as most superconducting critical temperatures tend to increase under sufficient pressure.

Considering the Li-BNIC compound is reported to be stable under an ambient atmosphere, it would then be interesting to see how it would behave under pressure in a nitrogen atmosphere - whether the nitrogen would be promoted into the crystal structure or whether the lithium would react to form lithium nitride, vacating the Li-B-N network. In the case of nitrogen incorporation, this very well could lead to novel compounds with nitrogen single bonds, interesting electronic properties, and ultra-hard properties, as discussed in Chapter 1.

The possibilities and interesting research avenues for this material under extreme conditions forms a long list that merits future attention by all means.

Bibliography

1. Li, Y., Hao, J., Liu, H., Lu, S. & Tse, J. S. High-Energy Density and Superhard Nitrogen-Rich B-N Compounds. *Phys. Rev. Lett.* **115,** 105502. ISSN: 0031-9007, 1079-7114 (Sept. 2015).

2. Lin, S. *et al.* Prediction of Superhard B_2N_3 with Two-Dimensional Metallicity. *J. Mater. Chem. C* **7,** 4527–4532. ISSN: 2050-7526, 2050-7534 (2019).

3. Xie, C. *et al.* Superhard Three-Dimensional B_3N_4 with Two-Dimensional Metallicity. *J. Mater. Chem. C* **5,** 5897–5901. ISSN: 2050-7526, 2050-7534 (2017).

4. Shen, C. *et al.* Intercalation of Hexagonal Boron Nitride by Strong Oxidizers and Evidence for the Metallic Nature of the Products. *Journal of Solid State Chemistry* **147,** 74–81. ISSN: 0022-4596 (Oct. 1999).

5. Doll, G. L. *et al.* Intercalation of Hexagonal Boron Nitride with Potassium. *J. Appl. Phys.* **66,** 2554–2558. ISSN: 0021-8979, 1089-7550 (Sept. 1989).

6. Kovtyukhova, N. I. *et al.* Reversible Intercalation of Hexagonal Boron Nitride with Brønsted Acids. *J. Am. Chem. Soc.* **135,** 8372–8381. ISSN: 0002-7863, 1520-5126 (June 2013).

7. Altintas, B., Parlak, C., Bozkurt, C. & Eryiğit, R. Intercalation of Graphite and Hexagonal Boron Nitride by Lithium. *Eur. Phys. J. B* **79,** 301–312. ISSN: 1434-6028, 1434-6036 (Feb. 2011).

8. Zhao, S. Y. F. *et al.* Controlled Electrochemical Intercalation of Graphene/ *h*- BN van Der Waals Heterostructures. *Nano Lett.* **18,** 460–466. ISSN: 1530-6984, 1530-6992 (Jan. 2018).

9. Kheirabadi, N. & Shafiekhani, A. Intercalation of Boron Nitride Quantum Dots with Lithium: Boron Nitride as a Protecting Layer for a Lithium-Ion Battery and a Spin-Dependent Photon Emission Device. *ArXiv200605792 Cond-Mat Physicsphysics*. arXiv: 2006.05792 [cond-mat, physics:physics]. http://arxiv.org/abs/2006.05792 (2020) (May 2020).

10. Kim, J., Yamasue, E., Ichitsubo, T., Okumura, H. & Ishihara, K. N. Electrochemical Lithium Intercalation Behavior of Pristine and Milled Hexagonal Boron Nitride. *Journal of Electroanalytical Chemistry* **799,** 263–269. ISSN: 15726657 (Aug. 2017).

11. Sumiyoshi, A., Hyodo, H., Sato, Y., Terauchi, M. & Kimura, K. Good Reproductive Preparation Method of Li-Intercalated Hexagonal Boron Nitride and Transmission Electron Microscopy – Electron Energy Loss Spectroscopy Analysis. *Solid State Sciences* **47,** 68–72. ISSN: 12932558 (Sept. 2015).

12. Kim, J., Yamasue, E., Okumura, H., Ishihara, K. N. & Michioka, C. Structures of Boron Nitride Intercalation Compound with Lithium Synthesized by Mechanical Milling and Heat Treatment. *Journal of Alloys and Compounds* **685,** 135–141. ISSN: 09258388 (Nov. 2016).

13. Sumiyoshi, A., Hyodo, H. & Kimura, K. Li-Intercalation into Hexagonal Boron Nitride. *Journal of Physics and Chemistry of Solids* **71,** 569–571. ISSN: 00223697 (Apr. 2010).

14. Laniel, D., Weck, G. & Loubeyre, P. Direct Reaction of Nitrogen and Lithium up to 75 GPa: Synthesis of the Li_3N, LiN, LiN_2, and LiN_5 Compounds. *Inorg. Chem.* **57,** 10685–10693. ISSN: 0020-1669, 1520-510X (Sept. 2018).

15. Laniel, D., Weck, G., Gaiffe, G., Garbarino, G. & Loubeyre, P. High-Pressure Synthesized Lithium Pentazolate Compound Metastable under Ambient Conditions. *J. Phys. Chem. Lett.* **9,** 1600–1604. ISSN: 1948-7185 (Apr. 2018).

16. Shimada, N. H., Minamitani, E. & Watanabe, S. Theoretical Prediction of Phonon-Mediated Superconductivity with $T_c \approx 25$ K in Li-Intercalated Hexagonal Boron Nitride Bilayer. *Appl. Phys. Express* **10,** 093101. ISSN: 1882-0778, 1882-0786 (Sept. 2017).

17. Nagamatsu, J., Nakagawa, N., Muranaka, T., Zenitani, Y. & Akimitsu, J. Superconductivity at 39 K in Magnesium Diboride. *Nature* **410,** 63–64. ISSN: 1476-4687 (Mar. 2001).

18. Hirai, H., Wanme, K., Yagi, T., Ikeda, A. & Abe, T. High-Pressure Synthesis of a Novel Form of Endohedral Li Diamond from Li Graphite Intercalation Compound. *Journal of Physics and Chemistry of Solids* **65,** 933–938. ISSN: 00223697 (May 2004).

19. Hromadová, L. & Martoňák, R. Pressure-Induced Structural Transitions in BN from *Ab Initio* Metadynamics. *Phys. Rev. B* **84,** 224108. ISSN: 1098-0121, 1550-235X (Dec. 2011).

20. Tapia-Ruiz, N., Segalés, M. & Gregory, D. H. The Chemistry of Ternary and Higher Lithium Nitrides. *Coordination Chemistry Reviews* **257,** 1978–2014. ISSN: 00108545 (July 2013).

21. Hanfland, M., Loa, I., Syassen, K., Schwarz, U. & Takemura, K. Equation of State of Lithium to 21GPa. *Solid State Communications* **112,** 123–127. ISSN: 0038-1098 (Sept. 1999).

22. Guillaume, C. L. *et al.* Cold Melting and Solid Structures of Dense Lithium. *Nat. Phys.* **7,** 211–214. ISSN: 1745-2481 (Mar. 2011).

23. Kim, J., Yamasue, E., Okumura, H. & Ishihara, K. N. Crystal Structures and Electronic Band Structures for Hypothetic Lithium Boron Nitride Intercalation Compounds. *Journal of Alloys and Compounds* **751,** 324–334. ISSN: 09258388 (June 2018).

24. Prescher, C. & Prakapenka, V. B. *DIOPTAS* : A Program for Reduction of Two-Dimensional X-Ray Diffraction Data and Data Exploration. *High Pressure Research* **35,** 223–230. ISSN: 0895-7959, 1477-2299 (July 2015).

25. Desgreniers, S. & Lagarec, K. XRDA: A Program for Energy-Dispersive X-Ray Diffraction Analysis on a PC. *J. Appl. Crystallogr.* **27,** 432–434. ISSN: 1600-5767 (1994).

26. *ICSD - Basic Search & Retrieve* https://icsd-fiz-karlsruhe-de.proxy.bib.uottawa.ca/search/basic.xhtml (2021).

27. Putz, H. & Bradenburg, K. *Diamond - Crystal and Molecular Structure Visulatization* Crystal Impact. 102, 53227 Bonn, Germany. http://www.crystalimpact.com/diamond.

28. Wen, J. *et al.* Highly Adhesive Li-BN Nanosheet Composite Anode with Excellent Interfacial Compatibility for Solid-State Li Metal Batteries. *ACS Nano* **13,** 14549–14556. ISSN: 1936-0851, 1936-086X (Dec. 2019).

29. Kim, J., Yamasue, E., Okumura, H., Michioka, C. & Ishihara, K. N. Intercalation of Hexagonal Boron Nitride and Graphite with Lithium by Sequential Process of Ball Milling and Heat Treatment. *Journal of Alloys and Compounds* **707,** 172–177. ISSN: 09258388 (June 2017).

Chapter 7

Summary and Future Prospects

BN was analyzed under pressure using X-ray diffraction and Raman and infrared spectroscopy. Powdered and single crystal hBN was loaded with and without a hydrostatic PTM to ensure the consideration of a variety of configurations. Starting at 9 GPa, phase I of BN, hBN, transitions to phase II, wBN. This transition is complete above 14 GPa for samples under hydrostatic conditions, but incomplete above 20 GPa for non-hydrostatic conditions. This transition is reversible in all observed cases; reconverted hBN was observed by XRD below 1.5 GPa on decompression, and a mix of hBN and wBN at ambient were observed for all recovered samples. Recompression of hBN under hydrostatic conditions lead to the greatest yield of wBN, with a wBN:hBN ratio of over 60:1.

The wBN formed has a high concentration of defects, shown by a broadening of XRD line by 2-3 times, by a high luminescence signal, and by new, defect-activated IR modes related to the phase. The luminescent background made obscured any potential observation of the wBN Raman lines. One of the defect-activated IR modes has been reported in literature[1,2], but the others have not. These modes are most likely related to peaks within the calculated phonon density of states[2].

The elastic parameters of hBN and wBN were estimated based on the pressure response of the materials. For hBN, the reported values of B_0 and B_0' are varied within literature[3–6] and highly dependent on the EoS used to estimate the parameters. Pressure coefficients for phonon modes were in good agreement with those reported in literature[7,8]. A softened E_{2g} mode was observed in recovered hBN. This mode softening is likely related to defects in the hBN structure. With increased laser power, the softening of this mode increases, most likely due to heating effects by light absorption. An attempt was made to

estimate the temperature based on of this softening, but this estimation is advanced with minimal confidence until further experiments can be carried out.

While several new XRD lines were observed, which could not be related to any expected phase, no features of the Raman or IR spectra point to the presence of any new phase(s) of BN.

Protocols were developed for filtering IR spectra to remove interference effects which appear due to the DAC acting as a Fabry-Perot cavity. While the filtering does introduce some artifacts, it is usually only around sharp features, and the artifacts are weak and localized. This was a necessary step to discern between what features were inherent to the material and which were a result of the interference or filtering.

A method was devised to use the NaCl PTM X-ray diffraction line to calibrate for pressure and temperature within a single X-ray diffraction pattern. The pressure calibration agreed with ruby measurements and allowed for local measurements of pressure anywhere within the sample chamber. The temperature calibration didn't correspond with the blackbody measurement, which was consistently higher than the NaCl calibration; neither agreed with the temperature expected by hBN expansion, which laid between both measurements in all cases. The NaCl and blackbody measurement thus make up lower and upper bounds for the true temperature, respectively, of the area of interest.

Laser heating of hBN to generate HPHT conditions while performing XRD on dense hBN proved challenging. Because hBN won't couple to the heating laser directly, methods for sympathetic heating of hBN using laser absorbers and heat diffusers were employed. These were in the form of powders mixed with the sample or, in one case, a separated ring of rhenium. While some thermal expansion of hBN was observed by XRD, the temperature related to this expansion was nowhere near the 2000 K needed to form predicted new phases of BN[9].

Finally, a mixture of lithium and hBN was loaded into a DAC. Upon compression, the sample was observed to turn dark. While only the hBN E_{2g} phonon modes were observed

under pressure, several new XRD lines appeared. No singular, predicted or reported compound within the $Li_xB_yN_z$ system accounted for all the new diffraction lines, though a combination of a compound-staging Li-BNIC with proposed Li_xN_y by-products accounts for most of these XRD lines. Future experiments could feature prepared Li-BNIC, synthesized following the procedure in , under a N_2 or ionic PTM to see how the compound behaves under pressure and whether lithium intercalant could promote intercalation of N_2. How the high predicted critical temperature for superconductivity for Li-BNIC behaves under pressure would be a further interesting avenue for exploration.

Challenges with HPHT experiments

Many challenges were faced over the course of the heating experiments that merit mention. This is by no means excuses for not having more high quality results, but may answer any questions of "why didn't they just try it again, but better?".

The most concise answer to this question is often "time". Foremost, these experiments are only possible at a handful of labs around the world, all of which are in high demand by users. It should also be noted that all of these facilities are international, so travel to them was not a possibility for the latter portion of the project. Though we were lucky enough to be awarded time for work on this project, that time was limited to about 48 hours, for a portion of which the beam was inactive (beam trips are a common nuisance in the life of any synchrotron user). A concerted focus on data collection meant that analysis during the experiment could not be done at any more than a superficial level, there was too little time to recognize if a mistake was made let alone correct for it. The experimental skill and patience required to prepare suitable samples in diamond anvil cell, align near-IR lasers with an X-ray beam with micrometer precision, and the optics to measure temperature and pressure on a microscopic sample also deserves to be taken into account.

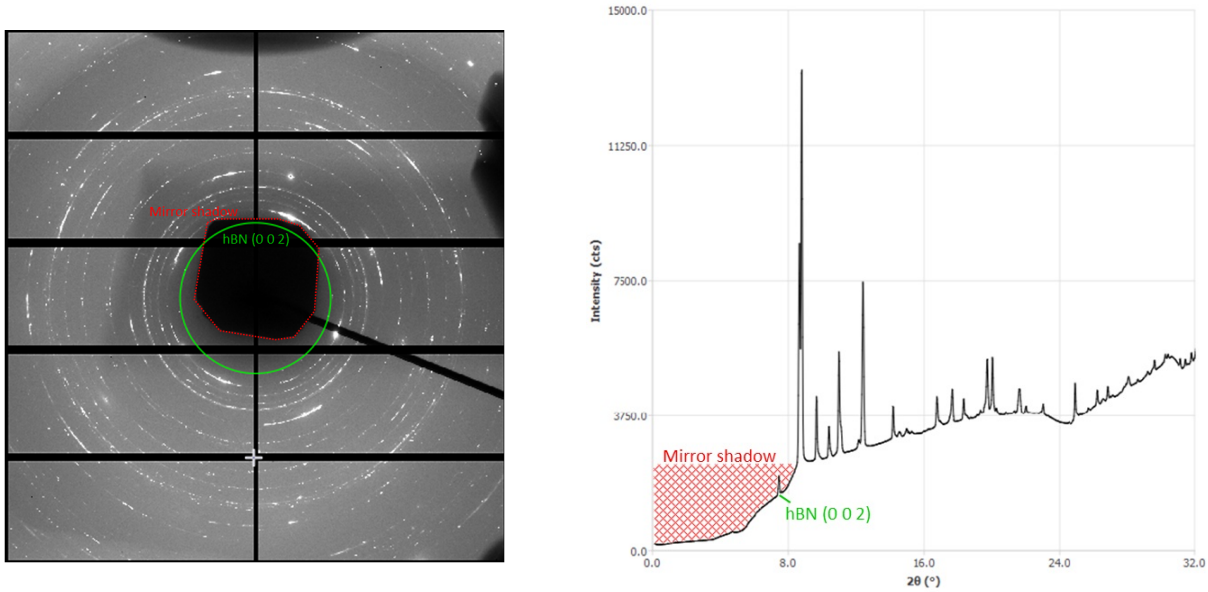

FIGURE 7.1: The effect on the XRD pattern from introducing the amorphous carbon mirrors in the beam path for laser heating. A shadow of the mirror can clearly be seen in the corresponding XRD image (left). This leads to a reduction in intensity for the integrated plot on the right. Information is thus lost, as XRD lines blocked by this shadow, notably much of the important (0 0 2) line of hBN.

Not all the challenges were related to a lack of the valuable resource of time, several challenges were technical, despite performing these experiments at some of the top labs in the world. While the amorphous carbon mirrors didn't diffract any of the X-rays, it still scattered them. As shown in Figure 7.1, the scattering blocked any diffraction lines from passing the mirror, leading to a region of no signal or reduced fidelity. Notably, the important (0 0 2) diffraction line from the hBN structure fell into the region partially masked by the mirror, often obscured to the point where it wasn't recoverable. This line is one of the most intense, and is essential in defining the c-parameter, without which compression or thermal expansion is nearly impossible to judge.

To ensure that diffraction lines aren't clipped by the DAC supports, the bulk of the sample is usually placed closer to the downstream anvil. This means, however, that the X-ray beam passes through more of the cold, less interesting PTM prior to reaching the sample. Not only does this result in a higher signal from the colder region, imposing a

bias in the thermal splitting in favor of the cold side, but the beam and resulting intensity is weaker for the latter, heated portions of the cell. In the interest of a low Z material such as hBN, this is troubling, since the scattering intensity being proportional to Z^2 means that scattering from the sample is already weaker than from the cell cohabitants before even considering this effect.

The Z^2 scattering intensity proportionality is especially notable considering that rhenium is used as a gasket material and sometimes heating element. Rhenium has an atomic number of 75, which means its scattering intensity is 156 times greater per unit cell than hBN, which has an effective Z of 6. Near the gasket there is also much more rhenium present, by a factor of a few orders of magnitude. Should the rhenium be 100 times thicker, and it is often more, this would mean that the beam would have to be at least 4 standard deviations away from it in order for the rhenium signal to only be equal to the sample. With a FWHM of 10μm[10], this equates to about 20 μm or more, which is a substantial region of our cells.

Also to note is the microscopic size of the sample assemblies. All of these experiments are assembled manually, with the exception of the laser machining process which utilizes a motorized stage. Assemblage requires a considerable amount of time, patience, skill, and sometimes attempts, and nonetheless perfection is never attainable, as with all things. This is true for all experiments, not just the laser heating ones, but these experiments tend to be much more complex.

Several challenges were faced in use of the rhenium ring attempt to have a suitable heat diffuser. Some were conquerable, such as the pressure difference between ruby gauge and sample expected from the rigid ring geometry, where the NaCl EoS was used as a secondary pressure gauge. Some challenges, however, had no such elegant solution (none yet thought of, at least). Unfortunately, due to the limited volume of hBN sample present, the amount of additional information that could be found from this series is limited. Many of the XRD patterns taken during the heating cycles demonstrated few XRD lines from

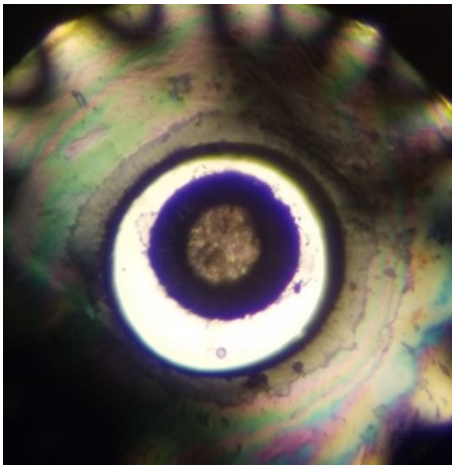

(A) ring setup before heating.

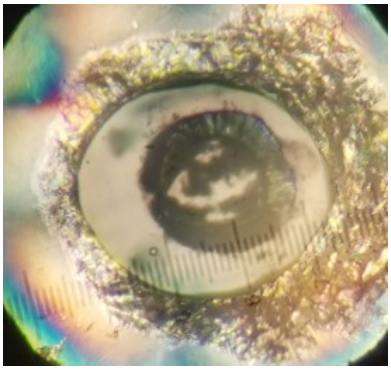

(B) ring setup after heating.

FIGURE 7.2: Pictures taken of the Re ring setup before and after heating, respectively. The paths taken by the heating lasers can be seen from the excavated ring interior.

hBN, making the calculation of the unit cell volume and lattice parameters less reliable, if possible at all. The experiment showed that, despite not providing sufficient heat to the sample, that this sample assembly has potential for use here, and that NaCl is just as effective and convenient a pressure and temperature gauge as it is a PTM.

Future experiments should be done with a similar setup using a higher sample to NaCl ratio, tuning the ratio to have a higher signal from the sample, while still being able to resolve the heated NaCl lines for temperature calibration. The heating problem can be solved in a few different ways. Now knowing how little heat might be imparted into the surroundings, there is less fear of going much higher in power with the heating lasers, immediately providing more heat. One area of concern is that the heating element is damaged over the course of the experiment, as shown in Figure 7.2. This should be taken into account in preparations of similar experiments in the future.

Bibliography

1. Dong, Z. & Song, Y. Transformations of Cold-Compressed Multiwalled Boron Nitride Nanotubes Probed by Infrared Spectroscopy. *J. Phys. Chem. C* **114,** 1782–1788. ISSN: 1932-7447, 1932-7455 (Feb. 2010).

2. Segura, A. *et al.* Nonreversible Transition from the Hexagonal to Wurtzite Phase of Boron Nitride under High Pressure: Optical Properties of the Wurtzite Phase. *J. Phys. Chem. C* **123,** 20167–20173. ISSN: 1932-7447, 1932-7455 (Aug. 2019).

3. Solozhenko, V. L., Will, G. & Elf, F. Isothermal Compression of Hexagonal Graphite-like Boron Nitride up to 12 GPa. *Solid State Commun.* **96,** 1–3. ISSN: 0038-1098 (Oct. 1995).

4. Godec, Y. L. *et al.* Thermoelastic Behaviour of Hexagonal Graphite-like Boron Nitride. *High Press. Res.* **17,** 35–46. ISSN: 0895-7959 (Mar. 2000).

5. Urakawa, S., Morishima, H., Kato, T., Suzuki, A. & Shimomura, O. Equation of State for *H*-BN. *Photon Fact. Act. Rep. 11196* 383 (2004).

6. Fuchizaki, K., Nakamichi, T., Saitoh, H. & Katayama, Y. Equation of State of Hexagonal Boron Nitride. *Solid State Communications* **148,** 390–394. ISSN: 0038-1098 (Dec. 2008).

7. Segura, A. *et al.* High-Pressure Softening of the Out-of-Plane A_{2u} (Transverse-Optic) Mode of Hexagonal Boron Nitride Induced by Dynamical Buckling. *J. Phys. Chem. C* **123,** 17491–17497. ISSN: 1932-7447, 1932-7455 (July 2019).

8. Cuscó, R. *et al.* Pressure Dependence of the Interlayer and Intralayer E_{2g} Raman-Active Modes of Hexagonal BN up to the Wurtzite Phase Transition. *Phys. Rev. B* **102,** 075206 (Aug. 2020).

9. Hromadová, L. & Martoňák, R. Pressure-Induced Structural Transitions in BN from *Ab Initio* Metadynamics. *Phys. Rev. B* **84,** 224108. ISSN: 1098-0121, 1550-235X (Dec. 2011).

10. Hirao, N. *et al.* New Developments in High-Pressure X-Ray Diffraction Beamline for Diamond Anvil Cell at SPring-8. *Matter and Radiation at Extremes* **5,** 018403. ISSN: 2468-2047 (Jan. 2020).